ANALYSIS AND CONTROL OF A BIO-INSPIRED AERIAL VEHICLE WITH AN ACTIVELY CONTROLLED ABDOMEN-LIKE APPENDAGE

A THESIS SUBMITTED TO
THE GRADUATE SCHOOL OF NATURAL AND APPLIED SCIENCES
OF
MIDDLE EAST TECHNICAL UNIVERSITY

BY

BERRİN GÜNEY

IN PARTIAL FULFILLMENT OF THE REQUIREMENTS
FOR
THE DEGREE OF MASTER OF SCIENCE
IN
ELECTRICAL AND ELECTRONICS ENGINEERING

SEPTEMBER 2022

Approval of the thesis:

ANALYSIS AND CONTROL OF A BIO-INSPIRED AERIAL VEHICLE WITH AN ACTIVELY CONTROLLED ABDOMEN-LIKE APPENDAGE

submitted by **BERRİN GÜNEY** in partial fulfillment of the requirements for the degree of **Master of Science in Electrical and Electronics Engineering Department, Middle East Technical University** by,

Prof. Dr. Halil Kalıpçılar
Dean, Graduate School of **Natural and Applied Sciences** _____

Prof. Dr. İlkay Ulusoy
Head of Department, **Electrical and Electronics Engineering** _____

Assoc. Prof. Dr. Mustafa Mert Ankaralı
Supervisor, **Electrical and Electronics Engineering, METU** _____

Examining Committee Members:

Prof. Dr. Kemal Leblebicioğlu
Electrical and Electronics Engineering, METU _____

Assoc. Prof. Dr. Mustafa Mert Ankaralı
Electrical and Electronics Engineering, METU _____

Prof. Dr. Umut Orguner
Electrical and Electronics Engineering, METU _____

Prof. Dr. Ömer Morgül
Electrical and Electronics Engineering, Bilkent University _____

Assoc. Prof. Dr. Ahmet Buğra Koku
Mechanical Engineering, METU _____

Date: 09.09.2022

I hereby declare that all information in this document has been obtained and presented in accordance with academic rules and ethical conduct. I also declare that, as required by these rules and conduct, I have fully cited and referenced all material and results that are not original to this work.

Name, Surname: Berrin Güney

Signature :

ABSTRACT

ANALYSIS AND CONTROL OF A BIO-INSPIRED AERIAL VEHICLE WITH AN ACTIVELY CONTROLLED ABDOMEN-LIKE APPENDAGE

Güney, Berrin
M.S., Department of Electrical and Electronics Engineering
Supervisor: Assoc. Prof. Dr. Mustafa Mert Ankaralı

September 2022, 104 pages

Animals' anatomies have control systems combined with multi motors and high-bandwidth sensors. Their complicated mechanisms give them high maneuverability with sufficient inertial stabilization performance during walking, jumping, and flying. From the point of aerial locomotion, flying insects use abdomen reflexes to stabilize their head positions. Articulation of the thoracic–abdominal joint contributes to the reorientation of their bodies over the law of conservation of angular momentum. Since acceleration is a fundamental component of maneuverability, increasing the acceleration without destabilizing the body is achieved with additional appendages such as the tail and abdomen. The presence of highly actuated abdominal muscles is an essential feature of these natural flyers conspicuously missing from the current aerial vehicles regarding maneuverability. In the scope of the thesis, we propose a bio-inspired aerial vehicle morphology with an actively controlled abdomen-like appendage. This study takes steps toward understanding the contribution of such an appendage to flight control. We aim to investigate the advantages and disadvantages of the abdomen-like appendage mounted on multi-rotor aerial vehicles by constructing the dynamical model and designing optimization-based controllers; Linear Quadratic

Regulator (LQR), Model Predictive Control (MPC), and Adaptive Model Predictive Control (A-MPC). We complete our analysis with a motion planning algorithm based on the idea of combining the sampling-based neighborhood graph approach with the A-MPC strategy. We demonstrate through simulation experiments that the appendage improves the stability and maneuverability of aerial vehicles, and the resulting motion planning structure with A-MPC ensures that the state and input constraints are not violated.

Keywords: abdomen-like appendage, adaptive model predictive control, bio-inspired aerial vehicle, linear quadratic regulator, sampling-based motion planning

ÖZ

AKTİF OLARAK KONTROL EDİLEN BİYO-ESİNLENİLMİŞ ABDOMİNAL UZUVLU BİR HAVA ARACININ ANALİZİ VE KONTROLÜ

Güney, Berrin
Yüksek Lisans, Elektrik ve Elektronik Mühendisliği Bölümü
Tez Yöneticisi: Doç. Dr. Mustafa Mert Ankaralı

Eylül 2022 , 104 sayfa

Hayvanlar anatomik olarak, çoklu motorlar ve yüksek bant genişlikli algılayıcılardan oluşan kontrol sistemlerine sahiptir. Bu karmaşık mekanizmaları onlara yürüme, zıplama ve uçuş sırasında yüksek manevra kabiliyeti ve ataletsel stabilizasyon performansı sağlar. Havada hareket açısından bakıldığında, uçabilen böceklerin baş pozisyonlarını karın kası refleksleri ile stabilize ettiği görülmüştür. Göğüs-karın ekleminin hareketi, vücutlarının açısal momentumun korunumu yasasına göre yeniden yönlendirilmesine katkıda bulunur. Manevra kabiliyetinin temeli ivmelenmeye dayalı olduğundan, gövde dengesini bozmadan ivmeyi arttırmak kuyruk ve karın gibi eklentiler ile sağlanır. Uçabilen böceklerin yüksek düzeyde tahrik edebildikleri karın kaslarının varlığı, manevra kabiliyeti açısından mevcut hava araçlarındaki önemli eksikliklerden biridir. Bu çalışmada, aktif olarak kontrol edilen karın benzeri eklentiye sahip, biyo-esinlenilmiş bir hava aracı morfolojisi önererek bu eklentinin uçuş kontrolüne katkısını inceledik. Sistemin doğrusal olmayan dinamik modelinin türetilmesi ve optimizasyon tabanlı kontrolcü tasarımları olan Lineer Kuadratik Regülatör (LQR), Model Öngürülü Kontrol (MPC) ve Uyarlamalı Model Öngörülü Kontrol (A-MPC)

ile bu eklentinin avantaj ve dezavantajlarının araştırılmasını amaçladık. Önerdiğimiz hava aracı morfolojisinin analizini örnekleme tabanlı komşuluk grafiği yaklaşımını A-MPC stratejisiyle birleştirme fikrine dayanan bir hareket planlama algoritması uygulayarak tamamladık. Simülasyon ortamında yapılan deneyler ile, eklentinin hava araçlarının stabilizasyonunu ve manevra kabiliyetini geliştirdiğini ve uyguladığımız hareket planlama yapısının sistemin kararlılığını durum ve girdi kısıtlarını ihlal etmeden sağladığını test sonuçları ile gösterdik.

Anahtar Kelimeler: biyo-esinlenilmiş hava aracı, karın benzeri eklenti, lineer kuadratik regülatör, örnekleme tabanlı hareket planlaması, uyarlamalı model öngörülü kontrolcü

To my family

ACKNOWLEDGMENTS

I would like to express my sincerest gratitude to my thesis supervisor, Assoc. Prof. Mustafa Mert Ankaralı for his meticulous academic advice, invaluable feedback, and continued guidance and support. I'm incredibly grateful for my time working with him.

I am thankful to my colleagues at ASELSAN; Gökhan Özdoğan for sharing his critical experiences with UAVs and advice as well as being an understanding and supportive team leader; Oğuzhan Tezgelen for his valuable MATLAB and LaTeX tips; Mehmet Sami Büyüksarıkulak for sharing his experiences with quadrotors; Galip Serdar Tombul for his discussions about analysis of nonlinear systems; Süleyman Emre Can and Başer Kandehir for their perfect blend of help and humor.

I would also like to thank Mert Özçelik for his endless support and patience. I am glad to have his friendship in my anxious times. Moreover, his guidance in modeling dynamical systems helped me complete this work.

My sincere thanks go to Simge Gönen for cheering me up and being there for me all the time.

And in the end, I would like to thank my family for always supporting me in all circumstances.

TABLE OF CONTENTS

LIST OF TABLES

TABLES

LIST OF FIGURES

FIGURES

LIST OF ABBREVIATIONS

2D	2 Dimensional
3D	3 Dimensional
A-MPC	Adaptive Model Predictive Control
CoG	Center of Gravity
DCM	Direction Cosine Matrix
DOF	Degrees of Freedom
ECEF	Earth Center Earth Fixed Frame
LQR	Linear Quadratic Regulator
LTI	Linear Time Invariant
MIMO	Multi Input Multi Output
MPC	Model Predictive Control
QP	Quadratic Programming
RHC	Receding Horizon Control
SNG	Sampling-based Neighborhood Graph
UAV	Unmanned Aerial Vehicle
USV	Unmanned Surface Vehicle
ZOH	Zero-Order Hold

LIST OF SYMBOLS

ρ	The density of air
$C_{f_1}^{f_2}$	Direction cosine matrix (DCM), that transforms one coordinate reference frame, f_1, to another, f_2.
I - frame	The inertial frame, origin is at the center of the Earth, and axes do not move relative to the stars.
E - frame	The Earth frame, origin is at the center of the Earth, axes are fixed with respect to Earth.
B - frame	The body frame, axes are aligned with the roll, pitch, and yaw axes of the vehicle.
A - frame	The abdomen-like appendage frame, axes are aligned with the body frame with origin at the joint between the appendage and the body.
P - frame	The propeller frame, axes are aligned with the body frame with the origin at the center of the propeller rotor.
h	Body height of the bi-rotor platform
L	Body length of the bi-rotor platform
d	Arm length of the quadrotor
J	Inertia matrix
I_{xx}, I_{yy}, I_{zz}	Moments of inertia about x, y, and z axes respectively.
I_{xy}, I_{yz}, I_{xz}	Products of inertia of the quadrotor
I_{px}, I_{py}	Moments of inertia of the 2-DOF abdomen-like appendage
ω_i	Angular speed of propeller i -th.
$\mathbf{c}_\alpha$	$cos(\alpha)$
$\mathbf{s}_\alpha$	$sin(\alpha)$
$\mathbf{t}_\alpha$	$tan(\alpha)$

$R(x, \alpha)$	Rotation matrix about the axis x of a coordinate system by an angle α.
$0_{m \times n}$	Zero matrix of size $m \times n$
$I_{n \times n}$	Identity matrix of size $n \times n$
f	Force vector acting on the joint between the appendage and the quadrotor body.
H	Angular momentum
A, B, C, D	State-space matrices of linear system
q	Generalized coordinates
u	Input vector
G	The gravitational vector
$\vec{g}$	Gravitational acceleration
$\omega_{A/B}$	The angular velocity of the B-frame relative to the A-frame.
$G(s)$	Plant transfer function
$C(s)$	Controller transfer function
x, y, z	Position of the quadrotor with respect to earth frame.
ϕ, θ, ψ	Euler angles of the quadrotor, roll, pitch, and yaw, respectively.
V_x, V_y, V_z	Translational velocities in the Earth frame.
p, q, r	Angular rates of the quadrotor with respect to the body frame.
ϕ_a, θ_a	Appendage angles with respect to the appendage frame.
τ_{ax}, τ_{ay}	Torques applied to the 2-DOF abdominal joint
Q, R	Weighting matrices that penalize states and inputs, respectively.

CHAPTER 1

INTRODUCTION

1.1 Motivation of the Study

Aerial vehicles of the current era have been used in many areas like rescue operations, mine detection, agriculture, entertainment, and package delivery. Engineers have spent a great deal of effort developing more efficient and safer designs as aerial vehicles are close to daily life.

In nature, free appendages such as the tail and abdomen assist animals in maneuvering and reorienting their bodies in midair. From the point of bio-inspired aerial robotics, there are numerous studies about the importance of appendages in stabilizing the body attitude. Additionally, the behavior of the appendage is an obvious example of the inertial redirection ability of flying animals. Therefore, we aim to examine the effects of such an appendage on aerial vehicles.

To the best of our knowledge, this is the first complementary study of the analysis and control of a bio-inspired aerial vehicle with an actively controlled abdomen-like appendage considering the nonlinearities and constraints of the system. In this work, we used dynamical models in the sagittal plane and 3D space with optimization-based controllers to show the effect of the abdomen-like appendage on the stabilization performance. Then, we performed a motion planning algorithm based on MPC policy with sampling-based neighborhood graph generation in a planar region.

Inspiration by the aerial maneuvering ability of the flying insects is the primary motivation of this study. We investigate the advantages and disadvantages of a bio-inspired aerial vehicle with an actively controlled abdomen-like appendage and analyze its re-

liability, efficiency, and safety performance. First and foremost, we want to examine the proposed system in a simulation environment and find the answer to the question, "Is it worth increasing the nonlinearity and complexity of the system considering what we get?". Then, according to the simulation results, experiments can be done on a physical setup of the proposed system as future work.

1.2 Literature Review

Hundreds of years before, Da Vinci [1] performed several observations outlined about birds. Since then, examining animal behavior has been the subject of extensive research for flight control, and flying animals have inspired scientists and engineers to design concepts for aerial vehicles. According to Tobalske [2], hovering and intermittent flight, two aspects of bird movement, hold enormous promise for the creation of autonomous flying robots in the future.

In 1970, Camhi [3, 4] stated that several mechanisms underlie the locust's flight, one of which is a central neuronal pattern generator that determines the sequence of wing-muscle contractions. He recorded the magnitude of abdominal and head movements of the insect induced by wind angle and observed the relation between them. The results show that for each experiment, the head, abdomen, and legs movements are correlated, and the receptors on the head provide information for the activities of the abdomen and legs in yaw correction.

Then, Gewecke and Philippen [5] investigated the aerodynamic output, the torque produced by the aerodynamic drag of the deflected abdomen, of tethered flying locusts in front of the wind tunnel to specify the impact of the abdominal reflexes in flight control. Baader [6] analyzed the posture of the abdomen during flight and pointed out interneurons that are in charge of controlling abdominal reflexes. Zanker [7], performed an experiment on tethered flying *Drosophila melanogaster* (Fig. 1.1a) and investigated the lateral abdomen deflections in response to visual stimuli for flight control. Frye [8] carried out an experiment with male and female *Manduca sexta* (Fig. 1.1b) during tethered flight within a wind tunnel setup and recorded abdominal deflections with sensors.

(a) *Drosophila melanogaster* (b) *Manduca sexta*

Figure 1.1: Flying locusts

Hedrick and Daniel [9] reported that Hawkmoths' abdomens are a sizeable portion of their overall mass and may contribute to shifting the moment produced by wing forces. Moreover, they constructed a mathematical model of *Manduca sexta* including the angle between the thorax and abdomen to simulate flight control. Dyhr et al. [10] experimented on *Manduca sexta* to observe visual-abdominal reflexes and developed a mathematical model with the thoracic–abdominal joint suggesting a new morphology that can be used redirecting thrust forces in flight control. Demir et al. [11] applied this new mechanism to a quadrotor with a classical control technique, PD control, and showed that the stability performance of a quadrotor could be improved by inertially redirecting wing forces using abdomen-like appendage inertia. Ugurlu et al. [12] designed a controller based on reinforcement learning for a bi-rotor platform with a tail appendage and compared it with classical control approaches.

On the other hand, several studies apply different control techniques to aerial vehicles to improve their stability. In literature, PID and LQR controllers are the most used techniques for aerial vehicles [13–15]. Bouabdallah [16] developed five controllers; Lyapunov-based, PID, LQ, backstepping, and sliding mode concepts. In recent years, with the improvement in computational power in microprocessors, several studies have been published using MPC to control UAVs [17–22]. Notter et al. [23] compared the MPC performance of the multirotor vehicle with a heavy slung load with the LQR approach. Cai et al. [24] combined the MPC algorithm with the feedback linearization technique.

The drawback of linear control approaches such as PID, LQR, and MPC is that they can stabilize unmanned aerial vehicles around the equilibrium point. As the states go far from equilibrium, the control performance degrades because of the nonlinear characteristics of the plant. Adaptive model predictive control (A-MPC) addresses this degradation by adapting the prediction model for changing operating conditions. In literature, A-MPC is applied with various methods. Pereida et al. [25] combined model predictive control with $\mathcal{L}_1$ adaptive controller for trajectory tracking. Tanaskovic et al. [26] divided the A-MPC approach into two steps: real-time system identification based on input-output data and formulation of robust finite-horizon optimal control problem. Lorenzen et al. [27] used past state values and inputs to update the model with guaranteed constraint satisfaction.

Furthermore, motion planning for UAVs is challenging, and numerous approaches have been developed recently. Goerzen et al. [28], provided an overview of the motion planning algorithms for UAVs and stated the challenges of the motion planning of UAVs compared to mobile robots or manipulators in terms of the difficulties about the differential constraints, unknown aerodynamic disturbances, limited knowledge about the environment, limited sensor capabilities, etc. There is comprehensive literature for path planning of UAVs, including heuristic and sample-based approaches such as A*, D*, ARA* [29–31]. Yang and LaValle [32] presented a sampling-based neighborhood graph (SNG) approach to execute feedback-motion planning by covering free configuration space with balls. Karagöz et al. [33] addressed that covering the free space with rectangular regions is more effective than the circular regions in terms of the sparsity of the graph structure. Atasoy [34] improved the algorithm and applied it to the unmanned surface vehicle (USV) models with a nonlinear MPC control strategy for collision avoidance.

1.3 Contributions

A preliminary version of the quadrotor structure with an actively controlled appendage inertia was presented by Demir et al. [11]. In this thesis, we comprehensively analyze the impact of the appendage in both the sagittal plane and 3D space. The main contributions are listed as follows;

- We constructed the mathematical model of the bi-rotor platform with an appendage in the sagittal plane, considering the hard and soft constraints.

- Then, we took our mathematical model one step further by applying the proposed structure to the conventional quadrotor in 3D space. In contrast to the previous model, we assumed that the appendage has 2-DOF, representing roll and pitch rotation in the appendage frame.

- We designed LQR for both models and compared their performances with conventional aerial vehicles. To make a fair comparison, we eliminated the weighting parameters of the states and the control effort that belong to the appendage. Then, we compared the systems' performances with different weighting parameters in terms of settling time, steady-state error, and the average cost value of the quadratic cost function.

- Since animals have highly actuated muscles, we tried to examine whether the appendage with significant torque-limit constraint still improves the performance or not. Also, we added soft and hard constraints for the appendage angles and compared the results with the conventional systems.

- We improved the controller performance by designing MPC, which is well suited for multi-input multi-output (MIMO) and highly nonlinear systems with constraints. We compared constrained LQR and MPC responses for initially perturbed systems.

- To increase the performance of MPC, we implemented A-MPC by linearizing the plant model at each prediction step. We analyzed the A-MPC response with the initial state values far from the nominal operating point and compared it with MPC.

- The final contribution relates to a sampling-based feedback motion planning algorithm with A-MPC policy in a planar region. We aimed to plan collision-free motion by using A-MPC with hard position constraints. We performed Monte Carlo simulations with different initial conditions and input noise to test our algorithm.

1.4 The Outline of the Thesis

The organization of the thesis is as follows. Chapter 1 gives information about the motivation of the proposed aerial vehicle configuration. In addition, we provide a literature review and contributions. The advantages, disadvantages, and challenging parts of this structure are discussed.

Chapter 2 explains the nonlinear mathematical model of the bi-rotor platform with an abdomen-like appendage. The equations of motion of the aerial vehicle are derived based on the Euler-Lagrange method in planar space. We explain the assumptions used in the modeling and constraints of the system. Furthermore, linearization around the equilibrium point and the state space representation is given in this chapter.

Chapter 3 takes the analysis to the next level by deriving the mathematical model of the conventional quadrotor with the Newton-Euler approach and expanding it to the proposed structure with an actively controlled 2-DOF abdomen-like appendage dynamics in 3D space.

After deriving the dynamical model of the systems, Chapter 4 gives a background for optimization-based controller designs; LQR, MPC, and A-MPC. It starts with explaining the scaling state space model, which is beneficial for weight selections, and then expresses the controllers step by step.

Chapter 5 discusses the recently published motion planning algorithm called "MPC-Graph" and its implementation on the proposed aerial vehicle in a planar region.

We present the simulation results and analyze the systems' performances in Chapter 6. We compare the controllers in terms of performance criteria and constraints.

Finally, Chapter 7 outlines our work and the concluding remarks on the results. In addition, we discuss future work and extensions of the proposed study.

CHAPTER 2

PLANAR DYNAMICAL SYSTEM MODELING

This chapter develops the mathematical model of the proposed aerial vehicle with an actively controlled abdomen-like appendage in the x-z plane. Fig. 2.1 illustrates the mathematical model of the hawkmoth *Manduca sexta* in the sagittal plane. The thorax and head of the animal are considered as a single body with a mass of M, for simplicity. The mass of the abdomen is denoted by m, and the abdominal joint connects the abdomen to the thorax. The body angle, θ_1, is defined as the pitch angle of the body mass. The abdomen angle, θ_2, represents the angle deviation of the abdomen from the x axis.

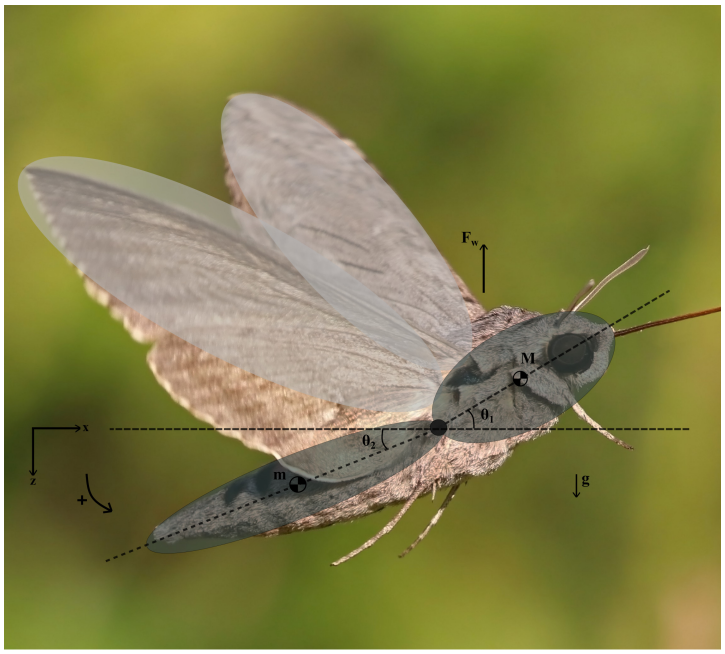

Figure 2.1: Hawkmoth *Manduca sexta* and the illustrated mathematical model in the sagittal plane.

The proposed system, inspired by the mathematical model of the hawkmoth, has two propellers (bi-rotor) and an abdomen-like appendage mounted on the bottom of the body. Conventional bi-rotor platform (Fig. 2.2a) has 3-DOF, (x, z, θ_1), whereas the platform with appendage has additional 1-DOF, which is the appendage angle θ_2 shown in Fig. 2.2b.

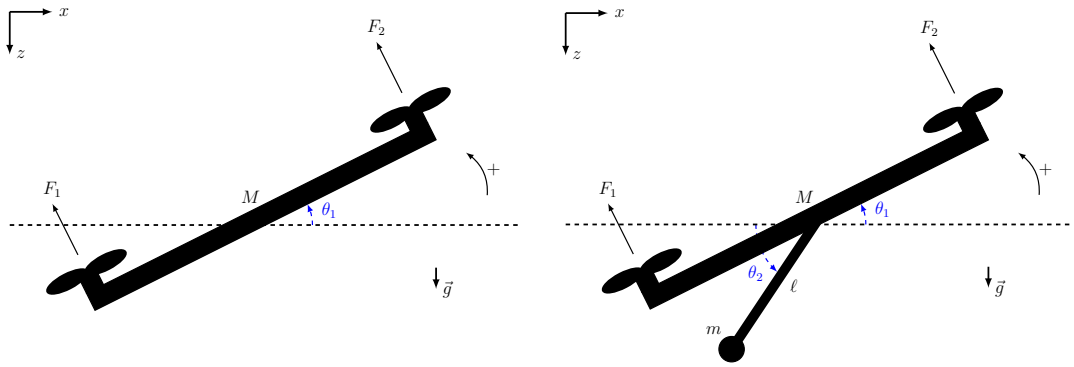

(a) The conventional bi-rotor platform. It has 3-DOF, translational movement in x and z direction, and orientation of the body, θ_1.

(b) The proposed bi-rotor platform with an abdomen-like appendage. It has an additional 1-DOF, which is the angle of the appendage, θ_2.

Figure 2.2: Bi-rotor platforms in the sagittal plane.

We begin our derivation with the nonlinear model of the conventional bi-rotor platform. Then, we expand the equations of motion to the proposed bi-rotor platform with an abdomen-like appendage. We obtain the mathematical models with respect to a fixed planar world frame whose axes are denoted as x and z. Accordingly, the gravitational force is acting along the z direction. We use the Euler-Lagrange approach to develop equations of motion of the vehicles.

Before deriving the equations of motion, we made the following assumptions for simplification;

- The structure of the vehicles is supposed as rigid and symmetrical.
- The appendage is assumed as mounted on the bottom of the body. Therefore, the distance between the CoG of the body and the abdominal joint is half of the body height, illustrated in Fig. 2.3.
- The appendage is considered an actively controlled pendulum with point mass,

and we assume that the pendulum rod is weightless.

- The body axes of the vehicle coincide with the axes of inertia.

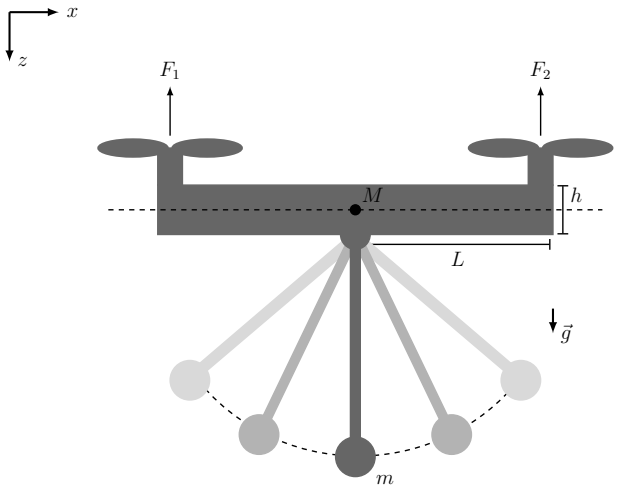

Figure 2.3: Illustration of the appendage motion and the abdominal joint

2.1 Conventional Bi-rotor Platform

As stated before, the conventional bi-rotor platform has 3-DOF, in which the state and the input variables are denoted as follows;

$$\begin{aligned} q &= \begin{bmatrix} x & z & \theta_1 \end{bmatrix}^T, \\ u &= \begin{bmatrix} F_1 & F_2 \end{bmatrix}^T, \end{aligned} \tag{2.1}$$

where x and z represent the translational movements in planar space and θ_1 is the body angle illustrated in Fig. 2.2a. The input vector consists of the thrust forces F_1 and F_2. Then, the position of the body and its first derivative are represented as;

$$\vec{r}_M = \begin{bmatrix} x & z \end{bmatrix}^T, \qquad \dot{\vec{r}}_M = \begin{bmatrix} \dot{x} & \dot{z} \end{bmatrix}^T. \tag{2.2}$$

Based on the Euler-Lagrange approach, the Lagrange equation is

$$\frac{d}{dt}\left(\frac{\partial L}{\partial \dot{q}}\right) - \frac{\partial L}{\partial q} = Q, \tag{2.3}$$

where the Lagrangian (L) is defined as the difference between the kinetic energy and potential energy of the system. The notation Q denotes the external forces of the system. The kinetic energy (T) and potential energy (V) are expressed as follows;

$$T = \frac{1}{2}M(\dot{x}^2 + \dot{z}^2) + \frac{1}{2}I_M\dot{\theta}_1^2, \tag{2.4}$$

$$V = Mgz. \tag{2.5}$$

Here, M is the body mass, and I_M is the moments of inertia of the body. By applying the Lagrange equation, we obtain nonlinear dynamic equations below;

$$M\ddot{x} = -(F_1 + F_2)\mathbf{s}_{\theta_1}, \tag{2.6}$$

$$M\ddot{z} + Mg = (F_1 + F_2)\mathbf{c}_{\theta_1}, \tag{2.7}$$

$$I_M\ddot{\theta}_1 = (F_2 - F_1)\frac{L}{2}. \tag{2.8}$$

Moreover, Euler-Lagrange equations of the nonlinear system can be expressed in the form of

$$M(q)\ddot{q} + C(q, \dot{q}) + N(q) = T + \Gamma. \tag{2.9}$$

The matrix $M(q)$ is called a mass matrix of the system and includes inertial terms. $C(q, \dot{q})$ is composed of the Coriolis terms with constraints and $N(q)$ includes the gravitational terms. The right-hand side of the equation is combined with external torques, T, and external forces Γ. Therefore, the matrix representation of the dynamic model can be formed as follows;

$$\underbrace{\begin{bmatrix} M & 0 & 0 \\ 0 & M & 0 \\ 0 & 0 & I_M \end{bmatrix}}_{M(q)} \begin{bmatrix} \ddot{x} \\ \ddot{z} \\ \ddot{\theta}_1 \end{bmatrix} + \underbrace{\begin{bmatrix} 0 \\ Mg \\ 0 \end{bmatrix}}_{N(q)} = \underbrace{\begin{bmatrix} -(F_1 + F_2)\mathbf{s}_{\theta_1} \\ (F_1 + F_2)\mathbf{c}_{\theta_1} \\ (F_2 - F_1)\frac{L}{2} \end{bmatrix}}_{T+\Gamma}. \tag{2.10}$$

2.2 Bi-rotor Platform with 1-DOF Abdomen-Like Appendage

The proposed system is equipped with an actively controlled 1-DOF abdomen-like appendage as indicated in Fig. 2.3. The joint between the body and the appendage is at the bottom center of the body. The mass and the appendage's length are denoted as m and ℓ, respectively. The new state variable related to the joint is represented as θ_2. The joint torque, τ, is added to the input vector as a control input to the system. The new states and input vector of the nonlinear system are as follows;

$$\begin{aligned} q &= \begin{bmatrix} x & z & \theta_1 & \theta_2 \end{bmatrix}^T, \\ u &= \begin{bmatrix} F_1 & F_2 & \tau \end{bmatrix}^T. \end{aligned} \tag{2.11}$$

To derive the nonlinear dynamic equations, we need to define the position of the bi-rotor body and the appendage as stated below;

$$\vec{r}_M = \begin{bmatrix} x \\ z \end{bmatrix}, \qquad \vec{r}_m = \begin{bmatrix} x - \ell \mathbf{c}_{\theta_2} + \frac{h}{2}\mathbf{s}_{\theta_1} \\ z - \ell \mathbf{s}_{\theta_2} - \frac{h}{2}\mathbf{c}_{\theta_1} \end{bmatrix}, \tag{2.12}$$

where $\vec{r}_M$ and $\vec{r}_m$ are the position vectors of the body and the appendage, respectively. Taking the first derivative of the position vectors, we obtain velocity vectors of the body and appendage;

$$\dot{\vec{r}}_M = \begin{bmatrix} \dot{x} \\ \dot{z} \end{bmatrix}, \qquad \dot{\vec{r}}_m = \begin{bmatrix} \dot{x} + \ell \mathbf{s}_{\theta_2}\dot{\theta}_2 + \frac{h}{2}\mathbf{c}_{\theta_1}\dot{\theta}_1 \\ \dot{z} - \ell \mathbf{c}_{\theta_2}\dot{\theta}_2 + \frac{h}{2}\mathbf{s}_{\theta_1}\dot{\theta}_1 \end{bmatrix}. \tag{2.13}$$

Then, we calculate the kinetic and potential energy of the system to apply the Euler-Lagrange approach;

$$\begin{aligned} T &= \frac{1}{2}m\ \dot{\vec{r}}_m^{\,2} + \frac{1}{2}M\ \dot{\vec{r}}_M^{\,2} + \frac{1}{2}I_M\dot{\theta}_1^2, \\ &= \frac{1}{2}(M+m)(\dot{x}^2+\dot{z}^2) + \frac{1}{2}m\ell^2\dot{\theta}_2^{\,2} + \frac{1}{2}\left(\frac{mh^2}{4} + I_M\right)\dot{\theta}_1^2 \\ &+ m\ell\dot{x}\mathbf{s}_{\theta_2}\dot{\theta}_2 + \frac{1}{2}mh\dot{x}\mathbf{c}_{\theta_1}\dot{\theta}_1 + m\ell\frac{h}{2}\mathbf{c}_{\theta_1}\mathbf{s}_{\theta_2}\dot{\theta}_1\dot{\theta}_2 \\ &- m\ell\dot{z}\mathbf{c}_{\theta_2}\dot{\theta}_2 + m\frac{h}{2}\dot{z}\mathbf{s}_{\theta_1}\dot{\theta}_1 - m\ell\frac{h}{2}\mathbf{s}_{\theta_1}\mathbf{c}_{\theta_2}\dot{\theta}_1\dot{\theta}_2, \end{aligned} \tag{2.14}$$

$$V = (M+m)gy + mg\ell(1-\mathbf{s}_{\theta_2}) - mg\frac{h}{2}\mathbf{c}_{\theta_1}. \tag{2.15}$$

By using the formulation (2.3), we obtain four Lagrange equations for each state variable listed below;

x:

$$\begin{aligned}\frac{d}{dt}\left[(M+m)\dot{x}+m\ell\mathbf{s}_{\theta_2}\dot{\theta}_2+\frac{1}{2}mh\mathbf{c}_{\theta_1}\dot{\theta}_1\right]-0=Q_1,\\ (M+m)\ddot{x}+m\ell\mathbf{s}_{\theta_2}\ddot{\theta}_2+m\ell\mathbf{c}_{\theta_2}\dot{\theta}_2^2+\frac{1}{2}mh\mathbf{c}_{\theta_1}\ddot{\theta}_1-\frac{1}{2}mh\mathbf{s}_{\theta_1}\dot{\theta}_1^2=Q_1.\end{aligned} \tag{2.16}$$

z:

$$\begin{aligned}\frac{d}{dt}\left[(M+m)\dot{z}-m\ell\mathbf{c}_{\theta_2}\dot{\theta}_2+\frac{1}{2}mh\mathbf{s}_{\theta_1}\dot{\theta}_1\right]+(M+m)g=Q_2,\\ (M+m)(\ddot{z}+g)-m\ell\mathbf{c}_{\theta_2}\ddot{\theta}_2+m\ell\mathbf{s}_{\theta_2}\dot{\theta}_2^2+\frac{1}{2}mh\mathbf{s}_{\theta_1}\ddot{\theta}_1+\frac{1}{2}mh\mathbf{c}_{\theta_1}\dot{\theta}_1^2=Q_2.\end{aligned} \tag{2.17}$$

$\boldsymbol{\theta_1}$:

$$\begin{aligned}&\frac{d}{dt}\left[\left(I_M+\frac{mh^2}{4}\right)\dot{\theta}_1+m\dot{x}\frac{h}{2}\mathbf{c}_{\theta_1}+m\ell\frac{h}{2}\mathbf{c}_{\theta_1}\mathbf{s}_{\theta_2}\dot{\theta}_2+m\dot{z}\frac{h}{2}\mathbf{s}_{\theta_1}-m\ell\frac{h}{2}\mathbf{c}_{\theta_2}\mathbf{s}_{\theta_1}\dot{\theta}_2\right]\\ &-\left[-m\dot{x}\frac{h}{2}\mathbf{s}_{\theta_1}\dot{\theta}_1-m\ell\frac{h}{2}\mathbf{s}_{\theta_1}\mathbf{s}_{\theta_2}\dot{\theta}_1\dot{\theta}_2+m\dot{z}\frac{h}{2}\mathbf{c}_{\theta_1}\dot{\theta}_1-m\ell\frac{h}{2}\mathbf{c}_{\theta_1}\mathbf{c}_{\theta_2}\dot{\theta}_1\dot{\theta}_2-mg\frac{h}{2}\mathbf{s}_{\theta_1}\right]=Q_3,\\ &\left(I_M+\frac{mh^2}{4}\right)\ddot{\theta}_1+m\frac{h}{2}\left(\ddot{x}\mathbf{c}_{\theta_1}+(\ddot{z}+g)\mathbf{s}_{\theta_1}+\ell\ddot{\theta}_2(\mathbf{c}_{\theta_1}\mathbf{s}_{\theta_2}-\mathbf{c}_{\theta_2}\mathbf{s}_{\theta_1})+\ell\dot{\theta}_2^2(\mathbf{c}_{\theta_1}\mathbf{c}_{\theta_2}+\mathbf{s}_{\theta_2}\mathbf{s}_{\theta_1})\right)=Q_3.\end{aligned} \tag{2.18}$$

$\boldsymbol{\theta_2}$:

$$\begin{aligned}&\frac{d}{dt}\left[m\ell^2\dot{\theta}_2+m\dot{x}\ell\mathbf{s}_{\theta_2}+m\ell\frac{h}{2}\mathbf{c}_{\theta_1}\mathbf{s}_{\theta_2}\dot{\theta}_1-m\dot{z}\ell\mathbf{c}_{\theta_2}-m\ell\frac{h}{2}\mathbf{c}_{\theta_2}\mathbf{s}_{\theta_1}\dot{\theta}_1\right]\\ &-\left[m\dot{x}\ell\mathbf{c}_{\theta_2}\dot{\theta}_2+m\ell\frac{h}{2}\mathbf{c}_{\theta_1}\mathbf{c}_{\theta_2}\dot{\theta}_1\dot{\theta}_2+m\dot{z}\ell\mathbf{s}_{\theta_2}\dot{\theta}_2+m\ell\frac{h}{2}\mathbf{s}_{\theta_2}\mathbf{s}_{\theta_1}\dot{\theta}_1\dot{\theta}_2+mg\ell\mathbf{c}_{\theta_2}\right]=Q_4,\\ &m\ell^2\ddot{\theta}_2+m\ell\left(\ddot{x}\mathbf{s}_{\theta_2}-(\ddot{z}+g)\mathbf{c}_{\theta_2}\right)+\frac{1}{2}m\ell h\left((\mathbf{c}_{\theta_1}\mathbf{s}_{\theta_2}-\mathbf{c}_{\theta_2}\mathbf{s}_{\theta_1})\ddot{\theta}_1-(\mathbf{s}_{\theta_1}\mathbf{s}_{\theta_2}+\mathbf{c}_{\theta_1}\mathbf{c}_{\theta_2})\dot{\theta}_1^2\right)=Q_4.\end{aligned} \tag{2.19}$$

The external forces denoted on the right-hand side of the equations are expressed by the input variables;

$$Q=\begin{bmatrix}Q_1\\Q_2\\Q_3\\Q_4\end{bmatrix}=\begin{bmatrix}-(F_1+F_2)\mathbf{s}_{\theta_1}\\(F_1+F_2)\mathbf{c}_{\theta_1}\\(F_2-F_1)\frac{L}{2}\\\tau\end{bmatrix}. \tag{2.20}$$

For the next step, let us construct a new state vector as

$$v = \begin{bmatrix} v_1 & v_2 \end{bmatrix}^T, \tag{2.21}$$

where

$$v_1 = \begin{bmatrix} x & z & \theta_1 & \theta_2 \end{bmatrix}^T, \qquad v_2 = \begin{bmatrix} \dot{x} & \dot{z} & \dot{\theta}_1 & \dot{\theta}_2 \end{bmatrix}^T. \tag{2.22}$$

Therefore, the equations of motion of the nonlinear model can be expressed as the four-first order equations by using the form of the equation (2.9);

$$\dot{v} = f(v,u) = \begin{bmatrix} v_2 \\ M(v_1)^{-1}[T + \Gamma - C(v_1, v_2) - N(v_1)] \end{bmatrix}, \tag{2.23}$$

with the matrices below;

$$M = \begin{bmatrix} (M+m) & 0 & m\frac{h}{2}\mathbf{c}_{\theta_1} & m\ell\mathbf{s}_{\theta_2} \\ 0 & (M+m) & m\frac{h}{2}\mathbf{s}_{\theta_1} & -m\ell\mathbf{c}_{\theta_2} \\ m\frac{h}{2}\mathbf{c}_{\theta_1} & m\frac{h}{2}\mathbf{s}_{\theta_1} & I_M + \frac{mh^2}{4} & m\ell\frac{h}{2}\mathbf{s}_{(\theta_2-\theta_1)} \\ m\ell\mathbf{s}_{\theta_2} & -m\ell\mathbf{c}_{\theta_2} & m\ell\frac{h}{2}\mathbf{s}_{(\theta_2-\theta_1)} & m\ell^2 \end{bmatrix}, \tag{2.24}$$

$$N(q) = \begin{bmatrix} 0 \\ (M+m)g \\ mg\frac{h}{2}\mathbf{s}_{\theta_1} \\ -mg\ell\mathbf{c}_{\theta_2} \end{bmatrix}, \tag{2.25}$$

$$C(q,\dot{q}) = \begin{bmatrix} -m\ell\mathbf{c}_{\theta_2}\dot{\theta_2}^2 - \frac{1}{2}mh\mathbf{s}_{\theta_1}\dot{\theta_1}^2 \\ m\ell\mathbf{s}_{\theta_2}\dot{\theta_2}^2 + \frac{1}{2}mh\mathbf{c}_{\theta_1}\dot{\theta_1}^2 \\ \frac{1}{2}m\ell h\mathbf{c}_{(\theta_2-\theta_1)}\dot{\theta_2}^2 \\ -\frac{1}{2}m\ell h\mathbf{c}_{(\theta_2-\theta_1)}\dot{\theta_1}^2 \end{bmatrix}, \tag{2.26}$$

$$T + \Gamma = \begin{bmatrix} -(F_1+F_2)\mathbf{s}_{\theta_1} \\ (F_1+F_2)\mathbf{c}_{\theta_1} \\ (F_2-F_1)\frac{L}{2} \\ \tau \end{bmatrix}. \tag{2.27}$$

2.3 Linearization

Khalil [35] states that as we move from linear to nonlinear systems, the superposition principle no longer holds, and analysis tools involve more advanced mathematics. A common practice in analyzing nonlinear systems is linearizing them about some nominal operating point. For nonlinear systems, a set of equilibrium points may exist. The equilibrium points of the system are determined by setting $f(x, u) = 0$.

Therefore, we linearize the nonlinear equations of the systems around the hovering state. Since the equilibrium point of the conventional bi-rotor platform is translation invariant, initial x and z states can be anything expressed by the following equilibrium states and input vector;

$$\begin{aligned} x_e &= \begin{bmatrix} x_0 & z_0 & 0 & 0 & 0 & 0 \end{bmatrix}^T, \\ u_e &= \begin{bmatrix} \frac{Mg}{2} & \frac{Mg}{2} \end{bmatrix}^T, \end{aligned} \tag{2.28}$$

where

$$\dot{x}_e = f(x_e, u_e) = 0. \tag{2.29}$$

The hover condition is satisfied when thrust force is equal to body weight, meaning that the system preserves its altitude. Examining the linearization at that point allows us to use linear control theory to design controllers that operate properly around the equilibrium region. We form the state space equation of the nonlinear model linearized around the equilibrium point as;

$$\dot{\bar{x}} = A\bar{x} + B\bar{u}, \tag{2.30}$$

where A, B matrices and the new state and input vector $\bar{x}$, $\bar{u}$ are defined as below;

$$\begin{aligned} A &= \left.\frac{\partial f(x,u)}{\partial x}\right|_{x_e,u_e}, & B &= \left.\frac{\partial f(x,u)}{\partial u}\right|_{x_e,u_e}, \\ \bar{x} &= x - x_e, & \bar{u} &= u - u_e. \end{aligned} \tag{2.31}$$

Therefore, A and B matrices are obtained as follows for the conventional bi-rotor platform;

$$A = \left[\begin{array}{ccc|c} \multicolumn{3}{c|}{\mathbf{0}_{3x3}} & \mathbf{I}_{3x3} \\ \hline 0 & 0 & -\frac{(F_1+F_2)}{M} & \\ 0 & 0 & 0 & \mathbf{0}_{3x3} \\ 0 & 0 & 0 & \end{array}\right], \qquad B = \left[\begin{array}{c} \mathbf{0}_{4x2} \\ \hline \frac{1}{M} \quad \frac{1}{M} \\ -\frac{L}{2I_M} \quad \frac{L}{2I_M} \end{array}\right]. \tag{2.32}$$

The proposed bi-rotor structure with an actively controlled abdomen-like appendage is also linearized around the hovering state with the following equilibrium state and input vectors;

$$\begin{aligned} x_e &= \begin{bmatrix} x_0 & z_0 & 0 & \frac{\pi}{2} & 0 & 0 & 0 & 0 \end{bmatrix}^T, \\ u_e &= \begin{bmatrix} \frac{(M+m)g}{2} & \frac{(M+m)g}{2} & 0 \end{bmatrix}^T. \end{aligned} \tag{2.33}$$

By using MATLAB Symbolic Toolbox, A and B matrices are found as;

$$A = \left[\begin{array}{cccc|c} \multicolumn{4}{c|}{\mathbf{0}_{4x4}} & \mathbf{I}_{4x4} \\ \hline 0 & 0 & -\frac{(M+m)g}{M} & \frac{mg}{M} & \\ 0 & 0 & 0 & 0 & \\ 0 & 0 & -\frac{mgh}{2I_M} & \frac{mgh}{2I_M} & \mathbf{0}_{4x4} \\ 0 & 0 & \frac{(M+m)g}{M\ell} + \frac{mgh^2}{4\ell I_M} & -\frac{(M+m)g}{M\ell} - \frac{mgh^2}{4\ell I_M} & \end{array}\right], \tag{2.34}$$

$$B = \left[\begin{array}{ccc} \multicolumn{3}{c}{\mathbf{0}_{4x3}} \\ \hline 0 & 0 & -\frac{1}{M\ell} \\ \frac{1}{(M+m)} & \frac{1}{(M+m)} & 0 \\ -\frac{L}{2I_M} & \frac{L}{2I_M} & -\frac{h}{2\ell I_M} \\ \frac{hL}{4\ell I_M} & -\frac{hL}{4\ell I_M} & \frac{h^2}{4\ell^2 I_M} + \frac{(M+m)}{Mm\ell^2} \end{array}\right]. \tag{2.35}$$

We also assumed that all state variables are measurable for conventional and proposed bi-rotor platforms. Thus, the matrix C is the identity matrix, I_{nxn} with n states. For the controllability and observability properties of the systems, we can analyze controllability $(\mathcal{C})$ and observability $(\mathcal{O})$ matrices formed as;

$$\mathcal{C} = \begin{bmatrix} B & AB & A^2B & \dots & A^{n-1}B \end{bmatrix}, \tag{2.36}$$

$$\mathcal{O} = \begin{bmatrix} C \\ CA \\ CA^2 \\ \vdots \\ CA^{n-1} \end{bmatrix}. \tag{2.37}$$

For both of the systems, $(\mathcal{C})$ and $(\mathcal{O})$ are found as full rank matrices by using MATLAB Symbolic Toolbox [36]. Therefore, the conventional and proposed bi-rotor vehicles are both controllable and observable.

CHAPTER 3

3D DYNAMICAL SYSTEM MODELING

3.1 3D Dynamical Modeling

This chapter demonstrates the nonlinear mathematical model of the proposed quadrotor configuration with an actively controlled 2-DOF abdomen-like appendage in 3D space. We begin our derivation with the conventional structure and then move to the proposed model as we did in Chapter 2.

First, we give the definitions of the reference frames used in the derivations. Then, we derive equations of motion of the 6-DOF conventional quadrotor body dynamics using the Newton-Euler approach. After that, we add the 2-DOF appendage dynamics to the equations of the conventional quadrotor and derive the resulting 8-DOF model, illustrated in Fig.3.1. Then, we linearize the nonlinear models at the hovering state.

3.1.1 Reference Frames

Analysis and control of the aerial vehicles involve various coordinate frames and the transformations between them. For instance, gyroscopes are inertial sensors that measure motion relative to an inertial frame of reference; the position and velocity of the vehicle can be given with respect to the Earth-centered, Earth-fixed (ECEF) frame. Therefore, we need to transform these quantities from different reference frames to the same frame to derive the equations of motion. The reference frames used in the derivation of the mathematical models are defined as follows:

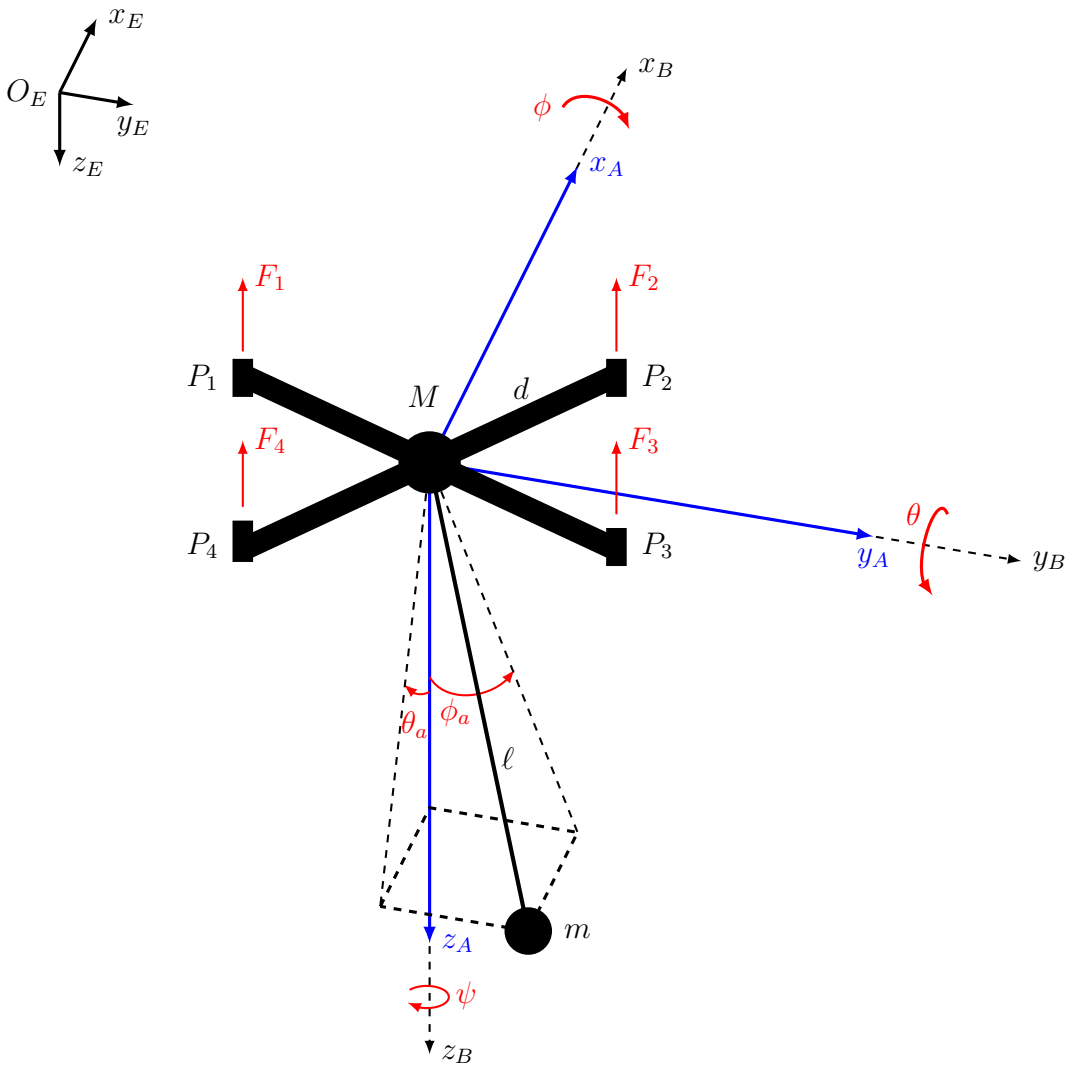

Figure 3.1: Illustration of the quadrotor with 2-DOF abdomen-like appendage. The appendage frame axes coincide with the body frame. The pendulum has 2-DOF, roll and pitch angles of the appendage, denoted as ϕ_a and θ_a, respectively.

- **Earth Frame (E):** Earth frame $\{E\} = \{x_E, y_E, z_E\}$ is defined to be rotating along with the Earth at a rate ω_{ie}^e. The frame's origin is at the center of the mass of the Earth. The z_E axis is along the direction of the gravitational force $\vec{g}$. The x_E axis points out the north, and the y axis completes a right-handed system.

- **Body Frame (B):** The body frame $\{B\} = \{x_B, y_B, z_B\}$ is fixed to the quadrotor body, and the origin of the body frame is at the center of mass of the body. The body frame is aligned with the axes of the inertial frame such that x_B points

out north and z_B points out the center of gravity.

- **Appendage Frame (A):** The appendage frame $\{A\} = \{x_A, y_A, z_A\}$ is established to derive the position of the appendage in the earth frame. The frame's origin coincides with the body frame, and the directions of the axes are parallel to the axes of the earth frame.

- **Propeller Frame (P):** The propeller frame $\{P\} = \{x_P, y_P, z_P\}$ is expressed in the reference frame of rotor i, and the frame axes are defined in the direction of the axes of the earth frame.

Each coordinate frame defined above is an orthogonal, right-handed coordinate frame. In this study, we assume the earth frame is a non-rotating fixed frame and neglect the earth rate ω_{ie}^{e}.

The conventional and the proposed quadrotor models rely on the following assumptions for simplification;

- The structure of the quadrotor is supposed as rigid and symmetrical.
- The center of mass of the quadrotor and the origin of the body frame coincide.
- The abdominal joint and the body's center of mass coincide with the origin of the body frame.
- The propellers have rigid body dynamics.
- The thrust and drag of each motor are proportional to the square of the motor velocity.
- The appendage is considered a 2-DOF point mass pendulum.
- We ignore the aerodynamic effects such as hub force, hub moment, and ground effect in the dynamical model.
- We assumed that the products of inertia of the quadrotor body are equal to zero, $J_{xy} = J_{yz} = J_{xz} = 0$.

3.1.2 Kinematic Equations of Quadrotor

Kinematics is the study of representing the positions and orientations of rigid objects without considering the forces and torques acting on them. It deals with the transformations of various coordinate frames that define the vehicle's position. We begin to derive kinematics of the conventional quadrotor by defining the generalized coordinates of the body that describes 6-DOF motion in 3D space;

$$q = \begin{bmatrix} x^E & y^E & z^E & \phi & \theta & \psi & V_x^E & V_y^E & V_z^E & p^B & q^B & r^B \end{bmatrix}^T, \tag{3.1}$$

where (x^E, y^E, z^E) and (V_x^E, V_y^E, V_z^E) express the position and linear velocities of the quadrotor with respect to the earth frame, respectively. (ϕ, θ, ψ) are the Euler angles that transform the body frame to the Earth frame. Lastly, (p^B, q^B, r^B) represents the angular rate of the quadrotor in the body frame.

Euler angles are defined in different frames, depicted in Fig. 3.2. The first frame is the body frame, and the roll (ϕ) angle is produced by rotating the body frame about its x-axis by the amount of ϕ. The resultant frame is denoted as F'. The frame F' is rotated on its y-axis by the amount of pitch angle θ, and the next frame is named F''. As a final step, rotating the frame F'' about its z-axis by the amount of yaw angle ψ gives us the earth frame.

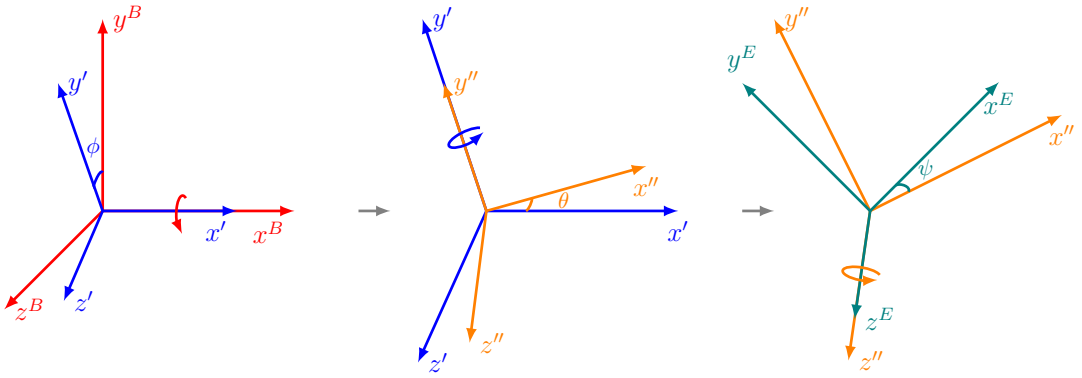

Figure 3.2: Representation of three successive rotations (x-y-z) of the body frame and the related Euler angles.

Therefore, we define the rotation matrices by using Euler angles as follows;

$$
\begin{aligned}
R_B^{F'}(x,\phi) &= \begin{bmatrix} 1 & 0 & 0 \\ 0 & \mathbf{c}_\phi & -\mathbf{s}_\phi \\ 0 & \mathbf{s}_\phi & \mathbf{c}_\phi \end{bmatrix}, \\
R_{F'}^{F''}(y,\theta) &= \begin{bmatrix} \mathbf{c}_\theta & 0 & \mathbf{s}_\theta \\ 0 & 1 & 0 \\ -\mathbf{s}_\theta & 0 & \mathbf{c}_\theta \end{bmatrix}, \\
R_{F''}^{E}(z,\psi) &= \begin{bmatrix} \mathbf{c}_\psi & -\mathbf{s}_\psi & 0 \\ \mathbf{s}_\psi & \mathbf{c}_\psi & 0 \\ 0 & 0 & 1 \end{bmatrix}.
\end{aligned} \tag{3.2}
$$

Direction cosine matrix (DCM) from the body to the earth frame, C_B^E, is derived by successive multiplication of the rotation matrices defined in (3.2). The resulting DCM is as follows;

$$
\begin{aligned}
C_B^E &= R_{F''}^E(z,\psi) R_{F'}^{F''}(y,\theta) R_B^{F'}(x,\phi), \\
&= \begin{bmatrix} \mathbf{c}_\theta\mathbf{c}_\psi & \mathbf{s}_\phi\mathbf{s}_\theta\mathbf{c}_\psi - \mathbf{c}_\phi\mathbf{s}_\psi & \mathbf{c}_\phi\mathbf{s}_\theta\mathbf{c}_\psi + \mathbf{s}_\phi\mathbf{s}_\psi \\ \mathbf{c}_\theta\mathbf{s}_\psi & \mathbf{s}_\phi\mathbf{s}_\theta\mathbf{s}_\psi + \mathbf{c}_\phi\mathbf{c}_\psi & \mathbf{c}_\phi\mathbf{s}_\theta\mathbf{s}_\psi - \mathbf{s}_\phi\mathbf{c}_\psi \\ -\mathbf{s}_\theta & \mathbf{s}_\phi\mathbf{c}_\theta & \mathbf{c}_\phi\mathbf{c}_\theta \end{bmatrix}.
\end{aligned} \tag{3.3}
$$

Then, angular rates with respect to the body frame are derived using the Euler angles and rotation matrices as;

$$
\begin{aligned}
\begin{bmatrix} p \\ q \\ r \end{bmatrix} &= \begin{bmatrix} \dot\phi \\ 0 \\ 0 \end{bmatrix} + R_B^{F'}(x,-\phi) \begin{bmatrix} 0 \\ \dot\theta \\ 0 \end{bmatrix} + R_B^{F'}(x,-\phi) R_{F'}^{F''}(y,-\theta) \begin{bmatrix} 0 \\ 0 \\ \dot\psi \end{bmatrix}, \\
&= \begin{bmatrix} \dot\phi \\ 0 \\ 0 \end{bmatrix} + \begin{bmatrix} 1 & 0 & 0 \\ 0 & \mathbf{c}_\phi & \mathbf{s}_\phi \\ 0 & -\mathbf{s}_\phi & \mathbf{c}_\phi \end{bmatrix} \begin{bmatrix} 0 \\ \dot\theta \\ 0 \end{bmatrix} + \begin{bmatrix} 1 & 0 & 0 \\ 0 & \mathbf{c}_\phi & \mathbf{s}_\phi \\ 0 & -\mathbf{s}_\phi & \mathbf{c}_\phi \end{bmatrix} \begin{bmatrix} \mathbf{c}_\theta & 0 & -\mathbf{s}_\theta \\ 0 & 1 & 0 \\ \mathbf{s}_\theta & 0 & \mathbf{c}_\theta \end{bmatrix} \begin{bmatrix} 0 \\ 0 \\ \dot\psi \end{bmatrix}, \\
&= \underbrace{\begin{bmatrix} 1 & 0 & -\mathbf{s}_\theta \\ 0 & \mathbf{c}_\phi & \mathbf{c}_\theta\mathbf{s}_\phi \\ 0 & -\mathbf{s}_\phi & \mathbf{c}_\theta\mathbf{c}_\phi \end{bmatrix}}_{R_{pqr}} \begin{bmatrix} \dot\phi \\ \dot\theta \\ \dot\psi \end{bmatrix}.
\end{aligned} \tag{3.4}
$$

After obtaining the resultant matrix R_{pqr}, by taking the inverse of it, we can find the transformation matrix from angular rates to Euler rates as follows;

$$\begin{bmatrix} \dot{\phi} \\ \dot{\theta} \\ \dot{\psi} \end{bmatrix} = R_{pqr}^{-1} \begin{bmatrix} p \\ q \\ r \end{bmatrix}, \tag{3.5}$$

$$= \begin{bmatrix} 1 & \mathbf{s}_\phi \mathbf{t}_\theta & \mathbf{c}_\phi \mathbf{t}_\theta \\ 0 & \mathbf{c}_\phi & -\mathbf{s}_\phi \\ 0 & \frac{\mathbf{s}_\phi}{\mathbf{c}_\theta} & \frac{\mathbf{c}_\phi}{\mathbf{c}_\theta} \end{bmatrix} \begin{bmatrix} p \\ q \\ r \end{bmatrix}. \tag{3.6}$$

Notice that R_{pqr} is not a regular rotation matrix, nor satisfies its properties such that $R_{pqr}^{-1} \neq R_{pqr}^{T}$. Therefore, by combining the obtained kinematic equations, we get the equation below;

$$\begin{bmatrix} \dot{x} \\ \dot{y} \\ \dot{z} \\ \dot{\phi} \\ \dot{\theta} \\ \dot{\psi} \end{bmatrix} = \begin{bmatrix} I_{3x3} & 0_{3x3} \\ 0_{3x3} & R_{pqr} \end{bmatrix} \begin{bmatrix} V_x \\ V_y \\ V_z \\ p \\ q \\ r \end{bmatrix}. \tag{3.7}$$

3.1.3 Rigid Body Dynamics

This section expresses the dynamical equations of the quadrotor. Whereas the kinematic equations explain the motion of the quadrotor without considering forces and torques acting on the body, the dynamical equations directly define the relationship between the forces and motion. We derive the equations of motion by using the Newton-Euler formulation. In Chapter 2, we used the Euler-Lagrange approach for bi-rotor platforms by using a Lagrangian function defined as the difference between kinetic and potential energy. In contrast, in the Newton-Euler method, we derive the equations describing the linear motion and angular motion of the quadrotor separately. Both formulations give us the same result, and each has certain advantages. The Newton-Euler method is better for recursive computation compared to the Lagrangian formulation [37]. Although the Lagrangian approach has an advantage in simplicity, we move on with the Newton-Euler approach to use vector notation and

define motion based on forces for the mathematical modeling of the proposed aerial vehicle in 3D space.

The Newton-Euler method is based on the following statements [37];

- For every action, there is an equal and opposite reaction.
- The linear momentum change rate equals the total force applied to the quadrotor.
- The rate of change of the angular momentum equals the total torque acting on the quadrotor.

We begin writing the equations by stating Newton's second law, which describes the dynamic systems in terms of force and momentum, as follows;

$$\frac{d\vec{p}}{dt} \triangleq \vec{F}_{ext}, \qquad \frac{d\vec{h}}{dt} \triangleq \vec{\tau}_{ext}, \tag{3.8}$$

where $\vec{F}_{ext}$, $\vec{\tau}_{ext}$ are the external forces and torques that produce the motion of the quadrotor. According to the assumptions we made, translational equations of motion in the earth frame are written as follows;

$$\begin{bmatrix} \dot{V}_x \\ \dot{V}_y \\ \dot{V}_z \end{bmatrix} = \frac{\vec{F}^E_{ext}}{M} + \vec{G}^E. \tag{3.9}$$

Here, $\vec{G}^E = [0, 0, g]^T$ is the gravitational force vector defined in the earth frame.

We derive rotational equations with respect to the body frame. At this point, we need to consider the Coriolis effect. Since Newton's laws of motion explain the motion of an object in an inertial frame of reference, when we transform these laws into a rotating frame, some additional centrifugal accelerations appear. The effect of these accelerations is called as "Coriolis effect."

Let the frame A_2 is rotated with respect to a non-accelerating (fixed) frame A_1, with angular velocity $\vec{w}_{A_1/A_2}$. If we define a vector $\vec{V}$ rotating in the frame A_2, we need to add Coriolis accelerations to Newton's second law. In other words, the derivative of

$\vec{V}$ in frame A_1 is equal to the sum of its derivative in frame A_2 and its cross product with the angular velocity, $\vec{w}_{A_1/A_2}$;

$$\frac{d\vec{V}}{dt}\Big|_{A_1} = \frac{d\vec{V}}{dt}\Big|_{A_2} + (\vec{\omega}_{A_1/A_2} \times \vec{V}). \tag{3.10}$$

Therefore, the equations of angular motion are expressed in the body frame by using the angular momentum, $H = J\omega$, as follows;

$$\begin{aligned} \tau_{ext} = \frac{d\vec{H}}{dt}\Big|_E &= \frac{d\vec{H}}{dt}\Big|_B + (\vec{\omega} \times \vec{H}), \\ &= \frac{J\vec{\omega}}{dt}\Big|_B + (\vec{\omega} \times \vec{H}), \end{aligned} \tag{3.11}$$

where $\omega \triangleq \begin{bmatrix} p & q & r \end{bmatrix}^T$, $\tau_{ext} \triangleq \begin{bmatrix} \tau_x & \tau_y & \tau_z \end{bmatrix}^T$.

Therefore, by using (3.11) we get the derivate of the angular rates of the quadrotor body with respect to the body frame;

$$\begin{aligned} \begin{bmatrix} \tau_x \\ \tau_y \\ \tau_z \end{bmatrix} &= \begin{bmatrix} J_{xx} & 0 & 0 \\ 0 & J_{yy} & 0 \\ 0 & 0 & J_{zz} \end{bmatrix} \begin{bmatrix} \dot{p} \\ \dot{q} \\ \dot{r} \end{bmatrix} + \begin{bmatrix} p \\ q \\ r \end{bmatrix} \times \begin{bmatrix} J_{xx} & 0 & 0 \\ 0 & J_{yy} & 0 \\ 0 & 0 & J_{zz} \end{bmatrix} \begin{bmatrix} p \\ q \\ r \end{bmatrix}, \\ \begin{bmatrix} \dot{p} \\ \dot{q} \\ \dot{r} \end{bmatrix} &= \begin{bmatrix} \tau_x/J_{xx} \\ \tau_y/J_{yy} \\ \tau_z/J_{zz} \end{bmatrix} + \begin{bmatrix} qr(J_{yy} - J_{zz})/J_{xx} \\ pr(J_{zz} - J_{xx})/J_{yy} \\ pq(J_{xx} - J_{yy})/J_{zz} \end{bmatrix}. \end{aligned} \tag{3.12}$$

3.1.4 External Forces

Propellers generate thrust force and torque that produce motion for the body. The conventional quadrotor has four propellers with plus $(+)$ or cross (x) configuration as illustrated in Fig. 3.3. This work uses the cross (x) configuration to derive dynamical equations.

Let us start by expressing the thrust force of the quadrotor. The value of the thrust force is used for the altitude change of the body with respect to the earth frame. The thrust value of each propeller is calculated using rotor radius R, air density ρ, the

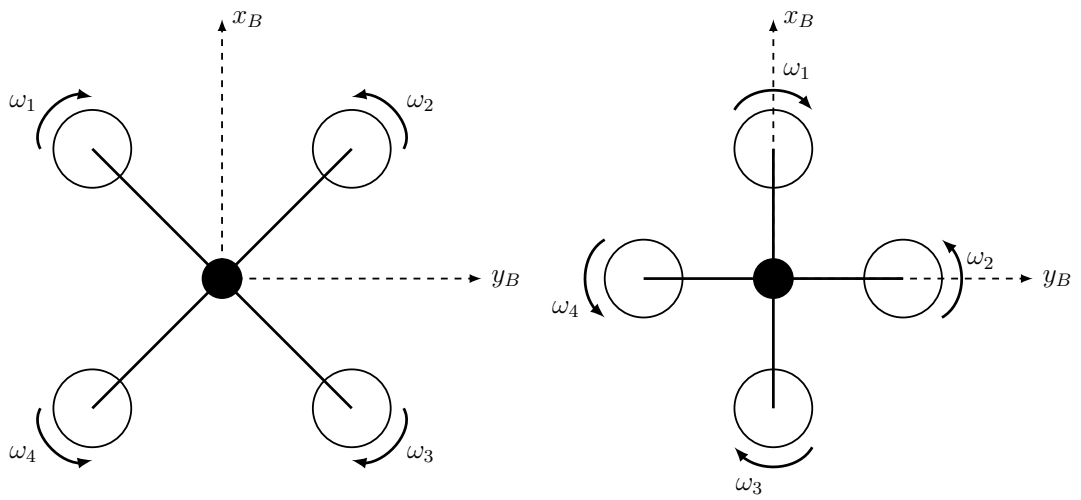

Figure 3.3: Two common structures for conventional quadrotors: Cross and plus configuration.

square of the rotor speed ω, and thrust coefficient c_T. The equation of the thrust force generated for each propeller is expressed as follows;

$$T_p = c_T \rho R^4 \pi \omega^2. \tag{3.13}$$

Although the thrust coefficient changes in time depending on the rotor speed, we consider it a constant parameter for simplicity. So, we can calculate external force, U_1, acting on the quadrotor in the body frame using the thrust forces generated by each propeller;

$$U_1 = \sum_{i=1}^{4} T_p^i = K_T(\omega_1^2 + \omega_2^2 + \omega_3^2 + \omega_4^2), \tag{3.14}$$

where $K_T = c_T \rho \pi R^4$, and T_p^i represents the thrust force of the i^{th} propeller.

However, we need to define the linear equations of motion in the earth frame. The calculated thrust force in the body frame is transformed into the earth frame using the rotation matrix described in (3.3) as follows;

$$\vec{U}_1^E = C_B^E \vec{U}_1^B = \begin{bmatrix} \mathbf{c}_\theta \mathbf{c}_\psi & \mathbf{s}_\phi \mathbf{s}_\theta \mathbf{c}_\psi - \mathbf{c}_\phi \mathbf{s}_\psi & \mathbf{c}_\phi \mathbf{s}_\theta \mathbf{c}_\psi + \mathbf{s}_\phi \mathbf{s}_\psi \\ \mathbf{c}_\theta \mathbf{s}_\psi & \mathbf{s}_\phi \mathbf{s}_\theta \mathbf{s}_\psi + \mathbf{c}_\phi \mathbf{c}_\psi & \mathbf{c}_\phi \mathbf{s}_\theta \mathbf{s}_\psi - \mathbf{s}_\phi \mathbf{c}_\psi \\ -\mathbf{s}_\theta & \mathbf{s}_\phi \mathbf{c}_\theta & \mathbf{c}_\phi \mathbf{c}_\theta \end{bmatrix} \begin{bmatrix} 0 \\ 0 \\ -U_1 \end{bmatrix} = \begin{bmatrix} -(\mathbf{c}_\phi \mathbf{s}_\theta \mathbf{c}_\psi + \mathbf{s}_\phi \mathbf{s}_\psi) U_1 \\ -(\mathbf{c}_\phi \mathbf{s}_\theta \mathbf{s}_\psi - \mathbf{s}_\phi \mathbf{c}_\psi) U_1 \\ -(\mathbf{c}_\phi \mathbf{c}_\theta) U_1 \end{bmatrix}. \tag{3.15}$$

Another external force is generated by gravitational acceleration. This force acts on the quadrotor along the positive z-axis in the earth frame. We can transform it into the body frame by using the DCM from the earth frame to the body frame below;

$$\vec{G}^B = C_E^B \vec{G}^E = C_E^B \begin{bmatrix} 0 \\ 0 \\ Mg \end{bmatrix} = \begin{bmatrix} -Mg\mathbf{s}_\theta \\ Mg\mathbf{c}_\theta\mathbf{s}_\phi \\ Mg\mathbf{c}_\theta\mathbf{c}_\phi \end{bmatrix}. \tag{3.16}$$

3.1.5 External Moments

Rotational motions of the quadrotor, roll-pitch-yaw, are primarily due to a moment produced by the speed change of the four propellers. Since the cross (x) configuration is used in this study, there are 45° between the body frame axes and the quadrotor arms. Thus, the moment arm is calculated accordingly, which is $\frac{1}{\sqrt{2}}$ times the arm length.

Roll angle can be changed by decreasing propeller speed of the propeller P_2 and P_3, while increasing the P_1 and P_4. Then, the difference creates moments around the x axis. By using the moment arm and the difference of the thrust forces, roll moment U_2 is calculated as follows;

$$U_2 = K_T \frac{d}{\sqrt{2}}(\omega_1^2 - \omega_2^2 - \omega_3^2 + \omega_4^2). \tag{3.17}$$

If the speed of P_3 and P_4 decrease while P_1 and P_2 increase, the pitch moment, U_3, occurs and it is computed as;

$$U_3 = K_T \frac{d}{\sqrt{2}}(\omega_1^2 + \omega_2^2 - \omega_3^2 - \omega_4^2). \tag{3.18}$$

Yaw moment is created by drag acting on the propellers' rotor, and it changes depending on the speed and direction of the propellers. Drag moment depends on several parameters as the propeller thrust values do. Again, for simplicity, we take these parameters as a combined constant variable and calculate the yaw moment as below;

$$U_4 = \sum_{i=1}^{4} K_d(\omega_1^2 - \omega_2^2 + \omega_3^2 - \omega_4^2). \tag{3.19}$$

The last generated moment is called gyroscopic torque, which occurs due to rotor rotation. It is calculated with respect to the propeller reference frame P as follows;

$$\vec{\tau}_{g_i}^{P} = J_r \begin{bmatrix} p_i \\ q_i \\ 0 \end{bmatrix} \times \begin{bmatrix} 0 \\ 0 \\ \omega_i \end{bmatrix}, \tag{3.20}$$

where J_r is the moment of inertia of the propeller rotor. Then, the produced moment of the four propellers is expressed in the body frame as follows;

$$\vec{\tau}_{g}^{B} = \begin{bmatrix} \frac{qU_R J_r}{J_{xx}} \\ -\frac{pU_R J_r}{J_{yy}} \\ 0 \end{bmatrix}, \tag{3.21}$$

with the relative rotor speed, $U_R = \omega_1 - \omega_2 + \omega_3 - \omega_4$.

3.1.6 6-DOF Equations of Motion

After expressing the external forces and torques, we are ready to combine the 6-DOF equation of motions of the conventional quadrotor as follows;

$$f(x,u) = \begin{bmatrix} \dot{x} \\ \dot{y} \\ \dot{z} \\ \dot{\phi} \\ \dot{\theta} \\ \dot{\psi} \\ \dot{V}_x \\ \dot{V}_y \\ \dot{V}_z \\ \dot{p} \\ \dot{q} \\ \dot{r} \end{bmatrix} = \begin{bmatrix} V_x \\ V_y \\ V_z \\ p + q\mathbf{s}_\phi \mathbf{t}_\theta + r\mathbf{c}_\phi \mathbf{t}_\theta \\ q\mathbf{c}_\phi - r\mathbf{s}_\phi \\ q\frac{\mathbf{s}_\phi}{\mathbf{c}_\theta} + r\frac{\mathbf{c}_\phi}{\mathbf{c}_\theta} \\ \frac{-(\mathbf{c}_\phi \mathbf{s}_\theta \mathbf{c}_\psi + \mathbf{s}_\phi \mathbf{s}_\psi)U_1}{M} \\ \frac{-(\mathbf{c}_\phi \mathbf{s}_\theta \mathbf{s}_\psi - \mathbf{s}_\phi \mathbf{c}_\psi)U_1}{M} \\ \frac{-(\mathbf{c}_\phi \mathbf{c}_\theta)U_1}{M} + g \\ \frac{U_2 + qU_R J_r + (J_{yy} - J_{zz})qr}{J_{xx}} \\ \frac{U_3 - pU_R J_r + (J_{zz} - J_{xx})pr}{J_{yy}} \\ \frac{U_4 + (J_{xx} - J_{yy})pq}{J_{zz}} \end{bmatrix}. \tag{3.22}$$

3.1.7 2-DOF Abdomen-Like Appendage

The reason behind the idea that we use a 2-DOF pendulum to model an abdomen-like appendage is that the dynamics of a pendulum are well suited to introduce the nonlinear dynamics of the abdomen-like appendage. It is a straightforward mechanical illustration of a nonuniform oscillator [38].

Therefore, let us consider the abdomen-like appendage as a 2-DOF pendulum mounted below the body's center. The abdomen-like appendage has a reference frame, A, whose axes coincide with the inertial frame axes. Let the angle ϕ_a represent the rotation angle around x_A, and θ_a denotes the rotation angle around y_A. These angles determine the motion of the abdomen-like appendage since it has two degrees of freedom.

According to the assumption that the abdomen-like appendage is considered a point mass, the position vector of the appendage at the equilibrium point is expressed in the appendage frame as follows;

$$P_{Ap}^{A} = \begin{bmatrix} 0 & 0 & \ell \end{bmatrix}^{T}, \tag{3.23}$$

where ℓ is the appendage length from the appendage center of mass to the origin of the body frame. When the quadrotor moves, the position of the appendage $P_{Ap}^{E} = [x_p, y_p, z_p]$ in the earth frame can be calculated with the position vector of the quadrotor body, P_{Q}^{E}, as follows;

$$P_{Ap}^{E} = P_{Q}^{E} + C_{A}^{E} P_{Ap}^{A}. \tag{3.24}$$

The matrix C_A^E is calculated by using the rotation matrices $Rot(\theta_a, y_A)$ and $Rot(\phi_a, x_A)$ with the equation below;

$$\begin{aligned} C_{A}^{E} &= Rot(\theta_a, y_A) Rot(\phi_a, x_A), \\ &= \begin{bmatrix} \mathbf{c}_{\theta_a} & 0 & \mathbf{s}_{\theta_a} \\ 0 & 1 & 0 \\ -\mathbf{s}_{\theta_a} & 0 & \mathbf{c}_{\theta_a} \end{bmatrix} \begin{bmatrix} 1 & 0 & 0 \\ 0 & \mathbf{c}_{\phi_a} & -\mathbf{s}_{\phi_a} \\ 0 & \mathbf{s}_{\phi_a} & \mathbf{c}_{\phi_a} \end{bmatrix} = \begin{bmatrix} \mathbf{c}_{\theta_a} & \mathbf{s}_{\theta_a}\mathbf{s}_{\phi_a} & \mathbf{s}_{\theta_a}\mathbf{c}_{\phi_a} \\ 0 & \mathbf{c}_{\phi_a} & -\mathbf{s}_{\phi_a} \\ -\mathbf{s}_{\theta_a} & \mathbf{s}_{\phi_a}\mathbf{c}_{\theta_a} & \mathbf{c}_{\theta_a}\mathbf{c}_{\phi_a} \end{bmatrix}. \end{aligned} \tag{3.25}$$

By combining (3.24) and (3.25), the position of the appendage with respect to the earth frame can be expressed as;

$$P_{Ap}^{E} = \begin{bmatrix} x_{Ap} \\ y_{Ap} \\ z_{Ap} \end{bmatrix} = \begin{bmatrix} x \\ y \\ z \end{bmatrix} + \begin{bmatrix} \mathbf{s}_{\theta_a}\mathbf{c}_{\phi_a}\ell \\ -\mathbf{s}_{\phi_a}\ell \\ \mathbf{c}_{\theta_a}\mathbf{c}_{\phi_a}\ell \end{bmatrix} = \begin{bmatrix} x + \mathbf{s}_{\theta_a}\mathbf{c}_{\phi_a}\ell \\ y - \mathbf{s}_{\phi_a}\ell \\ z + \mathbf{c}_{\theta_a}\mathbf{c}_{\phi_a}\ell \end{bmatrix}. \tag{3.26}$$

The first derivative of the position vector is as follows;

$$\dot{P}_{Ap}^{E} = \begin{bmatrix} \dot{x}_{Ap} \\ \dot{y}_{Ap} \\ \dot{z}_{Ap} \end{bmatrix} = \begin{bmatrix} \dot{x} + \ell(\dot{\theta}_a\mathbf{c}_{\theta_a}\mathbf{c}_{\phi_a} - \dot{\phi}_a\mathbf{s}_{\theta_a}\mathbf{s}_{\phi_a}) \\ \dot{y} - \ell\dot{\phi}_a\mathbf{c}_{\phi_a} \\ \dot{z} - \ell(\dot{\theta}_a\mathbf{s}_{\theta_a}\mathbf{c}_{\phi_a} + \dot{\phi}_a\mathbf{c}_{\theta_a}\mathbf{s}_{\phi_a}) \end{bmatrix}, \tag{3.27}$$

and the second derivative is obtained below;

$$\ddot{P}_{Ap}^{E} = \begin{bmatrix} \ddot{x}_{Ap} \\ \ddot{y}_{Ap} \\ \ddot{z}_{Ap} \end{bmatrix} = \begin{bmatrix} \dot{x} + \ell(\ddot{\theta}_a\mathbf{c}_{\theta_a}\mathbf{c}_{\phi_a} - \dot{\theta}_a^2\mathbf{s}_{\theta_a}\mathbf{c}_{\phi_a} - 2\dot{\theta}_a\dot{\phi}_a\mathbf{c}_{\theta_a}\mathbf{s}_{\phi_a} - \ddot{\phi}_a\mathbf{s}_{\theta_a}\mathbf{s}_{\phi_a} - \dot{\phi}_a^2\mathbf{s}_{\theta_a}\mathbf{c}_{\phi_a}) \\ \ddot{y} - \ell(\ddot{\phi}_a\mathbf{c}_{\phi_a} - \dot{\phi}_a^2\mathbf{s}_{\phi_a}) \\ \ddot{z} - \ell(\ddot{\theta}_a\mathbf{s}_{\theta_a}\mathbf{c}_{\phi_a} + \dot{\theta}_a^2\mathbf{c}_{\theta_a}\mathbf{c}_{\phi_a} - 2\dot{\theta}_a\dot{\phi}_a\mathbf{s}_{\theta_a}\mathbf{s}_{\phi_a} + \ddot{\phi}_a\mathbf{c}_{\theta_a}\mathbf{s}_{\phi_a} + \dot{\phi}_a^2\mathbf{c}_{\theta_a}\mathbf{c}_{\phi_a}) \end{bmatrix}. \tag{3.28}$$

The force vector acting on the appendage in the earth frame is calculated using the DCM from the appendage frame to the earth frame as follows;

$$\begin{bmatrix} f_x \\ f_y \\ f_z \end{bmatrix} = C_A^E \begin{bmatrix} 0 \\ 0 \\ -f \end{bmatrix} = \begin{bmatrix} -f\mathbf{s}_{\theta_a}\mathbf{c}_{\phi_a} \\ f\mathbf{s}_{\phi_a} \\ -f\mathbf{c}_{\theta_a}\mathbf{c}_{\phi_a} \end{bmatrix}, \tag{3.29}$$

where f is the tension force in the appendage frame. According to Newton's second law, the following equations can be obtained with the appendage mass m;

$$\begin{aligned} f_x &= m\ddot{x}_{Ap} = -f\mathbf{s}_{\theta_a}\mathbf{c}_{\phi_a}, \\ f_y &= m\ddot{y}_{Ap} = f\mathbf{s}_{\phi_a}, \\ f_z &= m\ddot{z}_{Ap} = -f\mathbf{c}_{\theta_a}\mathbf{c}_{\phi_a}. \end{aligned} \tag{3.30}$$

From these three equations stated above, we obtain;

$$m(\mathbf{c}_{\theta_a}\ddot{x}_{Ap} - \mathbf{s}_{\theta_a}\ddot{z}_{Ap}) = -mg\mathbf{s}_{\theta_a}, \tag{3.31}$$

and by rewriting (3.31), we get

$$-g\mathbf{s}_{\theta_a} = \ddot{x}\mathbf{c}_{\theta_a} - \ddot{z}\mathbf{s}_{\theta_a} + \ell\ddot{\theta}_a\mathbf{c}_{\phi_a} - 2\ell\dot{\theta}_a\dot{\phi}_a\mathbf{s}_{\phi_a}. \tag{3.32}$$

Then, by adding the external torque to (3.32), we get

$$\ddot{\theta}_a = \frac{1}{\ell \mathbf{c}_{\phi_a}}(-g\mathbf{s}_{\theta_a} - \ddot{x}\mathbf{c}_{\theta_a} + \ddot{z}\mathbf{s}_{\theta_a} + 2\ell\dot{\theta}_a\dot{\phi}_a\mathbf{s}_{\phi_a}) + \frac{\tau_{ay}}{I_{py}}. \tag{3.33}$$

For ϕ_a, we obtain the following equation;

$$m(\mathbf{c}_{\theta_a}\mathbf{c}_{\phi_a}\ddot{y}_{Ap} + \mathbf{s}_{\phi_a}\ddot{z}_{Ap}) = mg\mathbf{s}_{\phi_a}, \tag{3.34}$$

and by rewriting (3.34), we get

$$g\mathbf{s}_{\phi_a} = \ddot{y}\mathbf{c}_{\theta_a}\mathbf{c}_{\phi_a} + \ddot{z}\mathbf{s}_{\phi_a}\ell(\ddot{\theta}_a\mathbf{s}_{\theta_a}\mathbf{s}_{\phi_a}\mathbf{c}_{\phi_a} + \dot{\theta}_a^2\mathbf{c}_{\theta_a}\mathbf{s}_{\phi_a}\mathbf{c}_{\phi_a} - 2\dot{\theta}_a\dot{\phi}_a\mathbf{s}_{\theta_a}\mathbf{s}_{\phi_a}^2 + \ddot{\phi}_a\mathbf{c}_{\theta_a}). \tag{3.35}$$

By substituting $\ddot{\theta}_a$ and adding the applied torque into (3.35), we obtain the following equation;

$$\ddot{\phi}_a = -\frac{1}{\ell}(g\mathbf{c}_{\theta_a}\mathbf{s}_{\phi_a} + \ddot{x}\mathbf{s}_{\theta_a}\mathbf{s}_{\phi_a} + \ddot{y}\mathbf{c}_{\phi_a} + \ddot{z}\mathbf{c}_{\theta_a}\mathbf{s}_{\phi_a} - \dot{\theta}_a^2\ell\mathbf{s}_{\phi_a}\mathbf{c}_{\phi_a}) + \frac{\tau_{ax}}{I_{px}}. \tag{3.36}$$

After analyzing the appendage force, we have the nonlinear equations of the quadrotor with an actively controlled 2-DOF abdomen-like appendage as follows;

$$f(x,u) = \begin{bmatrix} \dot{x} & \dot{y} & \dot{z} & \dot{\phi} & \dot{\theta} & \dot{\psi} & \dot{\phi}_a & \dot{\theta}_a & \dot{V}_x & \dot{V}_y & \dot{V}_z & \dot{p} & \dot{q} & \dot{r} & \ddot{\phi}_a & \ddot{\theta}_a \end{bmatrix}^T$$

$$= \begin{bmatrix} V_x \\ V_y \\ V_z \\ p + q\mathbf{s}_\phi\mathbf{t}_\theta + r\mathbf{c}_\phi\mathbf{t}_\theta \\ q\mathbf{c}_\phi - r\mathbf{s}_\phi \\ q\frac{\mathbf{s}_\phi}{\mathbf{c}_\theta} + r\frac{\mathbf{c}_\phi}{\mathbf{c}_\theta} \\ \dot{\phi}_a \\ \dot{\theta}_a \\ \frac{-1}{M+m}[(\mathbf{c}_\phi s_\theta\mathbf{c}_\psi + \mathbf{s}_\phi\mathbf{s}_\psi)U_1 + m\ell(\ddot{\theta}_a\mathbf{c}_{\theta_a}\mathbf{c}_{\phi_a} - \dot{\theta}_a^2\mathbf{s}_{\theta_a}\mathbf{c}_{\phi_a} - 2\dot{\theta}_a\dot{\phi}_a\mathbf{c}_{\theta_a}\mathbf{s}_{\phi_a} - \ddot{\phi}_a\mathbf{s}_{\theta_a}\mathbf{s}_{\phi_a} - \dot{\phi}_a^2\mathbf{s}_{\theta_a}\mathbf{c}_{\phi_a})] \\ \frac{-1}{M+m}[-(\mathbf{c}_\phi\mathbf{s}_\theta\mathbf{s}_\psi - \mathbf{s}_\phi\mathbf{c}_\psi)U_1 + m\ell(\ddot{\phi}_a(\mathbf{c}_{\phi_a} - \dot{\phi}_a^2\mathbf{s}_{\phi_a})] \\ \frac{-1}{M+m}[-(\mathbf{c}_\phi\mathbf{c}_\theta)U_1 + m\ell(\ddot{\theta}_a\mathbf{s}_{\theta_a}\mathbf{c}_{\phi_a} + \dot{\theta}_a^2\mathbf{c}_{\theta_a}\mathbf{c}_{\phi_a} - 2\dot{\theta}_a\dot{\phi}_a\mathbf{s}_{\theta_a}\mathbf{s}_{\phi_a} + \ddot{\phi}_a\mathbf{c}_{\theta_a}\mathbf{s}_{\phi_a} + \dot{\phi}_a^2\mathbf{c}_{\theta_a}\mathbf{c}_{\phi_a})] + g \\ \frac{U_2 + qU_RJ_r + (J_{yy} - J_{zz})qr}{J_{xx}} \\ \frac{U_3 - pU_RJ_r + (J_{zz} - J_{xx})pr}{J_{yy}} \\ \frac{U_4 + (J_{xx} - J_{yy})pq}{J_{zz}} \\ \frac{1}{M\ell}[(-\mathbf{s}_{\theta_a}\mathbf{s}_{\phi_a}(\mathbf{c}_\phi\mathbf{s}_\theta\mathbf{c}_\psi + \mathbf{s}_\phi\mathbf{s}_\psi) - \mathbf{c}_{\phi_a}(\mathbf{c}_\phi\mathbf{s}_\theta\mathbf{s}_\psi) - \mathbf{c}_{\theta_a}\mathbf{s}_{\phi_a}\mathbf{c}_\phi\mathbf{c}_\theta)U_1] - \mathbf{s}_{\phi_a}\mathbf{c}_{\phi_a}\dot{\theta}_a^2 + \frac{(M+m)\tau_{ax}}{MI_{px}} \\ \frac{1}{M}[2M\dot{\theta}_a\dot{\phi}_a\mathbf{t}_{\phi_a} + (\frac{\mathbf{c}_{\theta_a}}{L\mathbf{c}_{\phi_a}}(\mathbf{c}_\phi\mathbf{s}_\theta\mathbf{c}_\psi + \mathbf{s}_\phi s_\psi) - \frac{\mathbf{s}_{\theta_a}}{L\mathbf{c}_{\phi_a}}(\mathbf{c}_\phi\mathbf{c}_\theta))U_1] + \frac{(M+m)\tau_{ay}}{MI_{py}} \end{bmatrix}, \tag{3.37}$$

with the following control input;

$$u = \begin{bmatrix} U_1 & U_2 & U_3 & U_4 & \tau_{ax} & \tau_{ay} \end{bmatrix}^T. \tag{3.38}$$

3.2 Linearization

Conventional quadrotors have multiple equilibrium points. Since nonlinear dynamics complicate the system equations and make controller design a challenging task, system dynamics need to be linearized around some operating points to use linear control theory approaches. The linearization of the quadrotor is performed in the hovering state. During hovering, the states x, y, z, and ψ can have any value and do not change the system dynamics.

Thus, the linearization is performed around the equilibrium point represented by the following states and inputs;

$$\begin{aligned} \boldsymbol{x}_e &= \begin{bmatrix} x_0 & y_0 & z_0 & 0 & 0 & \psi_0 & 0 & 0 & 0 & 0 & 0 & 0 & 0 & 0 & 0 & 0 \end{bmatrix}^T, \\ \boldsymbol{u}_e &= \begin{bmatrix} -(M+m)g & 0 & 0 & 0 & 0 & 0 \end{bmatrix}^T. \end{aligned} \tag{3.39}$$

At the equilibrium point, we have

$$\dot{x} = f(x_e, u_e) = 0. \tag{3.40}$$

The equation for the linearization of the nonlinear function $f(x, u)$ at equilibrium point (x_e, u_e) is;

$$f(x,u) \approx f(x_e, u_e) + \left.\frac{\partial f(x,u)}{\partial x}\right|_{x_e,u_e} (x - x_e) + \left.\frac{\partial f(x,u)}{\partial u}\right|_{x_e,u_e} (u - u_e). \tag{3.41}$$

Since $f(x_e, u_e) = 0$, the linearized state space equation of the system is as follows;

$$\dot{\bar{x}} = A\bar{x} + B\bar{u}, \tag{3.42}$$

where

$$\begin{aligned} A &= \left.\frac{\partial f(x,u)}{\partial x}\right|_{x_e,u_e}, \quad B = \left.\frac{\partial f(x,u)}{\partial u}\right|_{x_e,u_e}, \\ \bar{x} &= x - x_e, \qquad\qquad \bar{u} = u - u_e. \end{aligned} \tag{3.43}$$

Therefore, A and B matrices are as follows;

$$A = \left[\begin{array}{cccccccc|c} \multicolumn{8}{c|}{\mathbf{0}_{8x8}} & \mathbf{I}_{8x8} \\ \hline 0 & 0 & 0 & 0 & -\frac{(M+m)}{M}g & 0 & 0 & \frac{m}{M}g & \\ 0 & 0 & 0 & \frac{(M+m)}{M}g & 0 & 0 & -\frac{m}{M}g & 0 & \\ 0 & 0 & 0 & 0 & 0 & 0 & 0 & 0 & \\ 0 & 0 & 0 & 0 & 0 & 0 & 0 & 0 & \mathbf{0}_{8x8} \\ 0 & 0 & 0 & 0 & 0 & 0 & 0 & 0 & \\ 0 & 0 & 0 & 0 & 0 & 0 & 0 & 0 & \\ 0 & 0 & 0 & \frac{(M+m)}{M}g & 0 & 0 & -\frac{(M+m)}{ML}g & 0 & \\ 0 & 0 & 0 & 0 & \frac{(M+m)}{M}g & 0 & 0 & -\frac{(M+m)}{ML}g & \end{array}\right], \quad (3.44)$$

$$B = \left[\begin{array}{cccccc} \multicolumn{6}{c}{\mathbf{0}_{8x6}} \\ \hline 0 & 0 & 0 & 0 & 0 & -\frac{mL}{MI_{py}} \\ 0 & 0 & 0 & 0 & \frac{mL}{MI_{px}} & 0 \\ -\frac{1}{M+m} & 0 & 0 & 0 & 0 & 0 \\ 0 & \frac{1}{J_{xx}} & 0 & 0 & 0 & 0 \\ 0 & 0 & \frac{1}{J_{yy}} & 0 & 0 & 0 \\ 0 & 0 & 0 & \frac{1}{J_{zz}} & 0 & 0 \\ 0 & 0 & 0 & 0 & \frac{(M+m)}{MI_{px}} & 0 \\ 0 & 0 & 0 & 0 & 0 & \frac{(M+m)}{MI_{py}} \end{array}\right]. \quad (3.45)$$

CHAPTER 4

CONTROLLER DESIGN

Practically, in a control problem, the controller aims to calculate the input to the plant such that the tracking performance and stabilization are successfully guaranteed. Therefore, we design optimization-based controllers; linear quadratic regulator (LQR), model predictive controller (MPC), and adaptive model predictive control (A-MPC) to analyze the performance of the proposed aerial vehicle structure with an actively controlled abdomen-like appendage. In this section, we provide backgrounds for these controllers. First, we represent the state space models of the nonlinear systems derived in Chapter 2 and Chapter 3. Then, we explain the scaling method that makes the selection of the weighting parameters easy for optimization-based controllers. Finally, we give a brief introduction to each controller approach.

4.1 State-Space Model

In predictive control design, Wang [39] states three main approaches: Finite impulse response (FIR), transfer function, and state space models. The earlier method combines finite impulse response (FIR) and step response models. However, this method is limited to stable plant dynamics. Then, the transfer function model is introduced, and it is used for both stable and unstable plant dynamics. This approach is more effective than the earlier one but has a drawback; it is not well suited for the MIMO systems. Finally, the state space formulation, appropriate for MIMO systems, has been presented by Ordys and Clarke [40] for predictive control design. Recently, state space design methods have been widely used in predictive control design [41]. Therefore, in this study, we used the state space model of the proposed systems to

design predictive-based controllers.

Table 4.1: Model parameter values

Parameter	Symbol	Value
Body height of the bi-rotor platform (m)	h	0.3
Body length of the bi-rotor platform (m)	L	0.5
Drag coefficient (Ns^2)	K_d	3.02×10^{-7}
Length of the abdomen-like appendage(m)	ℓ	0.15
Length of the quadrotor arm (m)	d	0.3
Mass of the body (kg)	M	1.5
Mass of the abdomen (kg)	m	0.75
Maximum rotor speed (rad/s)	ω_{max}	950
Moments of inertia of the bi-rotor platform ($kg.m^2$)	I_M	0.0425
Moments of inertia of the quadrotor along the x-axis ($kg.m^2$)	J_{xx}	0.0143
Moments of inertia of the quadrotor along the y-axis ($kg.m^2$)	J_{yy}	0.0143
Moments of inertia of the quadrotor along the z-axis ($kg.m^2$)	J_{zz}	0.0276
Rotor inertia ($kg.m^2$)	J_r	9.89×10^{-5}
Thrust coefficient (Ns^2)	K_T	2.83×10^{-5}

In Chapter 2 and Chapter 3, we represented the equations of motion of the aerial vehicles parametrically in planar and 3D space. Now, we obtain the state space models of the systems using the parameter values depicted in Table 4.1.

The inspired insect hawkmoth *Manduca sexta* has an abdomen weight of approximately half of the mass of the animal [9]. Demir et al. [11] used a servo-actuated battery as an appendage, weighing about one-third of the total quadrotor mass in their experiment. Considering these studies, we chose appendage weight as half of the

vehicle body weight. We select other parameters, such as moments of inertia values, thrust and drag coefficients, rotor inertia, and arm length, as consistent with the manufactured conventional quadrotors. We select the appendage length as 0.15 m, meaning that the appendage lowers the CoG by 0.2 m at a naturally dropped position.

We derive the discrete-time state-space equations with the parameters in Table 4.1. The discrete-time linear models of the systems have the following form;

$$x(k+1) = \mathbf{A}x(k) + \mathbf{B}u(k). \tag{4.1}$$

We transform the continuous state space models to the discrete state space models using the *zero-order hold* (ZOH) discretization method. For all four systems derived before, we assume that all states of the systems are available, meaning that the systems are completely observable. We discretize the continuous state space models with a sampling period $T_s = 0.05$ s.

4.1.1 Conventional Bi-rotor Platform

The discrete state space model of the conventional bi-rotor platform is as follows;

$$\begin{bmatrix} \dot{x} \\ \dot{z} \\ \dot{\theta}_1 \\ \ddot{x} \\ \ddot{z} \\ \ddot{\theta}_1 \end{bmatrix} = \underbrace{\begin{bmatrix} 1 & 0 & -0.01226 & 0.05 & 0 & -0.0002 \\ 0 & 1 & 0 & 0 & 0.05 & 0 \\ 0 & 0 & 1 & 0 & 0 & 0.05 \\ 0 & 0 & -0.4905 & 1 & 0 & -0.01226 \\ 0 & 0 & 0 & 0 & 1 & 0 \\ 0 & 0 & 0 & 0 & 0 & 1 \end{bmatrix}}_{A} \begin{bmatrix} x \\ z \\ \theta_1 \\ \dot{x} \\ \dot{z} \\ \dot{\theta}_1 \end{bmatrix} + \underbrace{\begin{bmatrix} 0.00001 & -0.00001 \\ 0.0005556 & 0.0005556 \\ -0.004902 & 0.004902 \\ 0.0008015 & -0.000802 \\ 0.02222 & 0.02222 \\ -0.1961 & 0.1961 \end{bmatrix}}_{B} \begin{bmatrix} F_1 \\ F_2 \end{bmatrix}, \tag{4.2}$$

and the input-output constraints are listed below;

$$Cx_{min} \leq x \leq Cx_{max}, \tag{4.3a}$$

$$Cy_{min} \leq y \leq Cy_{umax}, \tag{4.3b}$$

$$-\frac{\pi}{3} \leq \theta_1 \leq \frac{\pi}{3}, \tag{4.3c}$$

$$F_{1_{min}} \leq F_1 \leq F_{1_{max}}, \tag{4.3d}$$

$$F_{2_{min}} \leq F_2 \leq F_{2_{max}}, \tag{4.3e}$$

where the input values F_1 and F_2 are in the interval of $[F_{1_{min}}, F_{1_{max}}]$ and $[F_{2_{min}}, F_{2_{max}}]$, respectively. The position constraints $Cx_{min}, Cx_{max}, Cz_{min}, Cz_{umax}$ can be changed

in real-time. The body angle θ_1 is limited to avoid singularity and produce proper control inputs.

4.1.2 Bi-rotor Platform with an Actively Controlled Abdomen-like Appendage

The discrete state space model of the proposed bi-rotor platform with an actively controlled abdomen-like appendage is as follows;

$$\begin{bmatrix} \dot{x} \\ \dot{z} \\ \dot{\theta}_1 \\ \dot{\theta}_2 \\ \ddot{x} \\ \ddot{z} \\ \ddot{\theta}_1 \\ \ddot{\theta}_2 \end{bmatrix} = \underbrace{\begin{bmatrix} 1 & 0 & -0.01814 & 0.005876 & 0.05 & 0 & -0.000304 & 0.00001 \\ 0 & 1 & 0 & 0 & 0 & 0.05 & 0 & 0 \\ 0 & 0 & 0.9685 & 0.03146 & 0 & 0 & 0.04947 & 0.0005309 \\ 0 & 0 & 0.1503 & 0.8497 & 0 & 0 & 0.002537 & 0.04746 \\ 0 & 0 & -0.7155 & 0.225 & 1 & 0 & -0.01814 & 0.005879 \\ 0 & 0 & 0 & 0 & 0 & 1 & 0 & 0 \\ 0 & 0 & -1.219 & 1.219 & 0 & 0 & 0.9685 & 0.03146 \\ 0 & 0 & 5.823 & -5.823 & 0 & 0 & 0.1503 & 0.8497 \end{bmatrix}}_{A} \begin{bmatrix} x \\ z \\ \theta_1 \\ \theta_2 \\ \dot{x} \\ \dot{z} \\ \dot{\theta}_1 \\ \dot{\theta}_2 \end{bmatrix}$$

$$+ \underbrace{\begin{bmatrix} 0.00003 & -0.00003 & -0.005325 \\ 0.0005556 & 0.0005556 & 0 \\ -0.007274 & 0.007274 & -0.0285 \\ 0.006978 & -0.006978 & 0.1362 \\ 0.002374 & -0.002374 & -0.2039 \\ 0.02222 & 0.02222 & 0 \\ -0.2879 & 0.2879 & -1.104 \\ 0.2643 & -0.2643 & 5.276 \end{bmatrix}}_{B} \begin{bmatrix} F_1 \\ F_2 \\ \tau \end{bmatrix}, \tag{4.4}$$

with the following input-output constraints;

$$Cx_{min} \leq x \leq Cx_{max}, \tag{4.5a}$$

$$Cy_{min} \leq y \leq Cy_{max}, \tag{4.5b}$$

$$-\frac{\pi}{3} \leq \theta_1 \leq \frac{\pi}{3}, \tag{4.5c}$$

$$\frac{\pi}{6} \leq \theta_2 \leq \frac{5\pi}{6}, \tag{4.5d}$$

$$F_{1_{min}} \leq F_1 \leq F_{1_{max}}, \tag{4.5e}$$

$$F_{2_{min}} \leq F_2 \leq F_{2_{max}}, \tag{4.5f}$$

$$\tau_{min} \leq \tau \leq \tau_{max}, \tag{4.5g}$$

$$\dot{\tau}_{min} \leq \dot{\tau} \leq \dot{\tau}_{max}. \tag{4.5h}$$

The appendage can rotate in the interval $(\frac{\pi}{6}, \frac{5\pi}{6})$, and this is the soft constraint of the joint. As Dyhr et al. [10] state, moths change the abdominal joint angle along with the highly actuated muscles; we must limit the applied torque to fairly compare the animals with physical systems. Therefore, the model includes the torque limits and constraint of the applied torque rate of change, $\dot{\tau}$, to represent the joint as a physical actuator.

4.1.3 Conventional Quadrotor Platform

We continue with the quadrotor models in 3D space for the next step. The conventional quadrotor platform has the following discrete state space model;

$$\begin{bmatrix} \dot{x} \\ \dot{y} \\ \dot{z} \\ \dot{\phi} \\ \dot{\theta} \\ \dot{\psi} \\ \dot{V}_x \\ \dot{V}_y \\ \dot{V}_z \\ \dot{p} \\ \dot{q} \\ \dot{r} \end{bmatrix} = \underbrace{\begin{bmatrix} 1 & 0 & 0 & 0 & -0.01226 & 0 & 0.05 & 0 & 0 & 0 & -0.0002044 & 0 \\ 0 & 1 & 0 & 0.01226 & 0 & 0 & 0 & 0.05 & 0 & 0.0002044 & 0 & 0 \\ 0 & 0 & 1 & 0 & 0 & 0 & 0 & 0 & 0.05 & 0 & 0 & 0 \\ 0 & 0 & 0 & 1 & 0 & 0 & 0 & 0 & 0 & 0.05 & 0 & 0 \\ 0 & 0 & 0 & 0 & 1 & 0 & 0 & 0 & 0 & 0 & 0.05 & 0 \\ 0 & 0 & 0 & 0 & 0 & 1 & 0 & 0 & 0 & 0 & 0 & 0.05 \\ 0 & 0 & 0 & 0 & -0.4905 & 0 & 1 & 0 & 0 & 0 & -0.01226 & 0 \\ 0 & 0 & 0 & 0.4905 & 0 & 0 & 0 & 1 & 0 & 0.01226 & 0 & 0 \\ 0 & 0 & 0 & 0 & 0 & 0 & 0 & 0 & 1 & 0 & 0 & 0 \\ 0 & 0 & 0 & 0 & 0 & 0 & 0 & 0 & 0 & 1 & 0 & 0 \\ 0 & 0 & 0 & 0 & 0 & 0 & 0 & 0 & 0 & 0 & 1 & 0 \\ 0 & 0 & 0 & 0 & 0 & 0 & 0 & 0 & 0 & 0 & 0 & 1 \end{bmatrix}}_{A} \begin{bmatrix} x \\ y \\ z \\ \phi \\ \theta \\ \psi \\ V_x \\ V_y \\ V_z \\ p \\ q \\ r \end{bmatrix} \tag{4.6}$$

$$+ \underbrace{\begin{bmatrix} 0 & 0 & -0.0001786 & 0 \\ 0 & 0.0001786 & 0 & 0 \\ -0.0007353 & 0 & 0 & 0 \\ 0 & 0.08741 & 0 & 0 \\ 0 & 0 & 0.08741 & 0 \\ 0 & 0 & 0 & 0.04529 \\ 0 & 0 & -0.01429 & 0 \\ 0 & 0.01429 & 0 & 0 \\ -0.02941 & 0 & 0 & 0 \\ 0 & 3.497 & 0 & 0 \\ 0 & 0 & 3.497 & 0 \\ 0 & 0 & 0 & 1.812 \end{bmatrix}}_{B} \begin{bmatrix} U_1 \\ U_2 \\ U_3 \\ U_4 \end{bmatrix},$$

with the following input-output constraints;

$$U_{1_{min}} \leq U_1 \leq U_{1_{max}}, \tag{4.7a}$$
$$U_{2_{min}} \leq U_2 \leq U_{2_{max}}, \tag{4.7b}$$
$$U_{3_{min}} \leq U_3 \leq U_{3_{max}}, \tag{4.7c}$$
$$U_{4_{min}} \leq U_4 \leq U_{4_{max}}, \tag{4.7d}$$
$$-\frac{\pi}{3} \leq \phi \leq \frac{\pi}{3}, \tag{4.7e}$$
$$-\frac{\pi}{3} \leq \theta \leq \frac{\pi}{3}, \tag{4.7f}$$
$$-\frac{\pi}{3} \leq \psi \leq \frac{\pi}{3}, \tag{4.7g}$$

where thrust force U_1, and roll, pitch, and yaw moments U_2, U_3, U_4 have boundaries due to rotor speed limitations. We calculate the maximum thrust and minimum thrust values from the equation (3.14) with the following formula;

$$U_{1_{max}} = 4K_T\omega_{max}^2, \tag{4.8}$$
$$U_{1_{min}} = 0. \tag{4.9}$$

And, the maximum and minimum values of the roll, pitch, and yaw moments, which are derived in equations (3.17,3.18,3.19), are calculated as follows;

$$U_{2_{max}} = 2K_T\frac{d}{\sqrt{2}}\omega_{max}^2, \qquad U_{2_{min}} = -2K_T\frac{d}{\sqrt{2}}\omega_{max}^2, \tag{4.10}$$
$$U_{3_{max}} = 2K_T\frac{d}{\sqrt{2}}\omega_{max}^2, \qquad U_{3_{min}} = -2K_T\frac{d}{\sqrt{2}}\omega_{max}^2, \tag{4.11}$$
$$U_{4_{max}} = 2K_d\omega_{max}^2, \qquad U_{4_{min}} = -2K_d\omega_{max}^2. \tag{4.12}$$

We also put angle constraints as we did for the bi-rotor platforms to avoid singularity and produce proper control inputs.

4.1.4 Quadrotor Platform with an Actively Controlled 2-D0F Abdomen-like Appendage

Lastly, the discretized state-space equation of the proposed quadrotor structure is as follows;

$$
\begin{bmatrix} \dot{x} \\ \dot{y} \\ \dot{z} \\ \dot{\phi} \\ \dot{\theta} \\ \dot{\psi} \\ \dot{\phi}_a \\ \dot{\theta}_a \\ \dot{V}_x \\ \dot{V}_y \\ \dot{V}_z \\ \dot{p} \\ \dot{q} \\ \dot{r} \\ \ddot{\phi}_a \\ \ddot{\theta}_a \end{bmatrix} =
\begin{bmatrix}
1 & 0 & 0 & 0 & -0.0176 & 0 & 0 & 0.00538 & 0.05 & 0 & 0 & 0 & -0.00029 & \dots \\
0 & 1 & 0 & 0.0176 & 0 & 0 & -0.00538 & 0 & 0 & 0.05 & 0 & 0.00029 & 0 & \dots \\
0 & 0 & 1 & 0 & 0 & 0 & 0 & 0 & 0 & 0 & 0.05 & 0 & 0 & \dots \\
0 & 0 & 0 & 1 & 0 & 0 & 0 & 0 & 0 & 0 & 0 & 0.05 & 0 & \dots \\
0 & 0 & 0 & 0 & 1 & 0 & 0 & 0 & 0 & 0 & 0 & 0 & 0.05 & \dots \\
0 & 0 & 0 & 0 & 0 & 1 & 0 & 0 & 0 & 0 & 0 & 0 & 0 & \dots \\
0 & 0 & 0 & 0.0351 & 0 & 0 & 0.965 & 0 & 0 & 0 & 0 & 0.00059 & 0 & \dots \\
0 & 0 & 0 & 0 & 0.0351 & 0 & 0 & 0.965 & 0 & 0 & 0 & 0 & 0.00059 & \dots \\
0 & 0 & 0 & 0 & -0.704 & 0 & 0 & 0.214 & 1 & 0 & 0 & 0 & -0.0176 & \dots \\
0 & 0 & 0 & 0.704 & 0 & 0 & -0.214 & 0 & 0 & 1 & 0 & 0.0176 & 0 & \dots \\
0 & 0 & 0 & 0 & 0 & 0 & 0 & 0 & 0 & 0 & 1 & 0 & 0 & \dots \\
0 & 0 & 0 & 0 & 0 & 0 & 0 & 0 & 0 & 0 & 0 & 1 & 0 & \dots \\
0 & 0 & 0 & 0 & 0 & 0 & 0 & 0 & 0 & 0 & 0 & 0 & 1 & \dots \\
0 & 0 & 0 & 0 & 0 & 0 & 0 & 0 & 0 & 0 & 0 & 0 & 0 & \dots \\
0 & 0 & 0 & 1.397 & 0 & 0 & -1.397 & 0 & 0 & 0 & 0 & 0.0351 & 0 & \dots \\
0 & 0 & 0 & 0 & 1.397 & 0 & 0 & -1.397 & 0 & 0 & 0 & 0 & 0.0351 & \dots
\end{bmatrix}
\begin{bmatrix} x \\ y \\ z \\ \phi \\ \theta \\ \psi \\ \phi_a \\ \theta_a \\ V_x \\ V_y \\ V_z \\ p \\ q \\ r \\ \dot{\phi}_a \\ \dot{\theta}_a \end{bmatrix}
$$

$$
\begin{bmatrix}
\dots & 0 & 0 & 0.000089 \\
\dots & 0 & -0.000089 & 0 \\
\dots & 0 & 0 & 0 \\
\dots & 0 & 0 & 0 \\
\dots & 0 & 0 & 0 \\
\dots & 0.05 & 0 & 0 \\
\dots & 0 & 0.0494 & 0 \\
\dots & 0 & 0 & 0.0494 \\
\dots & 0 & 0 & 0.00538 \\
\dots & 0 & -0.00538 & 0 \\
\dots & 0 & 0 & 0 \\
\dots & 0 & 0 & 0 \\
\dots & 0 & 0 & 0 \\
\dots & 1 & 0 & 0 \\
\dots & 0 & 0.965 & 0 \\
\dots & 0 & 0 & 0.965
\end{bmatrix}
+
\underbrace{\begin{bmatrix}
0 & 0 & -0.00026 & 0 & 0 & -0.0015 \\
0 & 0.00026 & 0 & 0 & 0.0015 & 0 \\
-0.0005 & 0 & 0 & 0 & 0 & 0 \\
0 & 0.0874 & 0 & 0 & 0 & 0 \\
0 & 0 & 0.0874 & 0 & 0 & 0 \\
0 & 0 & 0 & 0.0453 & 0 & 0 \\
0 & 0.00051 & 0 & 0 & 0.0095 & 0 \\
0 & 0 & 0.00051 & 0 & 0 & 0.0095 \\
0 & 0 & -0.0206 & 0 & 0 & -0.058 \\
0 & 0.0206 & 0 & 0 & 0.058 & 0 \\
-0.0204 & 0 & 0 & 0 & 0 & 0 \\
0 & 3.497 & 0 & 0 & 0 & 0 \\
0 & 0 & 3.497 & 0 & 0 & 0 \\
0 & 0 & 0 & 1.812 & 0 & 0 \\
0 & 0.041 & 0 & 0 & 0.379 & 0 \\
0 & 0 & 0.041 & 0 & 0 & 0.379
\end{bmatrix}}_{B}
\begin{bmatrix} U_1 \\ U_2 \\ U_3 \\ U_4 \\ \tau_{ax} \\ \tau_{ay} \end{bmatrix}, \tag{4.13}
$$

with the following input-output constraints;

$$U_{i_{min}} \leq U_i \leq U_{i_{max}}, \qquad i = 1, 2, 3, 4 \tag{4.14a}$$

$$-\frac{\pi}{3} \leq \phi, \theta, \psi, \phi_a, \theta_a \leq \frac{\pi}{3}, \tag{4.14b}$$

$$\tau_{x_{min}} \leq \tau_x \leq \tau_{x_{max}}, \tag{4.14c}$$

$$\dot{\tau}_{x_{min}} \leq \dot{\tau}_x \leq \dot{\tau}_{xmax}, \tag{4.14d}$$

$$\tau_{y_{min}} \leq \tau_y \leq \tau_{y_{max}}, \tag{4.14e}$$

$$\dot{\tau}_{y_{min}} \leq \dot{\tau}_y \leq \dot{\tau}_{ymax}. \tag{4.14f}$$

4.2 Scaling State-Space Model

In practical applications, tuning the weight parameters for the optimization-based controller design becomes easier if we scale the model considering the boundaries of the input-output variables. One of the most used scaling techniques is to make the input-output variables less than one in magnitude [42]. Therefore, we have reference $|r(t)| \leq 1$ and disturbance $|d(t)| \leq 1$, with control input $|u(t)| \leq 1$ such that the error $|e(t)| = |y(t) - r(t)| \leq 1$. To specify scale factors, we need to estimate the span of the input and output variables.

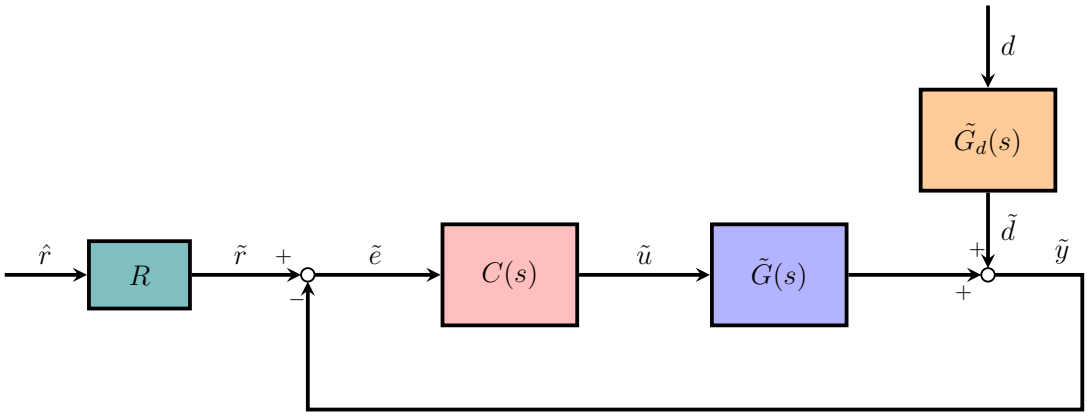

Figure 4.1: Block diagram of the system in terms of scaled variables

Let us denote the original linear model of the MIMO plant $G(s)$ with reference input u and output y. We also represent the disturbance input d and disturbance model $G_d(s)$ in the output equation. The output and error equations are as follows;

$$y = Gu + G_d d, \tag{4.15a}$$

$$e = y - r. \tag{4.15b}$$

Then, we divide each input variable by its maximum value and obtain scaled input variables whose magnitudes are less than equal to one;

$$\tilde{u} = \frac{u}{u_{max}}, \qquad \tilde{d} = \frac{d}{d_{max}}. \tag{4.16}$$

After that, we scale (4.15b) by dividing e_{max} because the primary purpose is to mini-

mize the control error. The new scaled variables $\tilde{y}, \tilde{r}$ and $\tilde{e}$ are as follows;

$$\tilde{y} = \frac{y}{e_{max}}, \qquad \tilde{r} = \frac{r}{e_{max}}, \qquad \tilde{e} = \frac{e}{e_{max}}. \tag{4.17}$$

Since the system we work with is MIMO, we need to introduce the scaling matrices D_d, D_u, D_e, D_r, whose diagonal elements are the maximum value of the corresponding variables. Then, the scaled variables become

$$\tilde{d} = D_d^{-1} d, \qquad \tilde{u} = D_u^{-1} u, \qquad \tilde{y} = D_e^{-1} y, \qquad \tilde{e} = D_e^{-1} e, \qquad \tilde{r} = D_e^{-1} r. \tag{4.18}$$

With the introduced matrices, the new scaled plant and disturbance model are as follows;

$$\tilde{G} = D_e^{-1} G D_u, \qquad \tilde{G_d} = D_e^{-1} G_d D_d. \tag{4.19}$$

To make the reference signal less than 1 in magnitude, we divide the reference signal by the maximum reference signal change value as follows;

$$\hat{r} = \frac{r}{r_{max}} = D_r^{-1} r. \tag{4.20}$$

Then, we have

$$\tilde{r} = R\hat{r}, \qquad R \triangleq D_e^{-1} D_r. \tag{4.21}$$

From the point of our models, we have state variables; some have much larger or smaller magnitudes or different units than others. For example, the position states are in $meters$, and the angles are defined in rad. Therefore, we use the scaling method in our controller designs to choose weight parameters easily compared to the unscaled models.

4.3 Controller Background and Design

The most commonly used technique for a conventional quadrotor control is to design a PID controller using a cascaded loop controller [43]. In that structure, the inner loop controls the attitude of the body, whereas the outer loop includes a position controller. In this study, we design optimization-based controllers as a single loop, and in this section, we give a brief background about LQR, MPC, and A-MPC methods.

4.3.1 Linear Quadratic Regulator

Linear Quadratic Regulator (LQR) is a type of optimal control based on state-space representation. LQR structure feeds back the entire state vector, then multiplies it by a gain matrix K and subtracts it from the scaled reference. It is like a pole placement technique, but we do not pick the pole locations. We find the optimal K matrix by choosing closed-loop characteristics.

The LQR finds the optimal control input $u[k]$ to the system

$$x[k+1] = Ax[k] + Bu[k], \tag{4.22}$$

that minimizes the following equation

$$\min \sum_{n=0}^{N-1} x^T[n]\mathbf{Q}x[n] + u^T[n]\mathbf{R}u[n]. \tag{4.23}$$

In the equation above, Q and R are positive definite weighting matrices that penalize the state performance and the control effort, respectively.

The quadratic cost function is defined as;

$$J(x, n-1) = \min_u x^T\mathbf{Q}x + u^T\mathbf{R}u + J(Ax + Bu, n). \tag{4.24}$$

Since the cost function is quadratic, let us use a positive definite symmetric matrix S that satisfies the equation below

$$J(x, n) = x^T\mathbf{S}[n]x, \qquad \mathbf{S}[n] = \mathbf{S}^T[n] > 0, \tag{4.25}$$

and we have the optimum control input, $u^*[n]$

$$u^*[n] = -\mathbf{K}[n]x[n] = -(\mathbf{R} + B^T\mathbf{S}[n]B)^{-1}B^T\mathbf{S}[n]Ax[n]. \tag{4.26}$$

Then, (4.26) yields that

$$\mathbf{S}[n-1] = \mathbf{Q} + A^T\mathbf{S}[n]A - (A^T\mathbf{S}[n]B)(\mathbf{R} + B^T\mathbf{S}[n]B)^{-1}(B^T\mathbf{S}[n]A), \quad \mathbf{S}[N] = 0, \tag{4.27}$$

the Riccati difference equation. The infinite horizon LQR solution is found as follows;

$$\mathbf{S} = \mathbf{Q} + A^T\mathbf{S}A - (A^T\mathbf{S}B)(\mathbf{R} + B^T\mathbf{S}B)^{-1}(B^T\mathbf{S}A). \tag{4.28}$$

The general choices for the matrices $\mathbf{Q}$ and $\mathbf{R}$ are based on the *Bryson's* rule [44] which scales the variables in the cost function as follows

$$\mathbf{Q}_{ii} = \frac{1}{\max x_i^2}, \qquad \mathbf{R}_{jj} = \frac{1}{\max u_j^2}. \tag{4.29}$$

Then, they can be tuned by the trial-and-error approach to obtain better performance.

4.3.2 Model Predictive Control

UAVs are vehicles whose velocity and acceleration constraints are critical for the reference tracking problem, and we must consider the constraints to get satisfactory tracking performance. However, LQR does not directly impact the output constraints, whereas the model predictive control determines the optimum control signal using constraints of the output signals directly.

Model Predictive Control (MPC) has been used in the process industry since the 1980s. Richalet et al. [45] presented the first MPC control applications in 1977. As the computing power increases, MPC becomes mostly chosen control algorithm for multivariable control applications in automation, aerospace, energy, and several industries.

The idea behind the MPC is to predict the system's behavior over a specified time horizon and produce a control input sequence that minimizes a predetermined cost function without any input-output violation. It solves an online optimization problem at each time step of the system to select the best control action that drives the states to the desired value. It uses a mathematical model of the plant to run an optimization problem with quadratic programming (QP) to make predictions about future output behaviors, illustrated in Fig. 4.2. By solving an optimization problem, MPC minimizes the error between the set point and the predicted path of the outputs. Additionally, MPC is also known as Receding Horizon Control (RCH) since it moves toward a state farther from the current state. Moreover, the power of the MPC comes from its capability to explicitly handle hard state and input limitations and proper performance criteria in the controller design. Another advantage of the MPC is that it is well suited for multi-input multi-output (MIMO) systems and considers the states' coupling interactions.

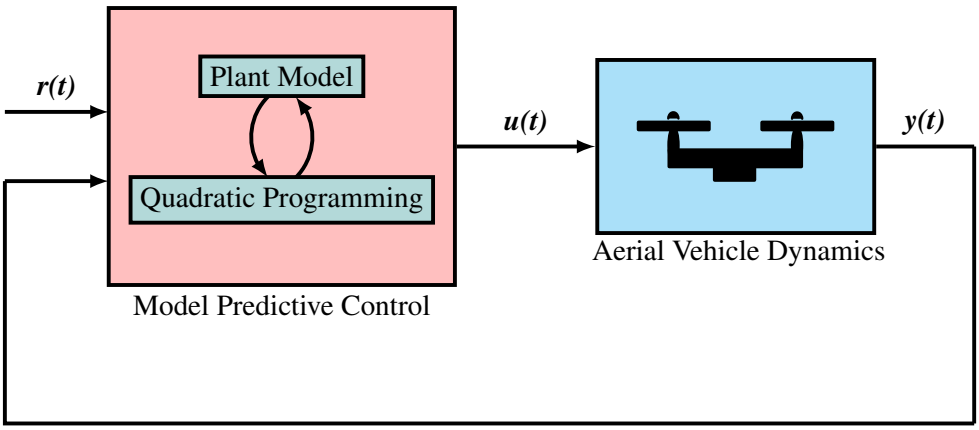

Figure 4.2: Block diagram of the MPC. Model Predictive Control solves an optimization problem at each prediction step with quadratic programming and uses the plant model to predict the future states of the system.

The main part of the MPC is the model used to predict the system's future states. Let us consider the discrete time state space model of the form;

$$x[k+1] = \mathbf{A}x[k] + \mathbf{B}u[k], \tag{4.30}$$

and the variables $x \in \mathbb{R}^n$ and $u \in \mathbb{R}^m$ have constraints

$$x_{min} \leq x \leq x_{max}, \tag{4.31}$$

$$u_{min} \leq u \leq u_{max}. \tag{4.32}$$

The cost function J of the optimization problem is in the form of

$$J = \sum_{i=1}^{N_p} \left(x[k+i-1]^T Q x[k+i-1] + u[k+j-1]^T R u[k+i-1] \right) + x[k+N_p]^T P x[k+N_p], \tag{4.33}$$

where N_p represents the prediction horizon. Q, R, and P are positive semi-definite matrices that weigh the state vector, control effort, and final state value in the prediction horizon, respectively.

The optimization problem minimizes the cost function subject to

$$x_{min} \leq x[k+i] \leq x_{max}, \qquad i = 0, 1, ..., N_p, \tag{4.34}$$

$$u_{min} \leq u[k+i] \leq u_{max}, \qquad i = 0, 1, ..., N_p, \tag{4.35}$$

$$x[k+i+1] = \mathbf{A}x[k+i] + \mathbf{B}u[k+i], \qquad i = 0, 1, ..., N_p - 1. \tag{4.36}$$

And the P matrix can be found by solving the following Riccati equation;

$$P = Q + A^T PA - A^T PB(R + B^T PB)^{-1} B^T PA. \tag{4.37}$$

4.3.2.1 MPC Design Parameters

The performance of the MPC highly depends on the design parameters such as sample time, prediction horizon, control horizon, and weight selections. There are rules of thumb for choosing the proper design parameters in MPC design. In this section, we briefly mention these rules.

Sample time is one of the most critical parameters that should be chosen first. By choosing sample time, we determine the rate at which the controller executes the control algorithm. If it is selected as too big, when a disturbance comes in, the controller cannot be able to react to the disturbance fast enough. On the contrary, if the sample time is too short, the controller responds much faster to the disturbances and set point changes, which causes some overshoots and unneeded computational load. In literature, the suggestion is to choose sample time considering these counter effects such that the open-loop system response has approximately 20 samples within the rise time, T_r.

The number of predicted future time steps is called the prediction horizon, denoted by N_p. It presents how far the controller predicts into the future. We should choose the prediction horizon considering the significant dynamics of the system, which can be measured by examining the open-loop transient response. It is ideal to have sufficient samples covering the settling time, T_{set}. We can choose the prediction horizon as $N_p T_s \geq T_{set}$.

The number of control moves, N_c, to be optimized at the control interval is called a control horizon. After N_c time steps, the inputs stay constant. As N_c increases, we obtain better closed-loop performance, but the computational load increases significantly. Since MPC uses only the first computed control input and ignores the remaining actions, there is no need to choose a massive control horizon parameter. In addition, if the system includes delay, we must select a small N_c to satisfy internal stability. The general rule of thumb is set to control horizon value as 10% of the

prediction horizon.

4.3.3 Adaptive Model Predictive Control

The linear time-invariant (LTI) MPC is for the systems that can be represented by the LTI model with linear constraints so that we build up a quadratic convex cost function. The performance of the LTI MPC depends highly on the accuracy of the model used in the prediction step. For the systems used in this work, linearization only around the hovering state is not a proper method to obtain high performance since the models are highly nonlinear and have differential constraints. In literature, Adaptive MPC, gain-scheduled MPC, and nonlinear MPC have been proposed for highly nonlinear systems to overcome performance reduction. Since the systems we use are nonlinear, but their constraints are linear, we can use linear MPC with two alternatives: Adaptive MPC (A-MPC) and gain-scheduled MPC. A-MPC overcomes the model inaccuracies in real-time by updating the linearized model at each prediction step, whereas the gain-scheduled MPC switches between a predesigned set of MPC controllers for several operating points.

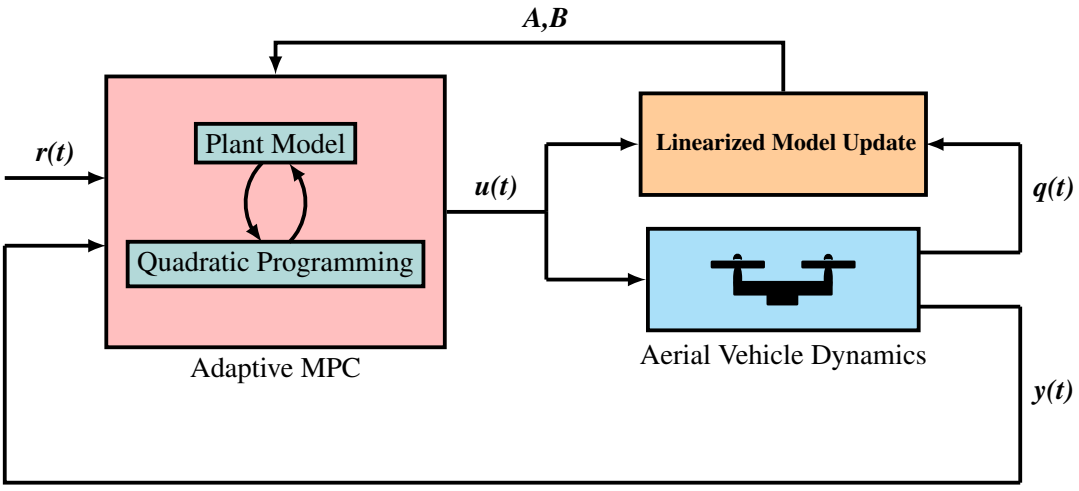

Figure 4.3: Block diagram of the A-MPC. The main difference from the conventional MPC is that it uses a linearized plant model updated for each prediction step to predict future outputs.

Considering that we have the same constraints for all operating points, we can apply adaptive A-MPC to increase the tracking and stabilization performance of the system. As seen in Fig. 4.3, the linearized model is updated using the current state and input variables. The controller then uses the updated model to predict the future states of the systems. Using this approach, we obtain a more accurate model to predict the future at each step. Therefore, A-MPC performs better than the common MPC, especially when the states are far from the hovering state. For the linearized model update block, the linearization equations and the resulting matrices A and B of the systems are given in Appendix A.

CHAPTER 5

MOTION PLANNING

We can roughly define motion planning as the ability to answer the question of how a vehicle can navigate through a defined environment without colliding with obstacles. For aerial locomotion, UAV's motion planning is a more complicated task rather than traditional mobile robots and manipulators. They have limited environmental knowledge because of limited sensors compared to mobile ones. They also have many DOF associated with highly nonlinear equations of motion. Another significant difficulty is that UAVs have differential constraints such as velocity and acceleration, leading engineers to use different techniques for motion planning algorithms.

Most currently used algorithms solve the motion planning problem by decomposing it into stages like solving path planning problems, applying constraints, forming a trajectory, and using feedback control techniques to follow the trajectory.

Karagöz *et al.* [33] proposed a motion planning algorithm, called *MPC-Graph*, consisting of sparse random neighborhood graphs and constrained nonlinear Model Predictive Control (MPC). Atasoy [34] implemented this algorithm's extended and improved version to autonomous surface vessel models. Based on the power of the MPC, which handles constraints very well, we implemented this motion planning algorithm for the proposed aerial vehicle structure.

MPC-Graph algorithm has three consecutive stages to accomplish the motion planning task: sampling-based graph generation, graph search, and motion control based on MPC. The first stage, graph generation, samples the obstacle-free region with overlapping rectangular areas. The graph search algorithm includes Dijkstra's search algorithm [46] to find an optimum path in terms of the predefined cost function. The

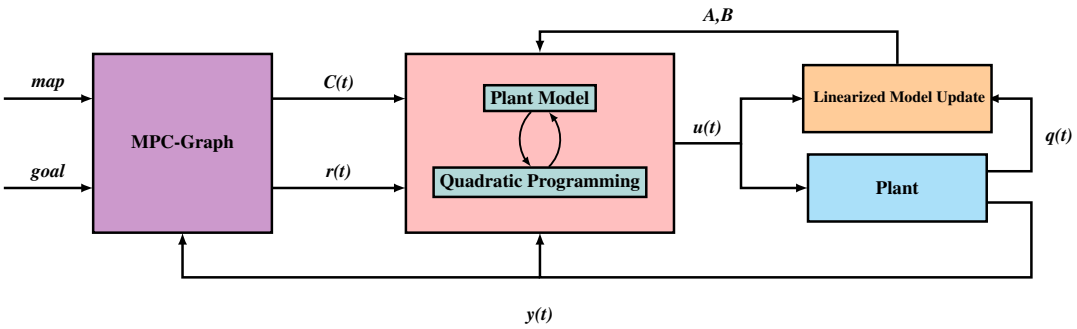

Figure 5.1: Block diagram of the *MPC-Graph* motion planning algorithm with A-MPC. MPC-Graph block takes the map, goal position, and current vehicle states as inputs and generates reference signal, $r(t)$ and constraints, $C(t)$. A-MPC takes these outputs with the linearized model update and generates control input, $u(t)$. At each prediction step, constraints and the linearized model are updated.

last stage is MPC-based motion control. We implement this algorithm using A-MPC instead of nonlinear MPC in the motion control stage. As the aerial vehicle moves from one rectangular region to another, the constraints are updated, and A-MPC takes the aerial vehicle to the goal position without violating these constraints. We represent the block diagram of the algorithm with A-MPC in Fig. 5.1.

5.1 Graph Generation

Let us assume that the aerial vehicle operates in a closed planar ($\mathbb{R}^2$) region called workspace W. The free workspace, W_{free}, is the set of points;

$$W_{free} = W \setminus \bigcup_i W\mathcal{O}_i, \tag{5.1}$$

where $W\mathcal{O}_i$ represents the ith obstacle. Let $\mathcal{C}$ denote configuration space, i.e., the set of configurations of the aerial vehicle with an abdomen-like appendage. $\mathcal{C}_{free}$ is the obstacle-free region in the configuration space, $\mathcal{C}$. Let $\mathcal{B}$ represent the subset of $\mathcal{C}_{free}$ that is covered by rectangular nodes:

$$\mathcal{B} = \bigcup_i Node_i, \tag{5.2}$$

where $Node_i$ is the rectangular region that constructs the graph. Algorithm 1 gives the outline of the graph generation stage step by step. The first step of this algorithm is sampling a random point, q_{rand}, in the obstacle-free region of the map. To get a successful random point, q_{rand}, it should be lied neither in the obstacle region, $q_{rand} \in \mathcal{C}_{free}$, nor in the rectangular regions generated before.

Algorithm 1 Generate Graph

$i = 1$
$G.init(q_{init})$
while $!(TerminationSatisfied(G, P_c, \alpha))$ **do**
  repeat
    $q_{rand_i} \leftarrow GenerateRandomSample()$
    $d = CalculateObstacleDistance(q_{rand_i})$
  until $(d > 0)$ **and** $(q_{rand} \notin \mathcal{B})$
  $C_i \leftarrow GenerateCircle(d)$
  $Node_i \leftarrow GenerateNode(C_i)$
  $Node_i \leftarrow ExpandNode(Node_i)$
  $G.AddNode(Node_i)$
  $i = i + 1$
end while
$G.RemoveRedundantNodes$
$G.RemoveSingletons$
return G

After we get q_{rand} successfully, we obtain the minimum distance from q_{rand} to the obstacles as follows;

$$q_{obs} = \arg \min_{q \in W\mathcal{O}} \|q - q_{rand}\|, \tag{5.3}$$

$$\vec{d}_{min} = q_{rand} - q_{obs}. \tag{5.4}$$

We use the distance, $\|d_{min}\|$, to create the largest possible imaginary circle that is centered at q_{rand} and lies in $\mathcal{C}_{free}$. After this step, the largest square with one edge perpendicular to the vector $\vec{d}_{min}$ is constructed inside the circle. Therefore, we obtain

the node and add it to the graph G after applying the node expansion procedure. Fig. 5.2 illustrates these steps in an environment example.

5.1.1 Node Expansion

Larger nodes are advantageous in terms of computational load and ability to design aggressive feedback motion strategies. To cover more areas in the free space, we extend the generated nodes until they hit an obstacle or area boundaries, as demonstrated in Fig. 5.2.

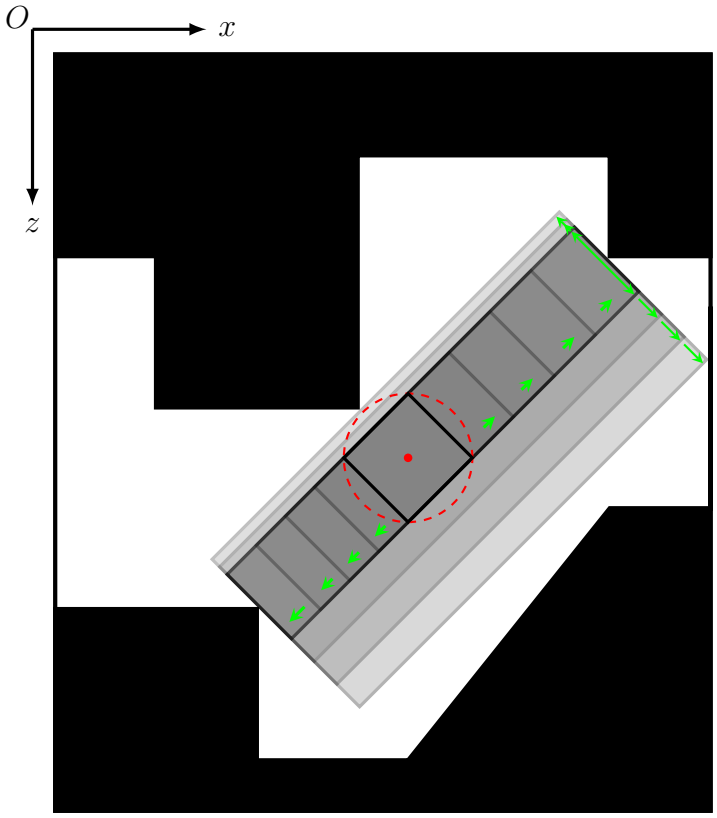

Figure 5.2: Node construction and expansion example. The red dot and the dashed circle represent the q_{rand} and the imaginary circle. The black node is the first generated square node. By expanding this square node along the direction that green arrows indicate, the expanded node is generated.

The first step in the node expansion procedure is extending the obtained square node in the direction perpendicular to the vector $\vec{d}_{min}$ until the node meets the obstacle or

the environment's boundaries. If the node hits the obstacle or edge of the environment, it comes one step back. Then, we apply the same extension procedure to the direction along the $\vec{d}_{min}$ with the new rectangular region.

The overall algorithm continues to sample and expand nodes until the Bayesian termination condition is satisfied, meaning that $TerminationSatisfied(G, P_c, \alpha)$ returns true. Yang and Lavalle [32] reports the Bayesian termination condition based on the equation below;

$$m \geq \frac{\ln(1 - Pc)}{\ln \alpha} - 1, \tag{5.5}$$

where m is the number of consecutive failures after the first success of generating a random point in $\mathcal{C}_{free}$, α is the percentage of the area covered by the rectangular nodes in $\mathcal{C}_{free}$ with probability P_c.

In conclusion, by generating q_{rand} and $Node_i$ successfully, we apply the following rules;

- Point q_{rand} should be lied neither in the obstacle region, $q_{rand} \in \mathcal{C}_{free}$, nor in the nodes generated before, $q_{rand} \notin \mathcal{B}$.
- If the generated node is a subset of other nodes or overlaps with any nodes with a ratio greater than 90%, it should be removed from the graph.
- If the generated node does not intersect with any nodes, it should also be removed from the graph.

Fig. 5.3 illustrates the example of the planar environment that an aerial vehicle navigates and the randomly generated graph.

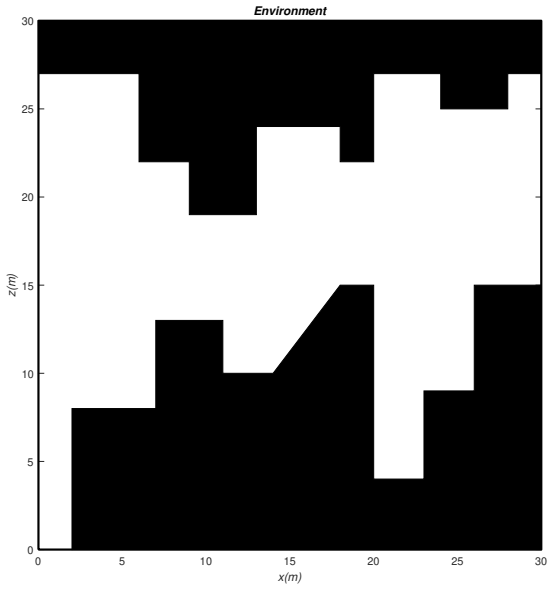

(a) Environment

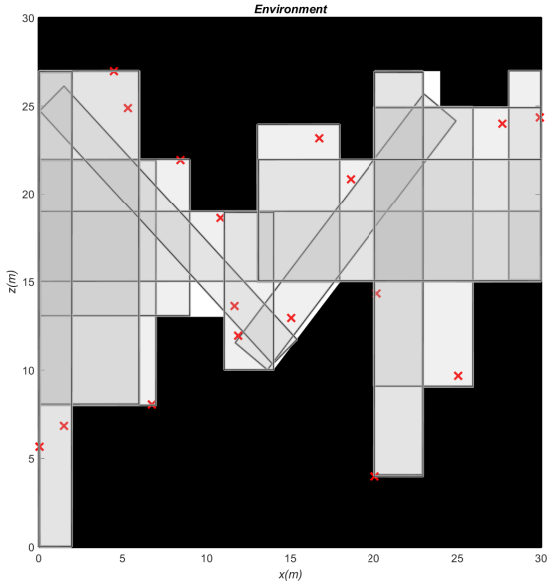

(b) Random samples and generated nodes

Figure 5.3: Example of the generated nodes in the planar environment: (a) an environment example with static obstacles, (b) the generated random points represented by red markers, and the related extended nodes.

5.2 Dijkstra's Search Algorithm

The motion planning algorithm starts to search the constructed graph after the termination condition in (5.5) is satisfied. Next, the algorithm finds the center of each overlapping area $A_{i,i+1}$, which is the intersection area of the node N_i and N_{i+1} in the map. Then for each overlapping region, the cost function, J_{nodes} is constructed using the equation that Atasoy reported [34];

$$J_{nodes} = \|C_{N_i} - C_{A_i}\| + \|C_{N_{i+1}} - C_{A_i}\| + \frac{1}{A_{i,i+1}}, \tag{5.6}$$

where C_{N_i} is the center of the $Node_i$, shown in Fig. 5.4. The cost function includes the distances from the center of the overlapping area to the center of the corresponding node. In addition, the size of the overlapping area inversely increases the cost because the larger areas allow vehicles to move faster.

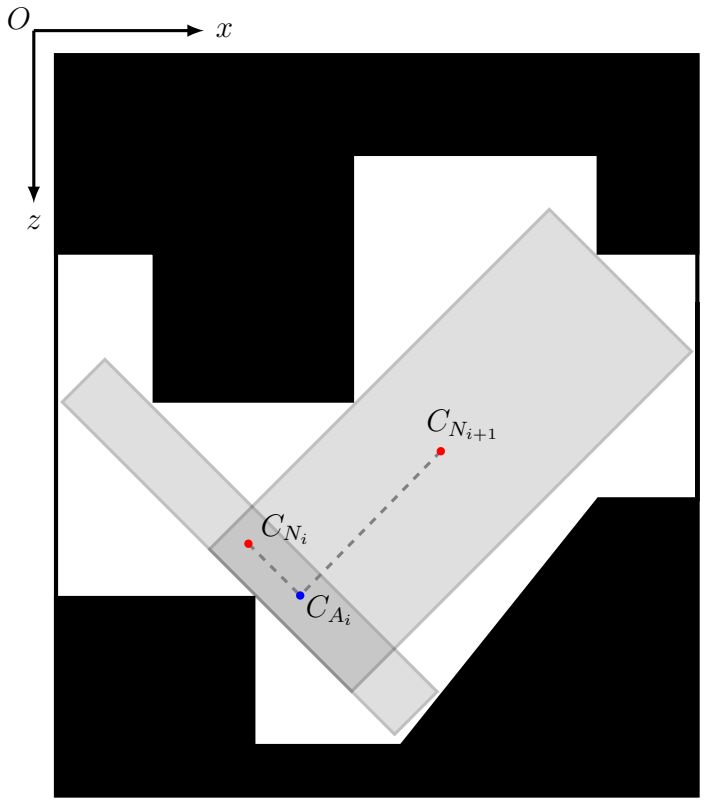

Figure 5.4: Illustration of the cost parameters. The distances are represented with a dashed line. The red dots represent the center points of the corresponding node, whereas the blue one represents the center of the overlapping area.

Based on this cost function, we use Dijkstra's search algorithm to find the optimum trajectory that takes the aerial vehicle from the start to the goal point. Then, we move on to the next stage, A-MPC based motion control algorithm, after obtaining the optimum trajectory, as shown in Fig. 5.5.

5.3 A-MPC Based Motion Control

The last stage of the MPC-Graph motion planning algorithm is motion control. This section implements the A-MPC control strategy instead of the nonlinear MPC as a feedback motion strategy. This stage is mainly responsible for navigating the aerial vehicle from its start to the goal position using the previously calculated trajectory.

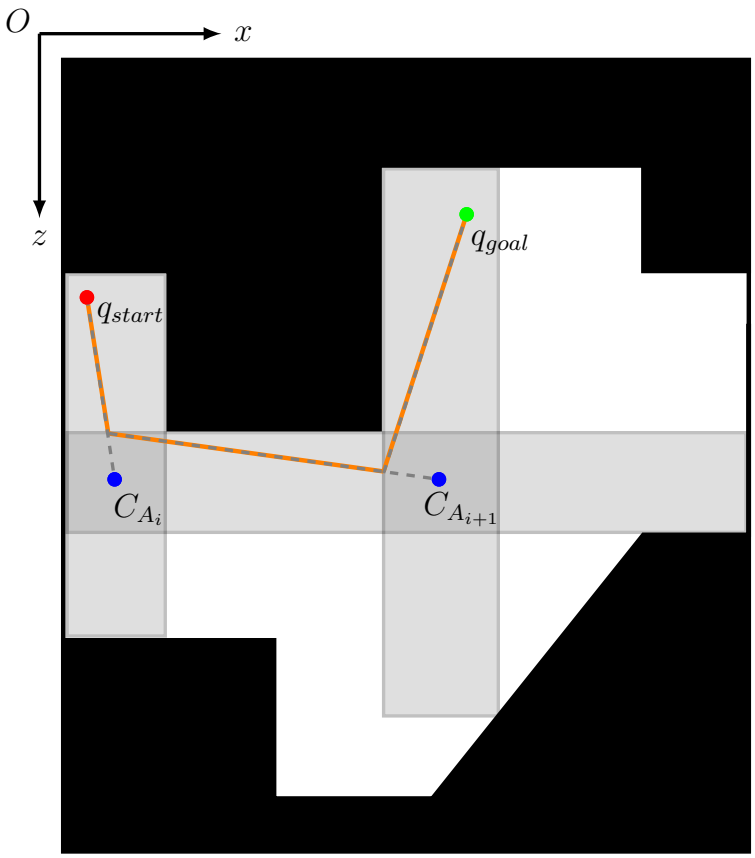

Figure 5.5: Illustration of the motion control algorithm. The dashed lines represent the path to the center of the intersection areas. The orange lines indicate the vehicle's path as the current node is updated.

The motion control algorithm starts with detecting the node that the vehicle is currently in it. Dijkstra's search algorithm selects the next node based on our constructed cost function. Then, the algorithm computes the reference signal as the center of the intersection area of the current node and the next node. When the vehicle moves to the next node, the algorithm assigns the next node to the current node and updates the next node. The reference signal is also updated as the center of the intersection area of the updated current and next node. Additionally, as the current node changes, the output constraints are updated according to the boundaries of the new current node.

The algorithm executes until the robot is currently in the node containing the q_{goal}. If the vehicle moves to the point that is not in the sets of the nodes, $\mathcal{B}$, new nodes are constructed, and the path is updated to reach q_{goal}. Algorithm 2 gives detailed steps about the motion control stage. After the algorithm finds the current and next node, A-MPC generates the control input u_{curr} using the corresponding reference signal. If somehow the vehicle is in the unsampled region in the environment, then the algorithm uses the node generation stage again for the current vehicle point q_{curr}. If the vehicle is already in the node that contains q_{goal}, it directly uses the point q_{goal} as a reference signal.

Algorithm 2 A-MPC Based Motion Control

$currentNode \leftarrow FindCurrentNode(G, q_{curr})$

$[nextNode, intersectionArea] \leftarrow Path.Next(currentNode)$

$refSignal \leftarrow FindCenteroid(intersectionArea)$

while $q_{curr} != q_{goal}$ **do**

  if $q_{curr} \in goalNode$ **then**

    $refSignal \leftarrow q_{goal}$

  else if $q_{curr} \in nextNode$ **then**

    $currentNode \leftarrow nextNode$

    $[nextNode, intersectionArea] \leftarrow Path.Next(currentNode)$

    $refSignal \leftarrow FindCenteroid(intersectionArea)$

  else if $q_{curr} \notin \mathcal{B}$ **then**

    $d = CalculateObstacleDistance(q_{curr})$

    $C \leftarrow GenerateCircle(d)$

    $Node \leftarrow GenerateNode(C)$

    $Node \leftarrow ExpandNode(Node)$

    $G.AddNode(Node)$

    $Path \leftarrow DijkstraSearchAlgorithm(G)$

    $currentNode \leftarrow Node$

    $[nextNode, intersectionArea] \leftarrow Path.Next(currentNode)$

    $refSignal \leftarrow FindCenteroid(intersectionArea)$

  else

    $currentNode \leftarrow FindCurrentNode(G, q_{curr})$

    $[nextNode, intersectionArea] \leftarrow Path.Next(currentNode)$

    $refSignal \leftarrow FindCenteroid(intersectionArea)$

  end if

  $u_{curr} \leftarrow AdaptiveMPC(q_{curr}, refSignal, currentNode)$

end while

CHAPTER 6

IMPLEMENTATION AND RESULTS

This chapter performs several simulations to analyze the performance of the proposed systems compared to conventional aerial vehicles. We used MATLAB Simscape Multibody to verify the derived equations of motion of the bi-rotor and quadrotor platforms with/without appendage. We implemented the controller designs and the motion planning algorithm in MATLAB Simulink [36].

6.1 Planar Models with Bi-rotor Platform

Firstly, we start with the bi-rotor platform models with and without an abdomen-like appendage with the controller designs explained in Chapter 4. We begin with LQR and then move to MPC and A-MPC designs and implementations.

6.1.1 Linear Quadratic Regulator

LQR performance depends highly on the selection of the weighting matrices. Tuning the weight matrices is an iterative process in which we analyze the plant's response and modify the weights according to the performance criteria. To make a fair comparison between the conventional and the proposed system, we first start selecting the weight matrices such that the weighting parameters of the appendage state θ_2 and $\dot{\theta}_2$ are equal to zero. On the other hand, we propose this structure to increase the body states' performance and optimize the propellers' control effort. Thus, we do not penalize the appendage actuator control input, τ, since the highly actuated insect abdomen muscles inspire it. However, for weighing the control efforts, we cannot

entirely make zero the corresponding weight for the input τ because it makes the R matrix singular. One possible solution is to give a smaller non-zero value to the weighting parameter of the input τ. The other solution is making the $Frobenius$ norm of the R matrices equal.

Let the R_{conv} and R_{app} represent the input weighting matrices for the conventional bi-rotor platform and the one with an appendage, respectively;

$$R_{conv} = \begin{bmatrix} a_{11} & 0 \\ 0 & a_{22} \end{bmatrix}, \qquad R_{app} = \begin{bmatrix} b_{11} & 0 & 0 \\ 0 & b_{22} & 0 \\ 0 & 0 & b_{33} \end{bmatrix}. \tag{6.1}$$

Since the input F_1 and F_2 are assumed to be generated by the identical actuators, we penalize them in the same way, meaning that $a_{11} = a_{22}$ and $b_{11} = b_{22}$. Thus, weighting parameters are supposed to satisfy the equation below to have an equal $Frobenius$ norm;

$$\sqrt{a_{11}^2 + a_{22}^2} = \sqrt{b_{11}^2 + b_{22}^2 + b_{33}^2}. \tag{6.2}$$

Therefore, as a first approach, we choose the weighting matrices for the conventional bi-rotor platform $Q_{conv} = I_{6x6}$, $R_{conv} = I_{2x2}$ and for the one with an appendage as follows;

$$Q_{app} = \begin{bmatrix} 1 & 0 & 0 & 0 & 0 & 0 & 0 & 0 \\ 0 & 1 & 0 & 0 & 0 & 0 & 0 & 0 \\ 0 & 0 & 1 & 0 & 0 & 0 & 0 & 0 \\ 0 & 0 & 0 & 0 & 0 & 0 & 0 & 0 \\ 0 & 0 & 0 & 0 & 1 & 0 & 0 & 0 \\ 0 & 0 & 0 & 0 & 0 & 1 & 0 & 0 \\ 0 & 0 & 0 & 0 & 0 & 0 & 1 & 0 \\ 0 & 0 & 0 & 0 & 0 & 0 & 0 & 0 \end{bmatrix}, \qquad R_{app} = \begin{bmatrix} 1 & 0 & 0 \\ 0 & 1 & 0 \\ 0 & 0 & 0.01 \end{bmatrix}. \tag{6.3}$$

With these matrices, we obtain state feedback gains K_{conv} and K_{app} for the conventional bi-rotor and the proposed one as follows;

$$K_{conv} = \begin{bmatrix} 0.7071 & 0.7071 & -5.3949 & 1.1304 & 1.4460 & -1.3696 \\ -0.7071 & 0.7071 & 5.3949 & -1.1304 & 1.4460 & 1.3696 \end{bmatrix}, \tag{6.4}$$

$$K_{app} = \begin{bmatrix} 0.3501 & 0.7071 & -1.1010 & -0.0678 & 0.4403 & 1.4460 & -0.3393 & -0.0479 \\ -0.3501 & 0.7071 & 1.1010 & 0.0678 & -0.4403 & 1.4460 & 0.3393 & 0.0479 \\ 8.6886 & 0 & -53.9866 & -0.5573 & 13.2109 & 0 & -10.3399 & 0.5297 \end{bmatrix}. \tag{6.5}$$

We apply these state feedback gains to linearized and nonlinear plant models with initially perturbed body angle, $\theta_{10} = 15°$. The responses of the states are shown in Fig. 6.1.

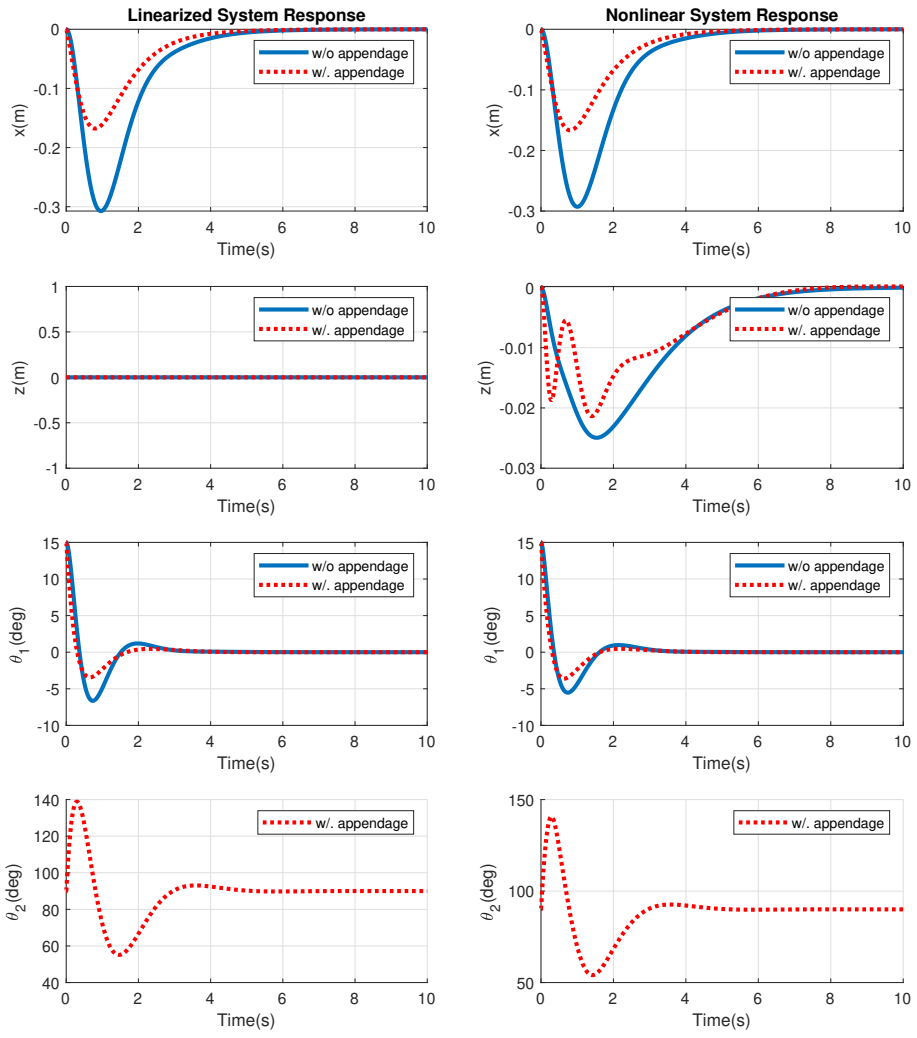

Figure 6.1: LQR controller response of the linearized and nonlinear systems with initially perturbed body angle ($\theta_{10} = 15°$)

The results show that the appendage enhances the stabilization of the bi-rotor body angle with the help of redirecting thrust forces. The advantage can be seen for the linearized model, whereas the nonlinear dynamics slightly reduce the performance improvement. The x position response also gives remarkably better results with the appendage since the angle change affects the horizontal movement directly.

We choose different weighting parameters to compare the conventional bi-rotor platform and the one with appendage as depicted in Table 6.1 and 6.2. We examine the step response of the position x with initial body perturbation $\theta_{10} = 5°$. Table 6.1 expresses the results of the step response for both systems in terms of performance metrics such as overshoot M_p, settling time T_{sett}, steady state error E_{ss}, and the average cost J. With this analysis, we can conclude that the appendage improves the position x response in settling time, T_{sett}, and it simultaneously reduces the average cost, J.

Table 6.1: Step response analysis of the position x for the bi-rotor platforms with-/without appendage

$\boldsymbol{Q_{diag}}$	$\boldsymbol{R_{diag}}$	$\boldsymbol{M_p}(\%)$	$\boldsymbol{T_{sett}}(\boldsymbol{s})$	$\boldsymbol{E_{ss}}(\%)$	$\boldsymbol{J}$
w/o appendage $Q_{diag} = \{1,1,1,1,1,1\}$	**w/o appendage** $R_{diag} = \{1,1\}$	0	4.66	0	1.5043
w/. appendage $Q_{diag} = \{1,1,1,\mathbf{0},1,1,1,\mathbf{0}\}$	**w/. appendage** $R_{diag} = \{1,1,\mathbf{0.01}\}$	0	4.50	0	1.4358
w/o appendage $Q_{diag} = \{1,1,1,1,1,1\}$	**w/o appendage** $R_{diag} = \{10,10\}$	0	4.99	0	1.6693
w/. appendage $Q_{diag} = \{1,1,1,\mathbf{0},1,1,1,\mathbf{0}\}$	**w/. appendage** $R_{diag} = \{10,10,\mathbf{0.01}\}$	0	4.47	0	1.4608
w/o appendage $Q_{diag} = \{1,1,10,1,1,1\}$	**w/o appendage** $R_{diag} = \{1,1\}$	0	4.62	0	1.5549
w/. appendage $Q_{diag} = \{1,1,10,\mathbf{0},1,1,1,\mathbf{0}\}$	**w/. appendage** $R_{diag} = \{1,1,\mathbf{0.01}\}$	0	4.51	0	1.4920
w/o appendage $Q_{diag} = \{1,1,10,1,1,1\}$	**w/o appendage** $R_{diag} = \{10,10\}$	0	4.98	0	1.7083
w/. appendage $Q_{diag} = \{1,1,10,\mathbf{0},1,1,1,\mathbf{0}\}$	**w/. appendage** $R_{diag} = \{10,10,\mathbf{0.01}\}$	0	4.46	0	1.5136
w/o appendage $Q_{diag} = \{10,1,10,1,1,1\}$	**w/o appendage** $R_{diag} = \{1,1\}$	2.55	1.72	0	8.9456
w/. appendage $Q_{diag} = \{10,1,10,\mathbf{0},1,1,1,\mathbf{0}\}$	**w/. appendage** $R_{diag} = \{1,1,\mathbf{0.01}\}$	1.64	1.65	0	8.6899

We apply the same procedure to the position z, and the results are given in Table 6.2. The table shows that the proposed system slightly overshoots, whereas the conventional one does not. When we compare the average costs, the conventional bi-rotor platform has a slightly lower average cost for the state z. Nonetheless, settling time is significantly improved compared to the step response of the conventional bi-rotor platform.

Table 6.2: Step response analysis of the position z for the bi-rotor platforms with-/without appendage

$\boldsymbol{Q_{diag}}$	$\boldsymbol{R_{diag}}$	$\boldsymbol{M_p}(\%)$	$\boldsymbol{T_{sett}}(s)$	$\boldsymbol{E_{ss}}(\%)$	$\boldsymbol{J}$
w/o appendage $Q_{diag} = \{1, 1, 1, 1, 1, 1\}$	**w/o appendage** $R_{diag} = \{1, 1\}$	0	5.94	0	1.9034
w/. appendage $Q_{diag} = \{1, 1, 1, \mathbf{0}, 1, 1, 1, \mathbf{0}\}$	**w/. appendage** $R_{diag} = \{1, 1, \mathbf{0.01}\}$	1.2	4.85	0	1.9651
w/o appendage $Q_{diag} = \{1, 1, 1, 1, 1, 1\}$	**w/o appendage** $R_{diag} = \{10, 10\}$	0	8.82	0	2.6560
w/. appendage $Q_{diag} = \{1, 1, 1, \mathbf{0}, 1, 1, 1, \mathbf{0}\}$	**w/. appendage** $R_{diag} = \{10, 10, \mathbf{0.01}\}$	3	7.45	0	2.7940
w/o appendage $Q_{diag} = \{1, 1, 10, 1, 1, 1\}$	**w/o appendage** $R_{diag} = \{1, 1\}$	0	5.93	0	1.9082
w/. appendage $Q_{diag} = \{1, 1, 10, \mathbf{0}, 1, 1, 1, \mathbf{0}\}$	**w/. appendage** $R_{diag} = \{1, 1, \mathbf{0.01}\}$	1.2	4.85	0	1.9710
w/o appendage $Q_{diag} = \{1, 1, 10, 1, 1, 1\}$	**w/o appendage** $R_{diag} = \{10, 10\}$	0	8.82	0	3.0239
w/. appendage $Q_{diag} = \{1, 1, 10, \mathbf{0}, 1, 1, 1, \mathbf{0}\}$	**w/. appendage** $R_{diag} = \{10, 10, \mathbf{0.01}\}$	3.1	7.52	0	3.2105
w/o appendage $Q_{diag} = \{10, 1, 10, 1, 1, 1\}$	**w/o appendage** $R_{diag} = \{1, 1\}$	0	5.94	0	1.9071
w/. appendage $Q_{diag} = \{10, 1, 10, \mathbf{0}, 1, 1, 1, \mathbf{0}\}$	**w/. appendage** $R_{diag} = \{1, 1, \mathbf{0.01}\}$	1.2	4.86	0	2.2267

Moreover, stabilizing the body attitude is critical for aerial vehicles. Therefore, we apply both step input to the x and z position, and we analyze the body angle response with initial condition $\theta_{10} = 5^\circ$. Table 6.3 indicates the results with previously chosen weighting parameters. The body angle settles down its steady state value, which is zero, by making some amount of overshoots. This time, we compare the responses using overshoot value and zero-crossing time. We define zero-crossing time as when

the state crosses its steady state value for the first time. Table 6.3 shows that the average cost J decreases with improved zero-crossing time with the proposed structure.

Table 6.3: Performance analysis for the angle θ_1 of the bi-rotor platforms with/without appendage

$\boldsymbol{Q_{diag}}$	$\boldsymbol{R_{diag}}$	**Overshoot value** (deg)	**Zero-crossing time** (s)	$\boldsymbol{J}$
w/o appendage $Q_{diag} = \{1, 1, 1, 1, 1, 1\}$	**w/o appendage** $R_{diag} = \{1, 1\}$	-6.52	1.18	3.0856
w/. appendage $Q_{diag} = \{1, 1, 1, \mathbf{0}, 1, 1, 1, \mathbf{0}\}$	**w/. appendage** $R_{diag} = \{1, 1, \mathbf{0.01}\}$	-6.03	1.04	3.0519
w/o appendage $Q_{diag} = \{1, 1, 1, 1, 1, 1\}$	**w/o appendage** $R_{diag} = \{10, 10\}$	-5.38	1.56	4.7073
w/. appendage $Q_{diag} = \{1, 1, 1, \mathbf{0}, 1, 1, 1, \mathbf{0}\}$	**w/. appendage** $R_{diag} = \{10, 10, \mathbf{0.01}\}$	-6.55	0.97	4.6327
w/o appendage $Q_{diag} = \{1, 1, 10, 1, 1, 1\}$	**w/o appendage** $R_{diag} = \{1, 1\}$	-6.06	1.21	3.4806
w/. appendage $Q_{diag} = \{1, 1, 10, \mathbf{0}, 1, 1, 1, \mathbf{0}\}$	**w/. appendage** $R_{diag} = \{1, 1, \mathbf{0.01}\}$	-5.51	1.07	3.4489
w/o appendage $Q_{diag} = \{1, 1, 10, 1, 1, 1\}$	**w/o appendage** $R_{diag} = \{10, 10\}$	-5.12	1.58	4.7418
w/. appendage $Q_{diag} = \{1, 1, 10, \mathbf{0}, 1, 1, 1, \mathbf{0}\}$	**w/. appendage** $R_{diag} = \{10, 10, \mathbf{0.01}\}$	-6.04	1.01	4.6893
w/o appendage $Q_{diag} = \{10, 1, 10, 1, 1, 1\}$	**w/o appendage** $R_{diag} = \{1, 1\}$	-12.8	2.55	9.8375
w/. appendage $Q_{diag} = \{10, 1, 10, \mathbf{0}, 1, 1, 1, \mathbf{0}\}$	**w/. appendage** $R_{diag} = \{1, 1, \mathbf{0.01}\}$	-13.3	2.45	9.7317

The next analysis is to demonstrate the effect of the torque limit-constraint, $|\tau| \leq \tau_{max}$. Given enough torque, the simulation results show that the appendage improves the tracking and stabilization performance. It means that, as highly actuated abdomen reflexes improve head stabilization of the flying animals, the abdomen-like appendage with unlimited actuator performs better for multi-rotor aerial vehicles. However, in the real world, the actuators have limits, and we need to analyze the proposed system with these limits to ensure that the proposed system still has an advantage in these conditions.

For a simple pendulum system with mass m and length ℓ, if the maximum torque is greater than $mg\ell$, we can drive and stabilize the pendulum by finding a feasible con-

trol input. The system becomes interesting when we have a torque limit smaller than mgl because we cannot achieve the control task for some states. Since we modeled the appendage as a pendulum, we analyzed the system with different torque limits around the value of the mgl Nm.

We give the initial condition to the body angle $\theta_1 = 30^\circ$ for the nonlinear models and observe the state responses in different torque-limit conditions. The x and z position responses given in Fig. 6.2, show that the better response is achieved with the unlimited torque input, $\tau_{max} = \infty$. The response worsens when we decrease τ_{max} step by step. However, the worst case with $\tau_{max} = 1$ Nm, still gives better response than the conventional bi-rotor platform for x-position. For the position z, the torque limit does not ruin the appendage's advantages for the vertical motion until $\tau_{max} = 1$ Nm. For the case, $\tau_{max} = 1$, the performance of the conventional bi-rotor platform is better in terms of the overshoot parameter. However, the proposed system still converges faster.

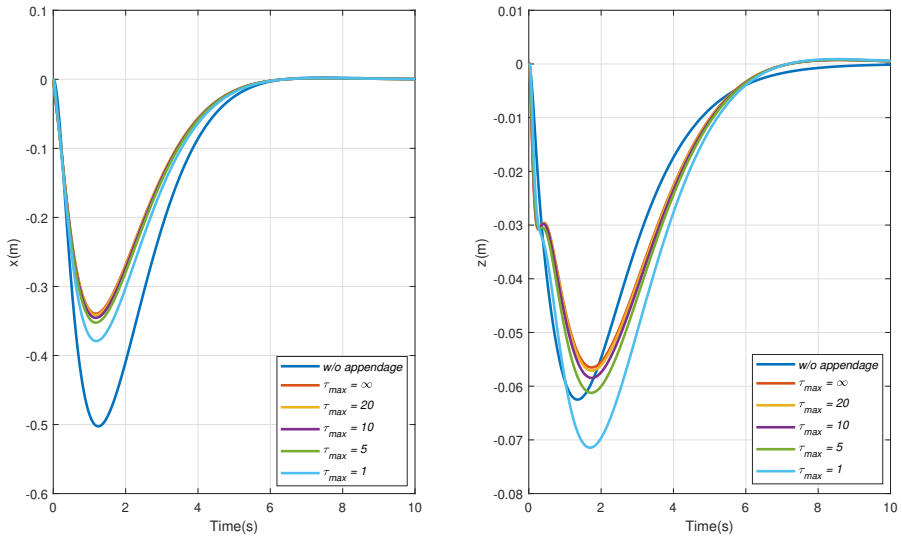

Figure 6.2: Analysis of how torque constraint affects the response of the translational movements, x and z.

Furthermore, the bi-rotor platform without an appendage performs worst in stabilizing the body attitude. Fig. 6.3 shows the body and the appendage angle responses under different torque limits. The appendage increases the attitude stabilization performance even if there is a hard torque-limit constraint. On the other hand, for the case $\tau_{max} \geq 20$ Nm, the appendage angle θ_2 reaches its maximum limit. Another remark from this analysis is that even if we do not have a torque-limit constraint, the system has mechanical limits for the appendage angle that needs to be considered.

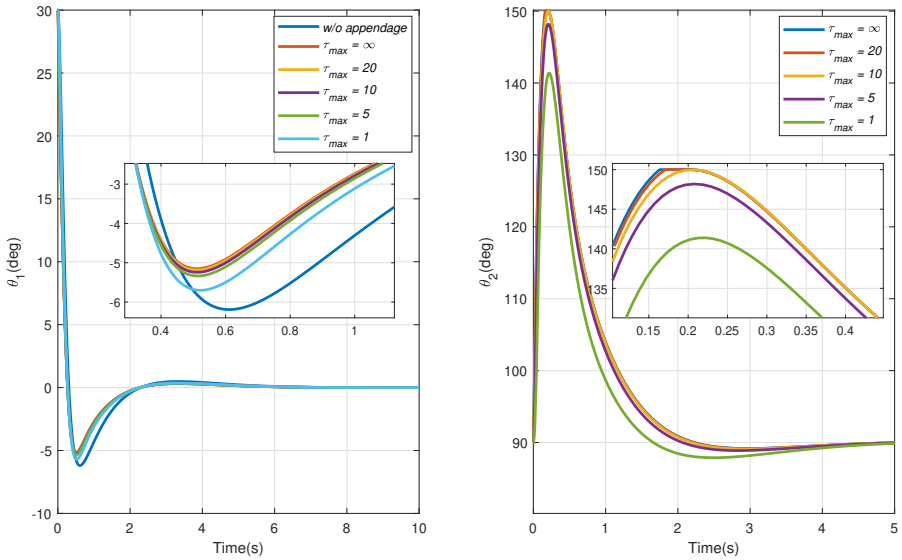

Figure 6.3: Analysis of how torque constraint affects the response of the body attitude, θ_1, and appendage angle, θ_2.

Fig. 6.4 presents the control efforts of the propellers with different appendage torque-limit constraints. The appendage reduces the control effort belonging to the propellers, F_1 and F_2. The main task of the propellers is to overcome gravity, and the appendage assists the propellers with the body's orientation and horizontal movement. As a result, we can consider this remark as another benefit of the abdomen-like appendage.

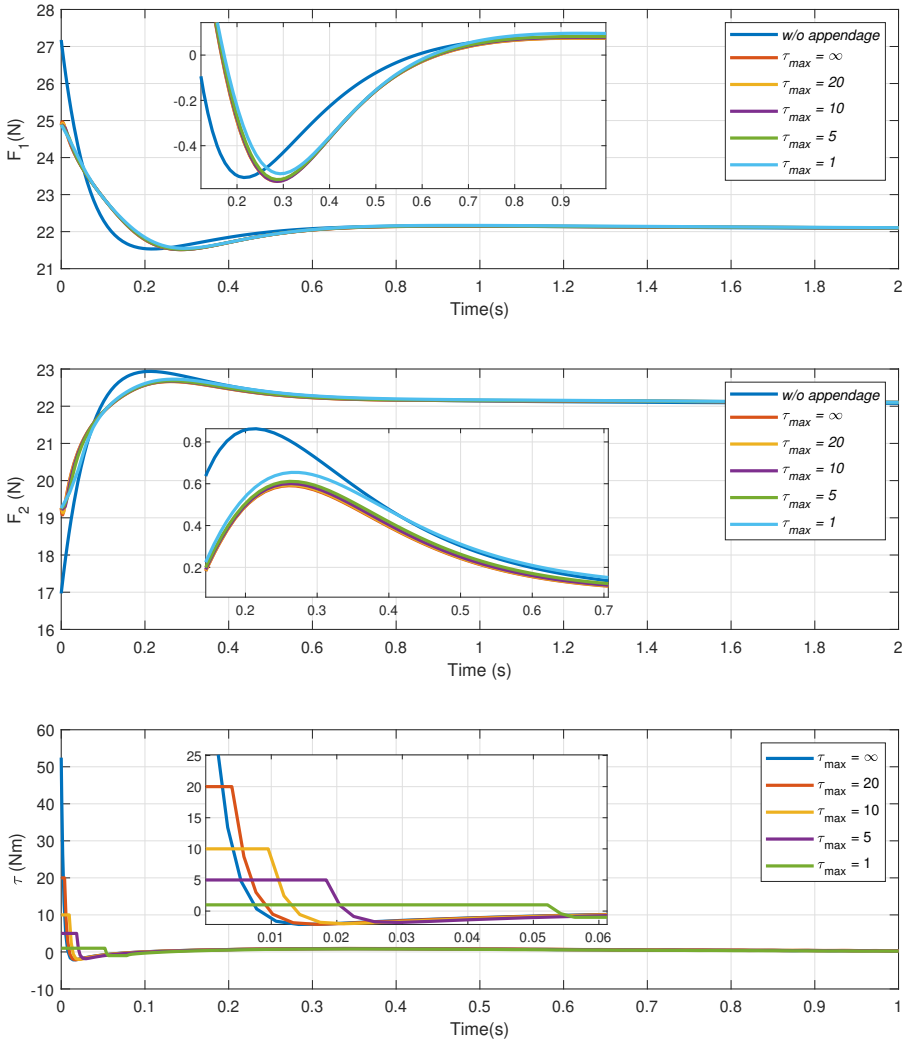

Figure 6.4: Control efforts of the propellers, F_1 and F_2, with different appendage torque-limit constraints, τ_{max}, and the appendage actuator response, τ.

6.1.2 Model Predictive Control

Model predictive control mainly differs from the LQR by constructing the cost function. In LQR, the weighting matrices Q and R correspond to the internal states $x(k)$ and $u(k)$. The input-output constraints are not considered while calculating the cost function.

Another difference is that LQR optimization is done for the whole horizon, whereas MPC optimizes its controller in a receding horizon. Therefore, the optimization problem of the MPC may have a suboptimal solution. On the other hand, MPC handles nonlinearities and hard constraints, which is the MPC's primary advantage over the LQR.

First, we choose the MPC design parameters, which are indicated in Table 6.4. We choose sample time, T_s, identical to the linearized model update rate, as 0.05 seconds. The prediction and control horizon parameters are tuned by using the trial and error method. We increase the prediction horizon step by step and examine the controller performance. When the performance improvement stops, we choose that value as the prediction horizon length. We pay attention not to increasing the control horizon too much since it adds computational load to the controller. Moreover, we try to select closer MPC parameters for both systems. Then, we tune the parameters to get a better response for each system. We choose a slightly smaller control horizon value for the conventional bi-rotor platform to get better performance. The constraints are chosen according to the assumptions made in Chapter 4. In addition, we used a scaled state space model to tune weighting parameters easily. We increase the weight of the body angle since it is the most crucial factor in improving the stabilization performance of the system.

Table 6.4: Comparison of the MPC parameters for bi-rotor platform with/without appendage

MPC Parameters	**w/o appendage**	**w/. appendage**
Sample Time, T_s	0.05 seconds	0.05 seconds
Prediction Horizon, N_p	45 steps	45 steps
Control Horizon, N_c	6 steps	10 steps
Input Constraints	**Min:** [0, 0] **Max:** [30, 30]	**Min:** [0, 0, -5] **Max:** [30, 30, 5]
Output Constraints	**Min:** [-30, -30, -$\frac{\pi}{3}$, -∞, -∞, -∞] **Max:** [30, 30, $\frac{\pi}{3}$, ∞, ∞, ∞]	**Min:** [-30, -30, -$\frac{\pi}{3}$, $\frac{\pi}{6}$, -∞, -∞, -∞, -∞] **Max:** [30, 30, $\frac{\pi}{3}$, $\frac{5\pi}{6}$, ∞, ∞, ∞, ∞]
Input Weights	**Weight:** [1,1] **Rate Weight:** [0.1,0.1]	**Weight:** [1,1,0.1] **Rate Weight:** [0.1,0.1,0.1]
Output Weights	[1,1,10,1,1,1]	[1,1,10,0.1,1,1,1,0.1]

Then, we compare the MPC performance with constrained LQR. Fig. 6.5 shows the step response of the system's x and z positions with constrained LQR and MPC. The left side of the figure indicates the constrained LQR responses of the bi-rotor platforms with/without appendage. In contrast, the right side demonstrates the MPC responses. The appendage angle reached its limit in the constrained LQR case, whereas MPC gives a better solution with optimal appendage movement.

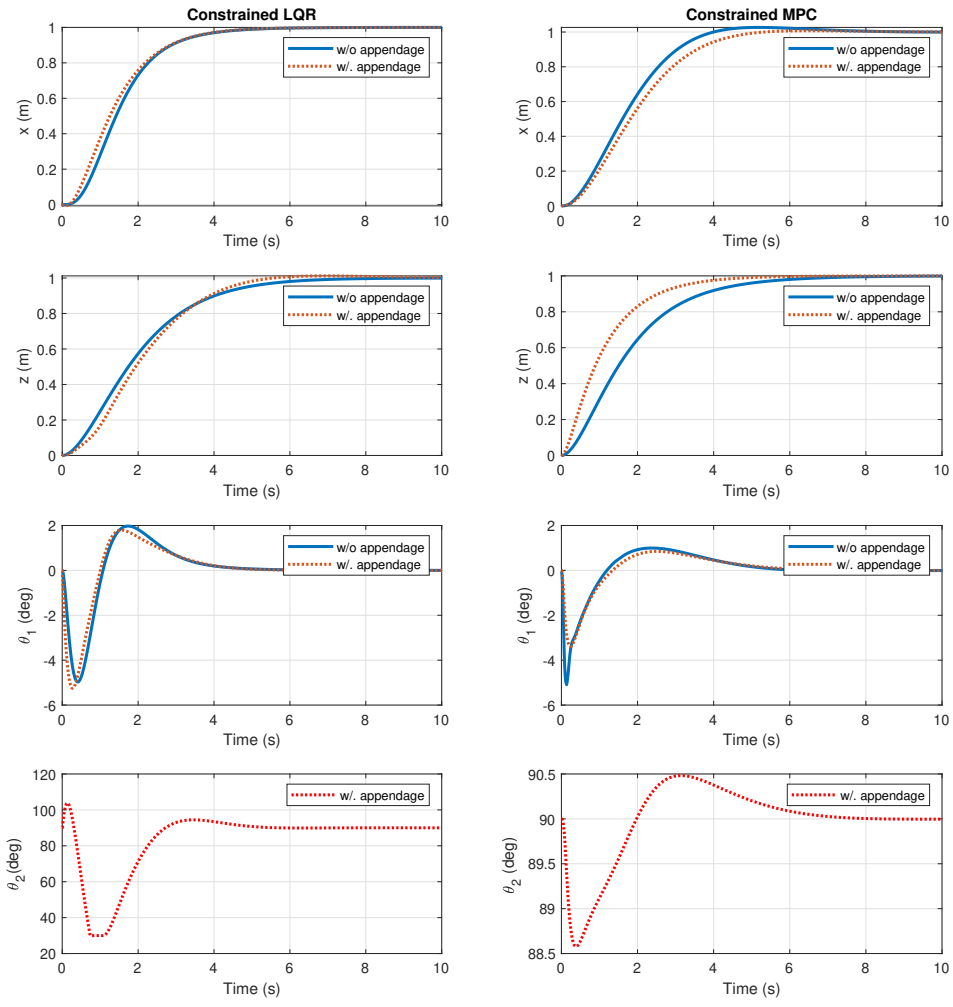

Figure 6.5: Constrained LQR and MPC responses of the bi-rotor platforms with/without appendage

6.1.3 Adaptive Model Predictive Control

We design A-MPC for the conventional and proposed bi-rotor platforms as a final controller approach. We use the MPC, which we already tuned in the previous section, to implement the A-MPC. Then, we update the plant model by linearizing it using the current states and the current input values at the beginning of each prediction step so that the update rate equals the controller's sample time, $T_s = 0.05$. Fig. 6.6 shows the responses of the conventional bi-rotor platform with three configurations: linearized plant model with conventional MPC (MPC_{lp}), nonlinear plant model with conventional MPC (MPC_{np}), and nonlinear plant model with adaptive MPC ($AMPC_{np}$).

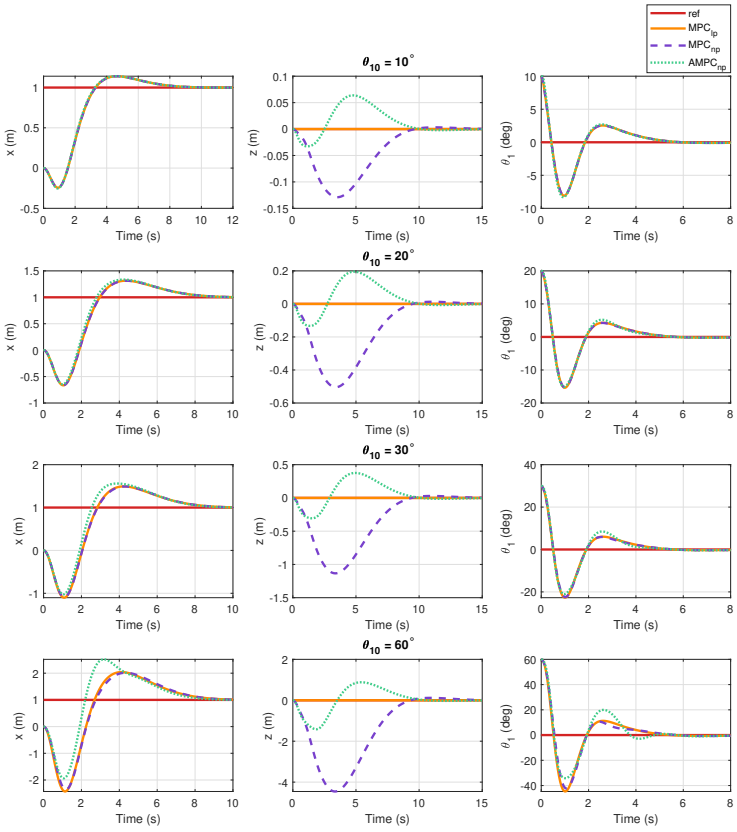

Figure 6.6: The state responses of the conventional bi-rotor platform under different initial body angle with A-MPC.

We give different initial conditions to the body angle and step input to the x position for the test scenario. As seen from the results, when we linearize the model only

at the hovering state, we lose the coupling effects between the z position and other body states. Thus, using this plant model in the prediction step of the MPC gives a significant performance degradation in the z position. Updating the linearized plant model at each prediction step enhances the performance of the z response. Also, the results indicate that the A-MPC becomes more advantageous when the system is far from its nominal operating point.

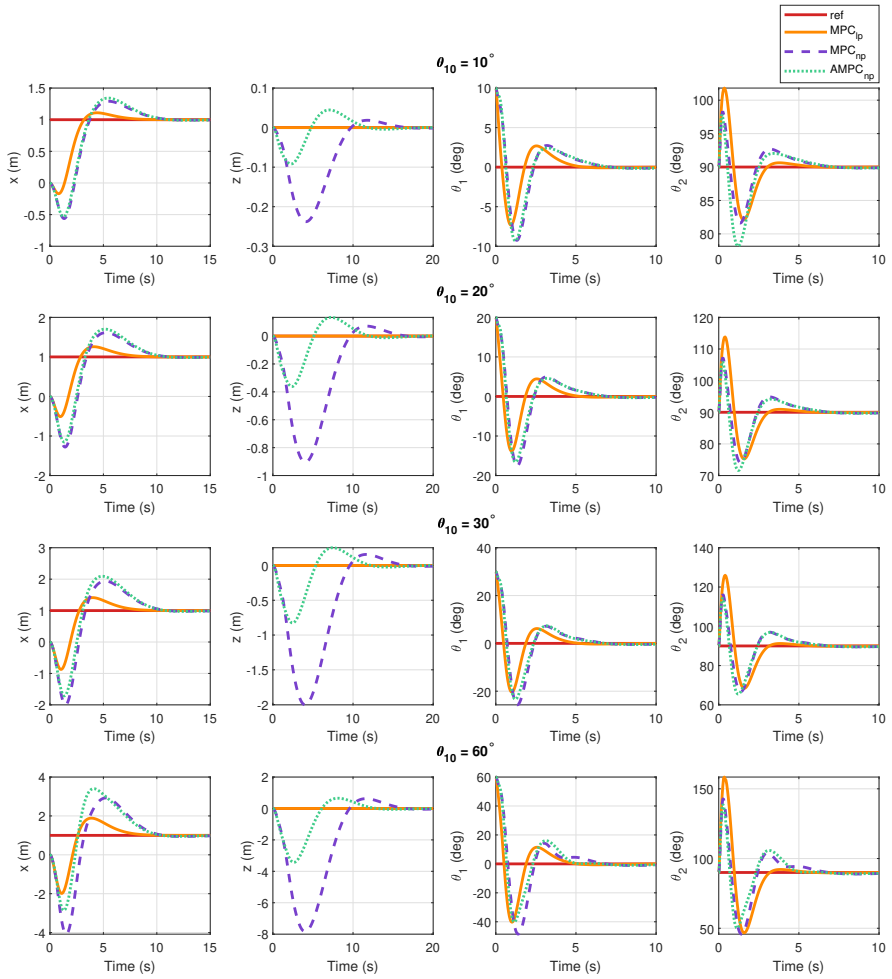

Figure 6.7: The state responses of the bi-rotor platform with appendage under different initial body angle with A-MPC.

We applied the same analysis to the proposed bi-rotor platform, as shown in Fig. 6.7. With A-MPC, the x and θ_1 responses are improved compared to MPC responses as the nonlinearity increases. Also, the body angle settles down rapidly with increased inertial redirection force applied by the appendage.

6.1.4 Motion Planning

In this section, we present the results obtained from the motion planning algorithm, MPC-Graph, implemented on a bi-rotor platform with an abdomen-like appendage.

We implemented the MPC-Graph algorithm based on the A-MPC control strategy, which improves the trajectory tracking performance of the proposed system. We implemented the SNG algorithm with the termination condition provided in (5.5). For a sufficient cover in the obstacle-free region, we implement termination condition with parameters $\alpha = 0.95$, $P_c = 0.9$ and these parameters give the number of consecutive failures as $m = 44$. Fig. 6.8 illustrates the generated nodes in the free space with unsampled regions.

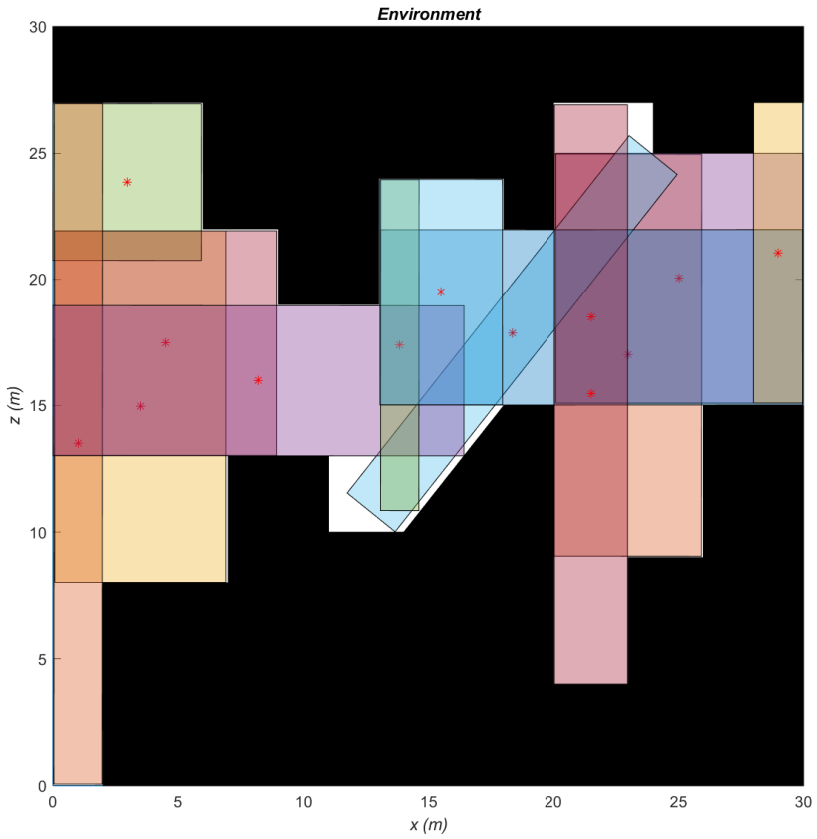

Figure 6.8: Illustration of the generated nodes. The red dots indicate the points q_{rand}, used for node generation. The white spaces are the regions that none of the nodes cover.

Then, we obtained the path from the start to the goal point, passing through the selected generated nodes. Dijkstra's search algorithm chooses the nodes with larger intersection areas to give vehicle flexibility for aggressive behavior during motion. The example of the nodes selected for the trajectory and the path executed by the aerial vehicle is shown in Fig. 6.9. When the robot passes through the next node, the reference point is updated as the center point of the next intersection area. The constraints are also updated according to the boundaries of the current node.

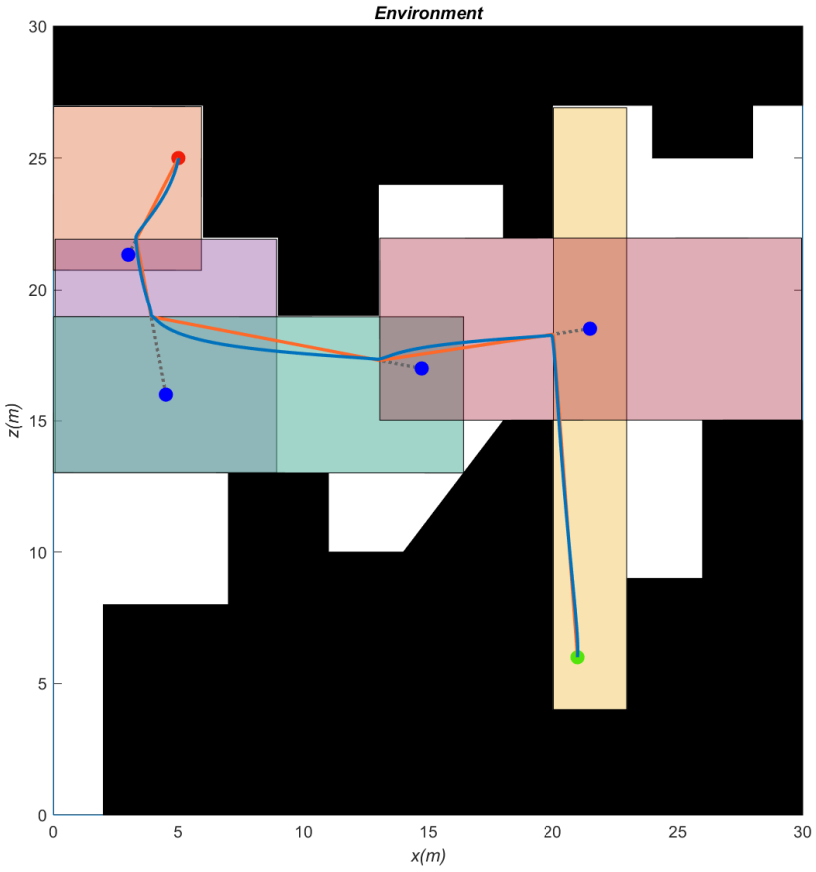

Figure 6.9: Representation of the trajectory generated by Dijkstra's search algorithm and the movement of the aerial vehicle. The red and green dots represent the start and goal points, respectively, whereas the blue dots represent the center of the intersection areas. The orange line shows the path generated from the algorithm, and the blue line indicates the motion of the aerial vehicle. Note that the reference signals (dashed gray lines) are updated when the vehicle enters the next node.

The result shows that the aerial vehicle follows the path without any input-output constraint violation in the absence of disturbance and noise. To analyze the algorithm's performance, we performed Monte-Carlo simulations in the presence of input noise, and the results are visualized in Fig. 6.10. Some of the tests ended with obstacle collision in the case that we have an initial condition with large body angles such as $\theta_1 = 60°$. In addition, the constraint violation occurred mainly in the first node, in which the aerial vehicle moved along x and z direction simultaneously with a disturbance coming from the initial body angle. On the other hand, based on most of the results, we can conclude that A-MPC performs effectively in the presence of the input noise.

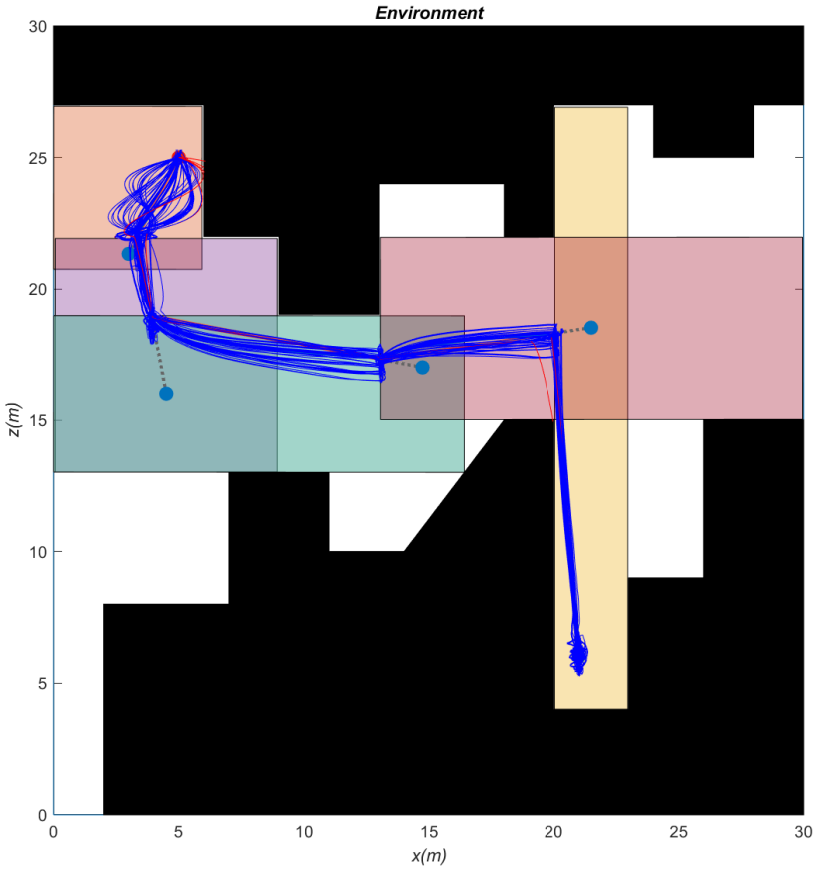

Figure 6.10: Results of the Monte-Carlo simulations with different initial conditions in the presence of input noise. The blue curves indicate the successful trajectories, whereas the red ones present the motion that ended with the obstacle collision.

6.2 3D Models with Quadrotor Platform

After completing our analysis in planar space, we now move on to 3D space with a conventional quadrotor and the one with an actively controlled 2-DOF abdomen-like appendage. Again, we start with LQR and then examine the conventional and adaptive MPC responses.

6.2.1 Linear Quadratic Regulator

As we did in the Section 6.1.1, we begin with the weighting matrices for the conventional quadrotor as $Q_{conv} = I_{12x12}$ and $R_{conv} = I_{4x4}$. The weighting matrices for the one with a 2-DOF appendage are as follows;

$$Q_{app} = \left[\begin{array}{cc|cc} \mathbf{I}_{6x6} & \mathbf{0}_{6x2} & \multicolumn{2}{c}{\multirow{2}{*}{$\mathbf{0}_{8x8}$}} \\ \mathbf{0}_{2x6} & \mathbf{0}_{2x2} & & \\ \hline \multicolumn{2}{c|}{\multirow{2}{*}{$\mathbf{0}_{8x8}$}} & \mathbf{I}_{6x6} & \mathbf{0}_{6x2} \\ & & \mathbf{0}_{2x6} & \mathbf{0}_{2x2} \end{array}\right], \qquad R_{app} = \left[\begin{array}{c|cc} \mathbf{I}_{4x4} & \multicolumn{2}{c}{\mathbf{0}_{4x2}} \\ \hline \multirow{2}{*}{$\mathbf{0}_{2x4}$} & 0.01 & 0 \\ & 0 & 0.01 \end{array}\right]. \tag{6.6}$$

For the conventional and the proposed quadrotor structure, we obtain state feedback gains K_{conv} and K_{app} with these weighting matrices as follows;

$$K_{conv} = \begin{bmatrix} 0 & 0 & -1 & 0 & 0 & 0 & 0 & 0 & -2.0976 & 0 & 0 & 0 \\ 0 & 1 & 0 & 5.6305 & 0 & 0 & 0 & 1.4656 & 0 & 1.0775 & 0 & 0 \\ -1 & 0 & 0 & 0 & 5.6305 & 0 & -1.4656 & 0 & 0 & 0 & 1.0775 & 0 \\ 0 & 0 & 0 & 0 & 0 & 1 & 0 & 0 & 0 & 0 & 0 & 1.0272 \end{bmatrix}, \tag{6.7}$$

$$K_{app} = \begin{bmatrix} 0 & 0 & -1 & 0 & 0 & 0 & 0 & 0 & 0 & 0 & -2.4290 & 0 & 0 & 0 & 0 & 0 \\ 0 & 0.7527 & 0 & 4.9702 & 0 & 0 & -0.2422 & 0 & 0 & 1.1394 & 0 & 1.0687 & 0 & 0 & -0.1753 & 0 \\ -0.7527 & 0 & 0 & 0 & 4.9702 & 0 & 0 & -0.2422 & -1.1394 & 0 & 0 & 0 & 1.0687 & 0 & 0 & -0.1753 \\ 0 & 0 & 0 & 0 & 0 & 1 & 0 & 0 & 0 & 0 & 0 & 0 & 0 & 1.0272 & 0 & 0 \\ 0 & 6.5839 & 0 & 0.5193 & 0 & 0 & -0.9098 & 0 & 0 & 6.4960 & 0 & -0.0101 & 0 & 0 & 0.5446 & 0 \\ -6.5839 & 0 & 0 & 0 & 0.5193 & 0 & 0 & -0.9098 & -6.4960 & 0 & 0 & 0 & -0.0101 & 0 & 0 & 0.5446 \end{bmatrix}. \tag{6.8}$$

Then, we apply these state feedback gains to linearized and nonlinear plant models with initial state $x_0 = 1$ and $\theta_0 = 30°$. Fig. 6.11 shows the response of the

states x, θ and θ_a. The left side represents the linearized model response, whereas the right represents the nonlinear model response. For both analyses, it can be seen that the appendage improves the pitch stabilization of the quadrotor, and the translational movement along the x axis makes less overshoot compared to the conventional one. In the nonlinear system response, the overshoot of the angle θ slightly increases compared to the linearized system. This outcome is related to the appendage angle change, which is smaller in the nonlinear system response.

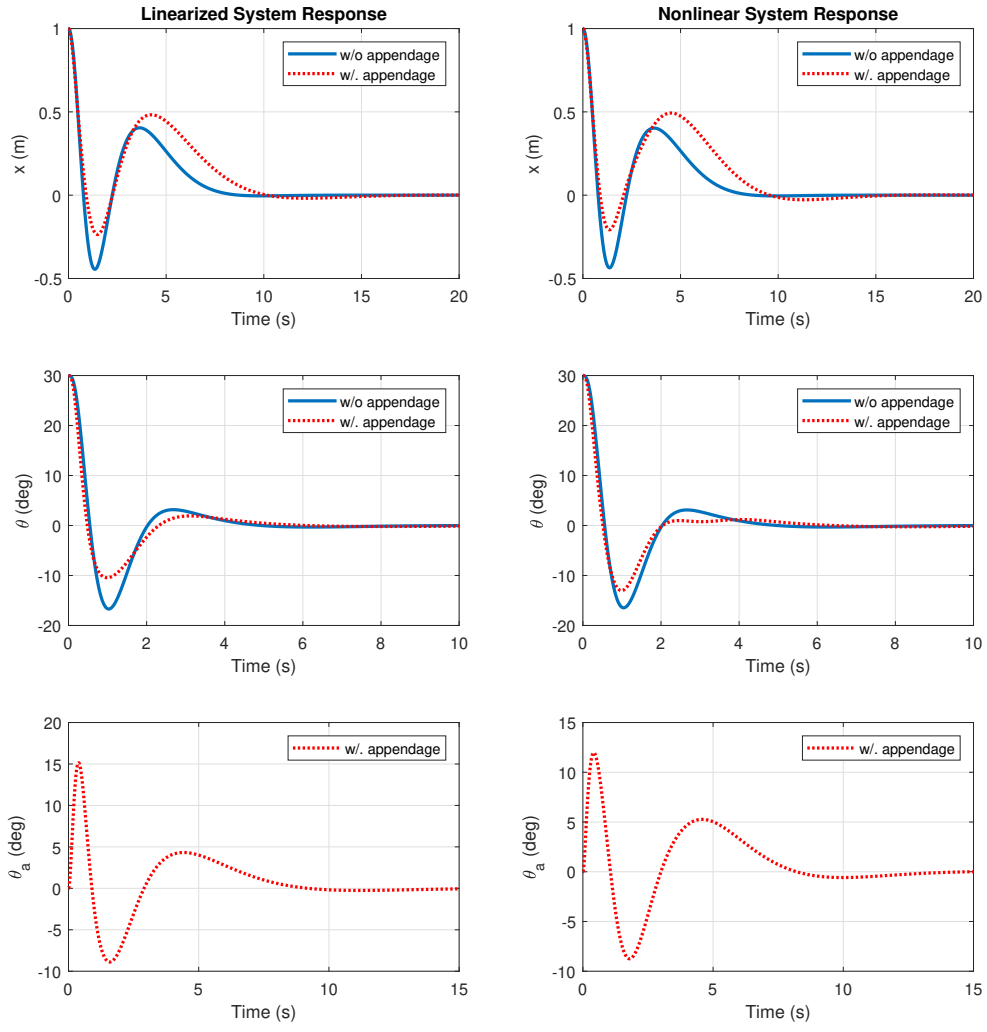

Figure 6.11: Comparison of the linearized system and nonlinear system response with initial state $x_0 = 1$ and $\theta_0 = 30°$

We also comprehensively analyzed different weighting parameters for the quadrotor platforms with/without an abdomen-like appendage. Table 6.5 compares the quadrotor platforms' responses regarding overshoot, settling time, steady-state error, and the average cost value. We investigated the step responses of the translational movements x, y and z with initial body angles, $\phi_0 = \theta_0 = 5°$. The results show that the appendage improves x and y response in settling time and decreases the average cost J. However, for position z, the conventional quadrotor reaches the desired value a bit quicker than the one with an appendage. Therefore, we obtain a slightly higher average cost for the z response of the proposed quadrotor system.

Table 6.5: Step response analysis for the position x, y, z of the quadrotor with/without abdomen-like appendage appendage

Q_{diag}	R_{diag}	$M_p(\%)$	$T_{sett}(s)$	$E_{ss}(\%)$	J
w/o appendage	**w/o appendage**	0, 0, 5.80	4.45, 4.27, 4.60	0, 0, 0	1.1272, 1.1805, 1.6729
$Q_{diag} = \{1, 1, 1, 1, 1, 1, 1, 1, 1, 1, 1, 1\}$	$R_{diag} = \{1, 1, 1, 1\}$				
w/. appendage	**w/. appendage**	0, 0, 2.11	4.16, 4.09, 5.55	0, 0, 0	1.0279, 1.0717, 1.8618
$Q_{diag} = \{1, 1, 1, 1, 1, 1, \mathbf{0}, \mathbf{0}, 1, 1, 1, 1, 1, 1, \mathbf{0}, \mathbf{0}\}$	$R_{diag} = \{1, 1, 1, 1, \mathbf{0.01}, \mathbf{0.01}\}$				
w/o appendage	**w/o appendage**	0, 0, 8.60	4.49, 4.28, 7.51	0, 0, 0	1.2114, 1.2537, 2.9245
$Q_{diag} = \{1, 1, 1, 1, 1, 1, 1, 1, 1, 1, 1, 1\}$	$R_{diag} = \{10, 10, 10, 10\}$				
w/. appendage	**w/. appendage**	0, 0, 3.52	4.17, 4.11, 8.98	0, 0, 0	1.1017, 1.1317, 3.2602
$Q_{diag} = \{1, 1, 1, 1, 1, 1, \mathbf{0}, \mathbf{0}, 1, 1, 1, 1, 1, 1, \mathbf{0}, \mathbf{0}\}$	$R_{diag} = \{10, 10, 10, 10, \mathbf{0.01}, \mathbf{0.01}\}$				
w/o appendage	**w/o appendage**	0, 0, 8.61	4.49, 4.28, 7.50	0, 0, 0	1.2203, 1.2350, 2.9216
$Q_{diag} = \{1, 1, 1, 1, 1, 1, 1, 1, 1, 1, 1, 1\}$	$R_{diag} = \{10, 10, 10, 10\}$				
w/. appendage	**w/. appendage**	0, 0, 3.51	4.43, 4.23, 8.99	0, 0, 0	1.2003, 1.2146, 3.2462
$Q_{diag} = \{1, 1, 1, 1, 1, 1, \mathbf{0}, \mathbf{0}, 1, 1, 1, 1, 1, 1, \mathbf{0}, \mathbf{0}\}$	$R_{diag} = \{9.975, 9.975, 9.975, 9.975, \mathbf{1}, \mathbf{1}\}$				
w/o appendage	**w/o appendage**	0, 0, 5.85	4.43, 4.27, 4.61	0, 0, 0	1.1488, 1.1681, 1.7078
$Q_{diag} = \{1, 1, 1, 1, 10, 1, 1, 1, 1, 1, 1, 1\}$	$R_{diag} = \{1, 1, 1, 1\}$				
w/. appendage	**w/. appendage**	0, 0, 2.11	4.37, 4.21, 5.56	0, 0, 0	1.1337, 1.1492, 1.8959
$Q_{diag} = \{1, 1, 1, 1, 10, 1, \mathbf{0}, \mathbf{0}, 1, 1, 1, 1, 1, 1, \mathbf{0}, \mathbf{0}\}$	$R_{diag} = \{1, 1, 1, 1, \mathbf{0.01}, \mathbf{0.01}\}$				
w/o appendage	**w/o appendage**	0, 0, 8.61	4.47, 4.28, 7.51	0, 0, 0	1.2503, 1.2526, 2.9159
$Q_{diag} = \{1, 1, 1, 1, 10, 1, 1, 1, 1, 1, 1, 1\}$	$R_{diag} = \{10, 10, 10, 10\}$				
w/. appendage	**w/. appendage**	0, 0, 3.52	4.18, 4.12, 8.99	0, 0, 0	1.1495, 1.1305, 3.2507
$Q_{diag} = \{1, 1, 1, 1, 10, 1, \mathbf{0}, \mathbf{0}, 1, 1, 1, 1, 1, 1, \mathbf{0}, \mathbf{0}\}$	$R_{diag} = \{10, 10, 10, 10, \mathbf{0.01}, \mathbf{0.01}\}$				
w/o appendage	**w/o appendage**	1.30, 0, 5.84	1.59, 4.27, 4.61	0, 0, 0	6.3465, 1.1060, 1.5364
$Q_{diag} = \{10, 1, 1, 1, 10, 1, 1, 1, 1, 1, 1, 1\}$	$R_{diag} = \{1, 1, 1, 1\}$				
w/. appendage	**w/. appendage**	2.10, 0, 2.11	1.30, 4.17, 5.57	0, 0, 0	5.6016, 1.0681, 1.7155
$Q_{diag} = \{10, 1, 1, 1, 10, 1, \mathbf{0.1}, \mathbf{0.1}, 1, 1, 1, 1, 1, 1, \mathbf{0.1}, \mathbf{0.1}\}$	$R_{diag} = \{1, 1, 1, 1, \mathbf{0.01}, \mathbf{0.01}\}$				
w/o appendage	**w/o appendage**	0, 1.28, 5.88	4.45, 1.54, 4.61	0, 0, 0	1.0339, 6.4652, 1.5607
$Q_{diag} = \{1, 10, 1, 10, 1, 1, 1, 1, 1, 1, 1, 1\}$	$R_{diag} = \{1, 1, 1, 1\}$				
w/. appendage	**w/. appendage**	0, 1.85, 2.11	4.32, 1.32, 5.57	0, 0, 0	1.0015, 5.6613, 1.7404
$Q_{diag} = \{1, 10, 1, 10, 1, 1, \mathbf{0.1}, \mathbf{0.1}, 1, 1, 1, 1, 1, 1, \mathbf{0.1}, \mathbf{0.1}\}$	$R_{diag} = \{1, 1, 1, 1, \mathbf{0.01}, \mathbf{0.01}\}$				
w/o appendage	**w/o appendage**	0, 0, 8.61	4.45, 4.26, 2.39	0, 0, 0	1.3091, 1.1443, 9.7141
$Q_{diag} = \{1, 1, 10, 1, 1, 1, 1, 1, 1, 1, 1, 1\}$	$R_{diag} = \{1, 1, 1, 1\}$				
w/. appendage	**w/. appendage**	0, 0, 3.52	4.32, 4.17, 2.87	0, 0, 0	1.2649, 1.1051, 10.8775
$Q_{diag} = \{1, 1, 10, 1, 1, 1, \mathbf{0.1}, \mathbf{0.1}, 1, 1, 1, 1, 1, 1, \mathbf{0.1}, \mathbf{0.1}\}$	$R_{diag} = \{1, 1, 1, 1, \mathbf{0.01}, \mathbf{0.01}\}$				

We also examine the effects of the weighting parameters for the states belonging to the appendage on the body angles. Fig. 6.12 presents the effect of the weighting parameter of θ_a on the quadrotor pitch angle, θ and itself. We give the initial condition to the system with $\theta = 15°$ and increase the weight of the appendage angle step by step to observe the body angle responses. The minimum weight value causes the higher appendage angle changes and results in less overshoot in the body angle response. When the weight parameter equals 1, the appendage angle changes its position by $2.5°$, and its produced force is almost negligible for the stabilization improvement. Therefore, we have almost the same body angle response when the quadrotor platform has no appendage.

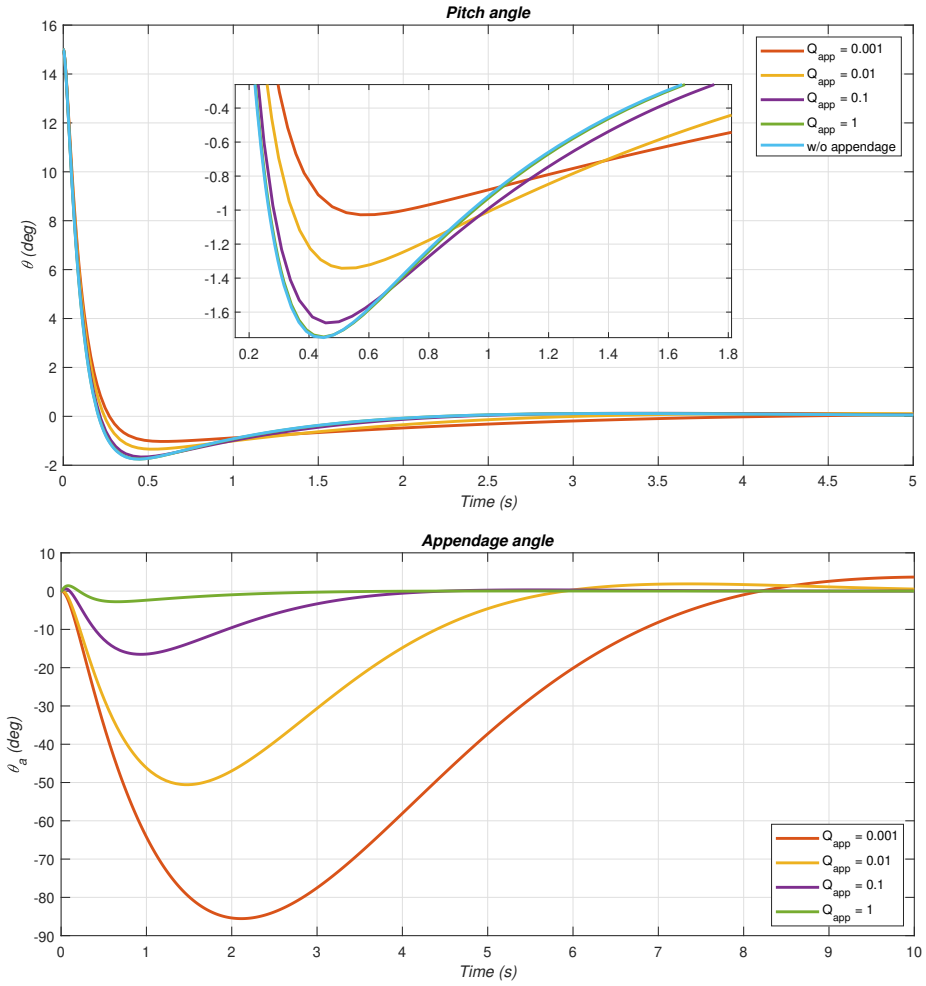

Figure 6.12: Responses of the quadrotor pitch angle, θ, and the appendage angle, θ_a, under different weight parameters of the appendage angle.

Table 6.6 also summarizes the results shown in Fig. 6.12 by emphasizing the results in terms of performance metrics.

Table 6.6: Effect of the weight parameter Q_{app} on the body angle θ

Weighting parameter for $\boldsymbol{\theta_a}$	Overshoot value of $\boldsymbol{\theta}$ (%)	Zero-crossing time of $\boldsymbol{\theta}$ (s)	Max value of $\boldsymbol{\theta_a}$ (deg)
$Q_{app} = 0.001$	6.85	2.94	85.51
$Q_{app} = 0.01$	8.93	2.32	50.55
$Q_{app} = 0.1$	11.10	1.85	16.51
$Q_{app} = 1$	11.63	1.77	2.77

6.2.2 Model Predictive Control

MPC is a well-suited controller strategy for a conventional quadrotor, an underactuated MIMO system with several constraints. Therefore, after LQR, we move to MPC to benefit from its ability to handle input-output constraints for conventional and the proposed quadrotor structure, as we did before for the planar bi-rotor platforms.

At this time, we have additional four states since the appendage has 2-DOF, represented by the angles ϕ_a, θ_a, and their derivatives. We choose the MPC parameters such that the stabilization of the body angles ϕ and θ have higher importance than other states. Table 6.7 gives the MPC parameters for the quadrotor structure with-/without appendage.

Table 6.7: Comparison of the MPC parameters for quadrotor with/without appendage

MPC Parameters	**w/o appendage**	**w/. appendage**
Sample Time, T_s	0.05 seconds	0.05 seconds
Prediction Horizon, N_p	35 steps	30 steps
Control Horizon, N_c	5 steps	4 steps
Input Constraints	**Min:** [0, -5, -5, -0.55] **Max:** [100, 5, 5, 0.55]	**Min:** [0, -5, -5, -0.55, -5, -5] **Max:** [100, 5, 5, 0.55, 5, 5]
Output Constraints	**Min:** [-30, -30, 0, $-\frac{\pi}{3}$, $-\frac{\pi}{3}$, $-\frac{\pi}{3}$] **Max:** [30, 30, 30, $\frac{\pi}{3}$, $\frac{\pi}{3}$, $\frac{\pi}{3}$]	**Min:** [-30, -30, 0, $-\frac{\pi}{3}$, $-\frac{\pi}{3}$, $-\frac{\pi}{3}$, $-\frac{\pi}{3}$, $-\frac{\pi}{3}$] **Max:** [30, 30, 30, $\frac{\pi}{3}$, $\frac{\pi}{3}$, $\frac{\pi}{3}$, $\frac{\pi}{3}$, $\frac{\pi}{3}$]
Input Weights	**Weight:** [1,1,1,1] **Rate Weight:** [0.1,0.1,0.1,0.1]	**Weight:** [1,1,1,1,0.01,0.01] **Rate Weight:** [0.1,0.1,0.1,0.1,0.01,0.01]
Output Weights	[1,1,1,10,10,1,1,1,1,1,1,1]	[1,1,1,10,10,1,0.1,0.1,1,1,1,1,1,1,0.1,0.1]

The state responses of the conventional and the proposed quadrotor can be seen in Fig. 6.13. For the analysis of the performances, we give step inputs to x and y positions with initial roll and pitch angle, $\phi_0 = \theta_0 = 10°$. These responses show that the proposed system performs better stabilization for the body attitude. However, the position x and z reach their steady-state values a bit slower than the conventional one due to appendage movement.

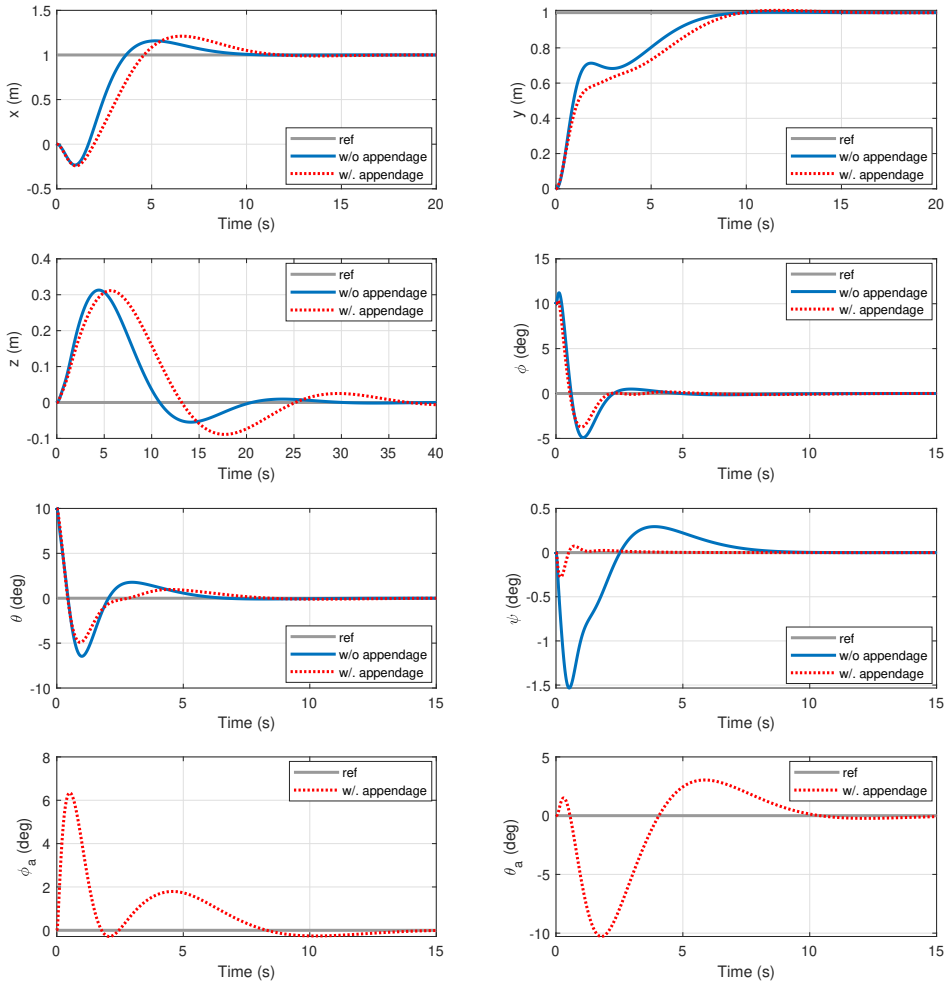

Figure 6.13: The conventional and proposed quadrotor response with MPC. The step input, $x_{ref} = y_{ref} = 1$, is given to the systems with initial body angles $\phi = \theta = 10°$.

The appendage movement is also shown in Fig. 6.13 with ϕ_a and θ_a responses. The change in the angle ϕ_a mainly improves the response of the translational movement

along the y direction and the body roll angle ϕ, whereas θ_a improves the tracking performance along the x axis and the body pitch angle θ. Since we increase the weights for ϕ and θ responses, the main improvement is related to these states, as the results presented. The inputs applied to the systems are also shown in Fig. 6.14.

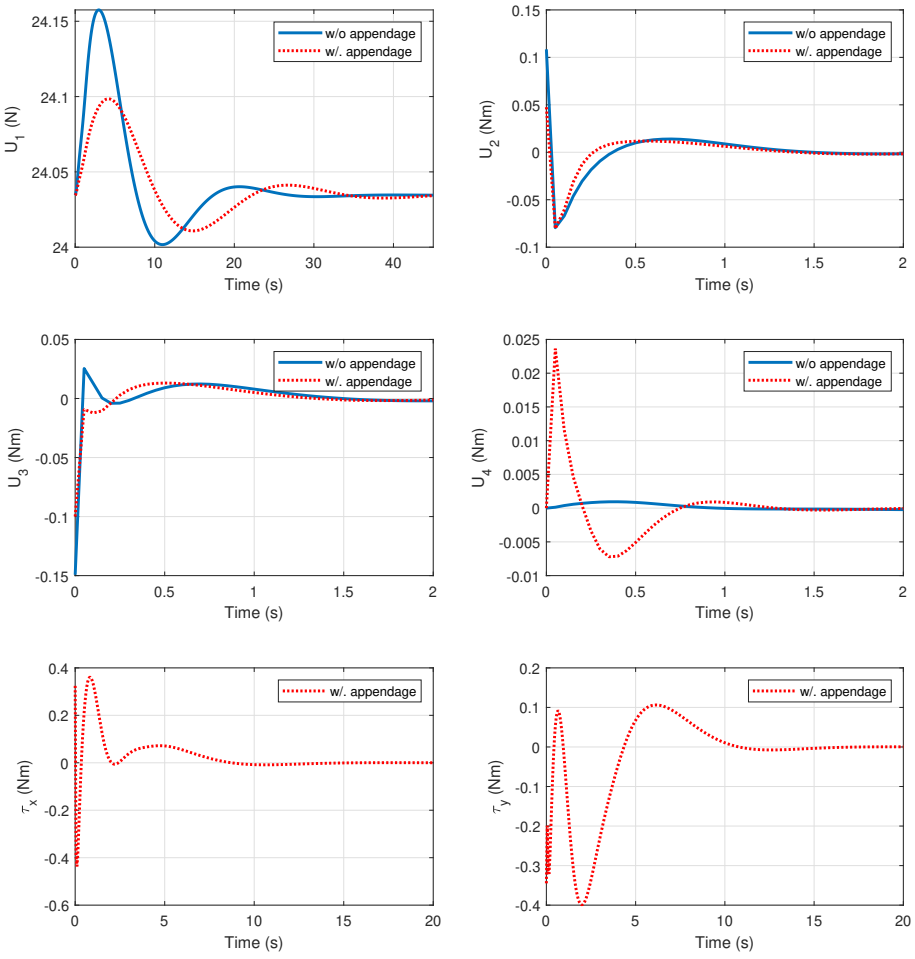

Figure 6.14: The conventional and proposed quadrotor input responses with MPC.

As we concluded in the analysis of the bi-rotor platforms, the propellers expend less effort with the help of appendage redirection. The only exception occurred in the yaw moment, U_4. However, the increased effort improves the yaw stabilization in the proposed system response.

6.2.3 Adaptive Model Predictive Control

This section presents the results of the A-MPC applied to the conventional and the proposed quadrotor platforms. MPC_{lp}, MPC_{np}, and $AMPC_{np}$ again refer to linearized plant model with conventional MPC, nonlinear plant model with conventional MPC, and nonlinear plant model with adaptive MPC, respectively. We first apply the A-MPC, which consists of the conventional MPC and linearized model update at each prediction step, to the conventional quadrotor. We give step input to the x position with different initial pitch angles, and the results are shown in Fig. 6.15.

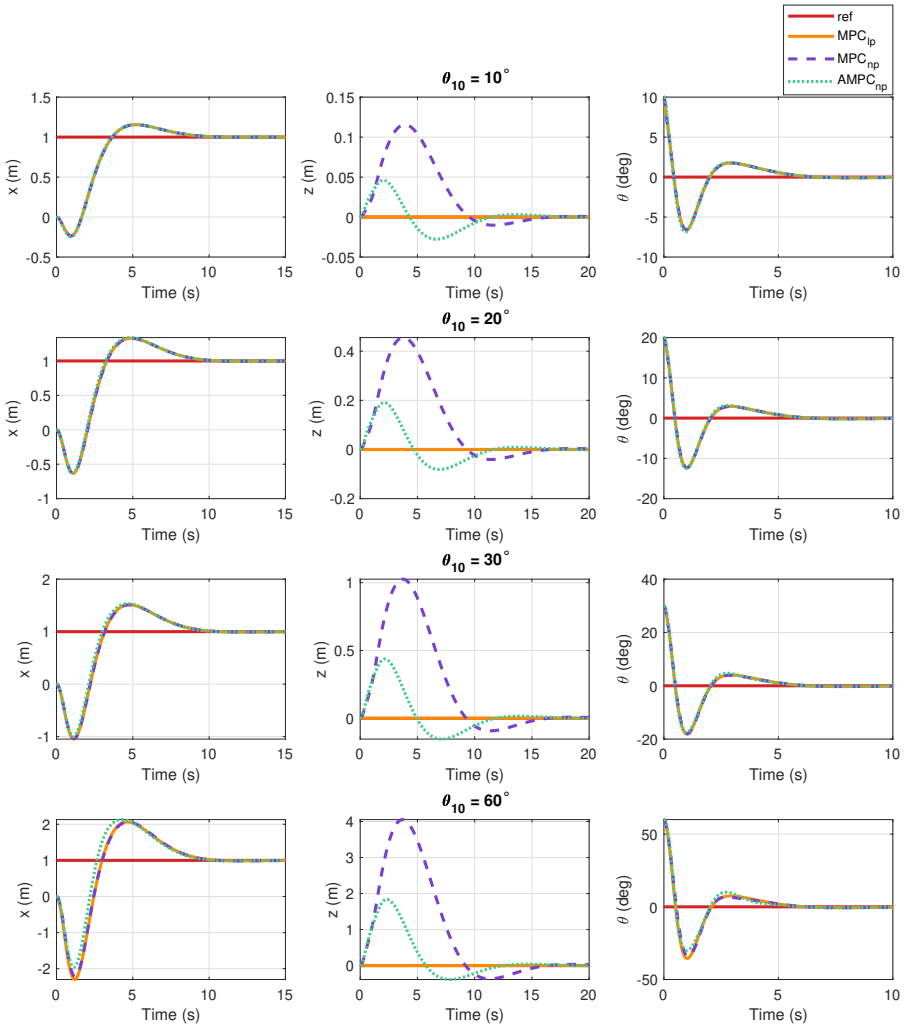

Figure 6.15: State response of the conventional quadrotor with A-MPC. The step input, $x_{ref} = 1$, is given to the system with different initial body pitch angles.

Then, we applied the same scenario to the quadrotor platform with an appendage, and we present the results in Fig. 6.16. For both systems, the results show that A-MPC improves the response of the position z significantly compared to conventional MPC. This outcome has arisen from losing the coupling effects between z and the other states if we keep using the model linearized only at the equilibrium point.

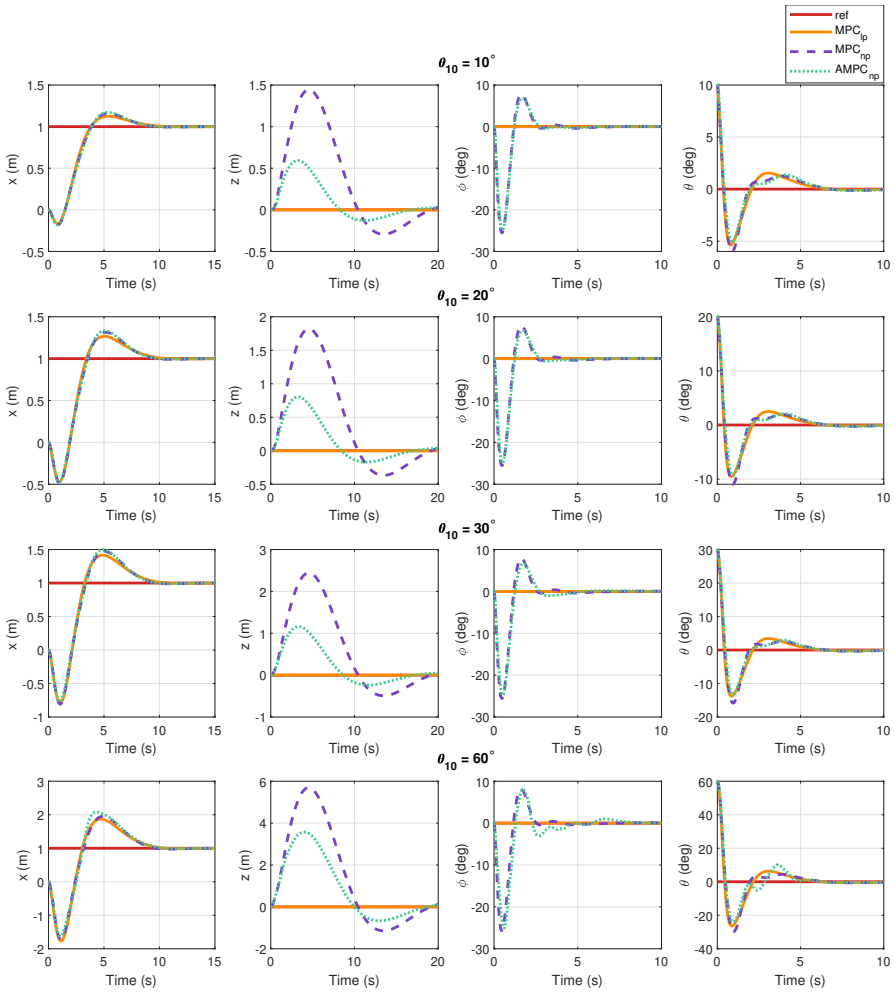

Figure 6.16: State response of the proposed quadrotor with A-MPC. The step input, $x_{ref} = 1$, is given to the system with different initial body pitch angles.

As we expected, the proposed system also performs better than the conventional one with A-MPC. The other states give better performance with A-MPC as we increase the nonlinearity by providing the initial condition to the pitch angle far from its equilibrium point.

CHAPTER 7

CONCLUSION AND FUTURE WORK

7.1 Conclusion

We proposed a bio-inspired aerial vehicle design with an actively controlled abdomen-like appendage in this work. The proposed system is inspired by flying insects that use abdomen reflexes to adjust their body orientation. We began our analysis in planar space, with a bi-rotor platform with and without the appendage. We derived the nonlinear mathematical models of the systems by using the Euler-Lagrange formulation. Then, we take our analysis to the next step by investigating the proposed morphology in 3D space with a quadrotor platform. We added 2-DOF abdomen-like appendage to the conventional quadrotor and constructed the bio-inspired aerial vehicle structure.

Towards analyzing the effect of the actively controlled abdomen-like appendage, we designed an LQR controller for conventional and proposed systems and compared their responses considering performance criteria such as settling time, overshoot, steady-state error, and average cost value. We kept the weighting parameters of the additional states smaller as much as possible to make a fair comparison. The results showed that the appendage improves the systems' performance and decreases the average cost.

In the next step, since the systems have several constraints, such as rotor speed limits, mechanical angular limitations, and rate of change of the inputs, we designed MPC, which sufficiently deals with input-output constraints. We went one step further by designing A-MPC for the highly nonlinear proposed systems. Comparing these controllers shows that MPC gives optimum results by considering input-output constraints compared to the LQR controller. The A-MPC performs best since it deals

with nonlinearities based on linearization at each prediction step.

As a final step of the study, we implemented a recently reported motion planning algorithm, MPC-Graph, in a planar space. The algorithm first generates sampling-based connected rectangular regions to represent free space in the environment. It calculates the cost function for moving one rectangle to another, considering the Euclidian distance between the center of the corresponding node and the intersection area. After calculating the cost function, Dijkstra's algorithm finds the optimum path from the start to the goal point. Then, designed MPCs navigate the aerial vehicle to the goal by passing through the predefined nodes. MPC updates the x and y position constraints with the corresponding rectangular boundaries during each rectangular region. Therefore, the vehicle stays in the rectangles that are defined in the free space during its movements. We analyzed the algorithm performance by applying input disturbances to the system and examined the constraint violations. We performed Monte Carlo simulations under different initial conditions. For higher initial body angles, the motion planning algorithm sometimes fails in the presence of input noise. Overall, we can conclude that the MPC-Graph algorithm handles the disturbances with an A-MPC based feedback motion policy.

To sum up, the main results of this study can be summarized as follows;

- The appendage makes propellers use less thrust force to accomplish the control tasks.
- Although we use additional control effort for the actively controlled abdomen-like appendage, the average LQR cost is still lower than the conventional aerial vehicles.
- The advantages of the appendage clearly appear when we have a wider appendage angle range and larger maximum torque limits as constraints.
- The worst case of the proposed system with hard torque constraint still gives better/equal performance with the conventional aerial vehicle.
- The advantage of the appendage can be used in industrial applications in which body stabilization is critical such as film-making, since the body angles of the

proposed system change less than the conventional one during horizontal movement.

- Model predictive control performs better than the constrained LQR when we have several constraints for the states of the system.
- A-MPC handles nonlinearities by linearizing the plant model at each prediction step. Thus, the performance of the controller increases compared to the conventional MPC.
- The final and essential point is that the bio-inspired aerial vehicle with an actively controlled abdomen-like appendage can be preferred for performance improvement, although it increases the mechanical complexity of the system.

7.2 Future Work

In this study, we analyzed the proposed structure in a simulation environment. Since the real-world implementation cost is high, we decided to perform the system analysis in simulations as a first step. In the future, we plan to test the proposed structure with a physical setup experimentally.

In the derivations of the quadrotor models, we simplified the nonlinear model with assumptions such as neglecting the Earth rate and aerodynamic effects because we want to emphasize the impact of the abdomen-like appendage on the stability performance of the system. Also, for simplicity, we considered the abdomen-like appendage as a 2-DOF point mass pendulum. It can be modeled as appendage inertia with a precisely defined center of mass. Therefore, we can advance the mathematical model by considering these improvements.

Furthermore, we only tested the motion planning algorithm, MPC-Graph, in a planar environment. We can expand the algorithm to a 3D space with 3D convex polytopes instead of planar obstacles to examine the algorithm's performance.

REFERENCES

[1] L. da Vinci, "Codex "on the flight of birds" 1505," *Leonardo Da Vinci: Turin*, vol. 17, p. 1505, 2013.

[2] B. Tobalske, "Hovering and intermittent flight in birds," *Bioinspiration & Biomimetics*, vol. 5, p. 045004, 12 2010.

[3] J. Camhi, "Yaw-correcting postural changes in locusts," *Journal of Experimental Biology*, vol. 52, no. 3, pp. 519–531, 1970.

[4] J. Camhi, "Sensory control of abdomen posture in flying locusts," *Journal of Experimental Biology*, vol. 52, 06 1970.

[5] M. GEWECKE and J. PHILIPPEN, "Control of the horizontal flight-course by air-current sense organs in locusta migratoria," *Physiological Entomology*, vol. 3, no. 1, pp. 43–52, 1978.

[6] A. BAADER, "The Posture of the Abdomen during Locust Flight: Regulation by Steering and Ventilatory Interneurones," *Journal of Experimental Biology*, vol. 151, pp. 109–131, 07 1990.

[7] J. M. Zanker, "How does lateral abdomen deflection contribute to flight control of drosophila melanogaster?," *Journal of Comparative Physiology A*, vol. 162, no. 5, pp. 581–588, 1988.

[8] M. Frye, "Effects of stretch receptor ablation on the optomotor control of lift in the hawkmoth manduca sexta," *The Journal of Experimental Biology*, vol. 204, pp. 3683–91, 12 2001.

[9] T. L. Hedrick and T. L. Daniel, "Flight control in the hawkmoth Manduca sexta: The inverse problem of hovering," *Journal of Experimental Biology*, vol. 209, pp. 3114–3130, 08 2006.

[10] J. P. Dyhr, K. A. Morgansen, T. L. Daniel, and N. J. Cowan, "Flexible strategies for flight control: An active role for the abdomen," *Journal of Experimental Biology*, vol. 216, pp. 1523–1536, May 2013.

[11] A. Demir, M. Ankarali, J. Dyhr, K. Morgansen, T. Daniel, and N. Cowan, "Inertial redirection of thrust forces for flight stabilization," 09 2012.

[12] H. Ugurlu, S. Kalkan, and A. Saranli, "Reinforcement learning versus conventional control for controlling a planar bi-rotor platform with tail appendage," *Journal of Intelligent & Robotic Systems*, vol. 102, 08 2021.

[13] G. Hoffmann, S. Waslander, and C. Tomlin, "Quadrotor helicopter trajectory tracking control," *Proceedings of the AIAA Guidance, Navigation, and Control Conference*, 08 2008.

[14] S. Bouabdallah, A. Noth, and R. Y. Siegwart, "PID vs LQ control techniques applied to an indoor micro quadrotor," *2004 IEEE/RSJ International Conference on Intelligent Robots and Systems (IROS) (IEEE Cat. No.04CH37566)*, vol. 3, pp. 2451–2456 vol.3, 2004.

[15] J. Li and Y. Li, "Dynamic analysis and PID control for a quadrotor," in *2011 IEEE International Conference on Mechatronics and Automation*, pp. 573–578, 2011.

[16] S. Bouabdallah, "Design and control of quadrotors with application to autonomous flying," 2007.

[17] H. Kim, D. Shim, and S. Sastry, "Nonlinear model predictive tracking control for rotorcraft-based unmanned aerial vehicles," in *Proceedings of the 2002 American Control Conference (IEEE Cat. No.CH37301)*, vol. 5, pp. 3576–3581 vol.5, 2002.

[18] K. Shimada and T. Nishida, "Particle filter-model predictive control of quadcopters," 10 2014.

[19] P. Chikasha and C. Dube, "Adaptive model predictive control of a quadrotor," *IFAC-PapersOnLine*, vol. 50, pp. 157–162, 12 2017.

[20] M. Abdolhosseini, Y. Zhang, and C. Rabbath, "An efficient model predictive control scheme for an unmanned quadrotor helicopter," *Journal of Intelligent & Robotic Systems*, vol. 70, 04 2013.

[21] K. Alexis, C. Papachristos, R. Siegwart, and A. Tzes, "Robust model predictive flight control of unmanned rotorcrafts," *Journal of Intelligent & Robotic Systems*, vol. 81, 06 2015.

[22] P. Outeiro, C. Cardeira, and P. Oliveira, "Multiple-model adaptive control architecture for a quadrotor with constant unknown mass and inertia," *Aerospace Science and Technology*, vol. 117, p. 106899, 2021.

[23] S. Notter, A. Heckmann, A. Mcfadyen, and L. Gonzalez, "Modelling, simulation and flight test of a model predictive controlled multirotor with heavy slung load," vol. 49, 12 2016.

[24] Z. Cai, S. Zhang, and X. Jing, "Model predictive controller for quadcopter trajectory tracking based on feedback linearization," *IEEE Access*, vol. 9, pp. 162909–162918, 2021.

[25] K. Pereida and A. P. Schoellig, "Adaptive model predictive control for high-accuracy trajectory tracking in changing conditions," in *2018 IEEE/RSJ International Conference on Intelligent Robots and Systems (IROS)*, pp. 7831–7837, 2018.

[26] M. Tanaskovic, L. Fagiano, and V. Gligorovski, "Adaptive model predictive control for linear time varying MIMO systems," *Automatica*, vol. 105, pp. 237–245, 2019.

[27] M. Lorenzen, F. Allgöwer, and M. Cannon, "Adaptive model predictive control with robust constraint satisfaction," *IFAC-PapersOnLine*, vol. 50, no. 1, pp. 3313–3318, 2017. 20th IFAC World Congress.

[28] C. Goerzen, Z. Kong, and B. Mettler, "A survey of motion planning algorithms from the perspective of autonomous UAV guidance," *Journal of Intelligent and Robotic Systems*, vol. 57, pp. 65–100, 11 2010.

[29] D. Ferguson, M. Likhachev, and A. Stentz, "A guide to heuristic-based path planning," 01 2005.

[30] K. Danancier, D. Ruvio, I. Sung, and P. Nielsen, "Comparison of path planning algorithms for an unmanned aerial vehicle deployment under threats," *IFAC-PapersOnLine*, vol. 52, no. 13, pp. 1978–1983, 2019. 9th IFAC Conference on Manufacturing Modelling, Management and Control MIM 2019.

[31] F. H. Tseng, T. T. Liang, C. H. Lee, L. D. Chou, and H. C. Chao, "A star search algorithm for civil UAV path planning with 3G communication," in *2014 Tenth International Conference on Intelligent Information Hiding and Multimedia Signal Processing*, pp. 942–945, 2014.

[32] L. Yang and S. LaValle, "The sampling-based neighborhood graph: An approach to computing and executing feedback motion strategies," *Robotics and Automation, IEEE Transactions on*, vol. 20, pp. 419 – 432, 07 2004.

[33] O. K. Karagoz, S. Atasoy, and M. M. Ankarali, "MPC-graph: Feedback motion planning using sparse sampling based neighborhood graph," in *2020 IEEE/RSJ International Conference on Intelligent Robots and Systems (IROS)*, pp. 6797–6802, 2020.

[34] S. Atasoy, "MPC-graph: Nonlinear feedback motion planning using sparse sampling based neighborhood graph," Master's thesis, Middle East Technical University, 2022.

[35] H. Khalil, *Nonlinear Systems*. Pearson Education, Prentice Hall, 2002.

[36] The Mathworks, Inc., Natick, Massachusetts, *MATLAB version 9.7.0.1471314 (R2019b) Update 7*, 2019.

[37] M. Spong, S. Hutchinson, and M. Vidyasagar, *Robot Modeling and Control*. Wiley select coursepack, Wiley, 2005.

[38] S. H. Strogatz, *Nonlinear Dynamics and Chaos: With Applications to Physics, Biology, Chemistry and Engineering*. Westview Press, 2000.

[39] L. Wang, *Model Predictive Control System Design and Implementation Using MATLAB*. Springer Publishing Company, Incorporated, 1st ed., 2009.

[40] A. W. ORDYS and D. W. CLARKE, "A state-space description for GPC controllers," *International Journal of Systems Science*, vol. 24, no. 9, pp. 1727–1744, 1993.

[41] J. Rawlings, "Tutorial overview of model predictive control," *IEEE Control Systems Magazine*, vol. 20, no. 3, pp. 38–52, 2000.

[42] S. Skogestad and I. Postlethwaite, *Multivariable Feedback Control: Analysis and Design*. Hoboken, NJ, USA: John Wiley & Sons, Inc., 2005.

[43] S. Tang and V. Kumar, "Autonomous flying," *Annual Review of Control, Robotics, and Autonomous Systems*, vol. 1, 05 2018.

[44] G. F. Powell, *Feedback Control Of Dynamic Systems, Global Edition.* Pearson Education Limited, 2019.

[45] J. Richalet, A. Rault, J. Testud, and J. Papon, "Model algorithmic control of industrial processes," *IFAC Proceedings Volumes*, vol. 10, no. 16, pp. 103–120, 1977. Preprints of the 5th IFAC/IFIP International Conference on Digital Computer Applications to Process Control, The Hague, The Netherlands, 14-17 June, 1977.

[46] E. DIJKSTRA, "A note on two problems in connexion with graphs.," *Numerische Mathematik*, vol. 1, pp. 269–271, 1959.

APPENDIX A

ANALYTIC LINEARIZATION EQUATIONS OF THE SYSTEMS

In this section, the Jacobian linearization of the systems is derived analytically. First, we begin with bi-rotor platforms and then we move to the quadrotor platforms used in this study.

A.1 Conventional Bi-rotor Platform

The conventional bi-rotor platform has the A and B matrix, defined with the current states and inputs, as follows;

$$A = \begin{bmatrix} 0 & 0 & 0 & 1 & 0 & 0 \\ 0 & 0 & 0 & 0 & 1 & 0 \\ 0 & 0 & 0 & 0 & 0 & 1 \\ 0 & 0 & \boldsymbol{A_{4,3}} & 0 & 0 & 0 \\ 0 & 0 & \boldsymbol{A_{5,3}} & 0 & 0 & 0 \\ 0 & 0 & 0 & 0 & 0 & 0 \end{bmatrix}, \qquad B = \begin{bmatrix} 0 & 0 \\ 0 & 0 \\ 0 & 0 \\ \boldsymbol{B_{4,1}} & \boldsymbol{B_{4,2}} \\ \boldsymbol{B_{5,1}} & \boldsymbol{B_{5,2}} \\ \boldsymbol{B_{6,1}} & \boldsymbol{B_{6,2}} \end{bmatrix}, \tag{A.1}$$

where

$$\boldsymbol{A_{4,3}} = -\frac{(F_1 + F_2)\mathbf{c}_{\theta_1}}{M}, \qquad \boldsymbol{A_{5,3}} = -\frac{(F_1 + F_2)\mathbf{s}_{\theta_1}}{M}, \tag{A.2}$$

$$\boldsymbol{B_{4,1}} = -\frac{\mathbf{s}_{\theta_1}}{M}, \qquad \boldsymbol{B_{4,2}} = -\frac{\mathbf{s}_{\theta_1}}{M}, \tag{A.3}$$

$$\boldsymbol{B_{5,1}} = \frac{\mathbf{c}_{\theta_1}}{M}, \qquad \boldsymbol{B_{5,2}} = \frac{\mathbf{c}_{\theta_1}}{M}, \tag{A.4}$$

$$\boldsymbol{B_{6,1}} = -\frac{L}{2I_M}, \qquad \boldsymbol{B_{6,2}} = \frac{L}{2I_M}. \tag{A.5}$$

A.2 Proposed Bi-rotor Platform with Abdomen-Like Appendage

The state transition matrix A of the bi-rotor platform with abdomen-like appendage is as follows;

$$A = \begin{bmatrix} 0 & 0 & 0 & 0 & 1 & 0 & 0 & 0 \\ 0 & 0 & 0 & 0 & 0 & 1 & 0 & 0 \\ 0 & 0 & 0 & 0 & 0 & 0 & 1 & 0 \\ 0 & 0 & 0 & 0 & 0 & 0 & 0 & 1 \\ 0 & 0 & \boldsymbol{A_{5,3}} & \boldsymbol{A_{5,4}} & 0 & 0 & \boldsymbol{A_{5,7}} & \boldsymbol{A_{5,8}} \\ 0 & 0 & \boldsymbol{A_{6,3}} & \boldsymbol{A_{6,4}} & 0 & 0 & \boldsymbol{A_{6,7}} & \boldsymbol{A_{6,8}} \\ 0 & 0 & \boldsymbol{A_{7,3}} & \boldsymbol{A_{7,4}} & 0 & 0 & \boldsymbol{A_{7,7}} & \boldsymbol{A_{7,8}} \\ 0 & 0 & \boldsymbol{A_{8,3}} & \boldsymbol{A_{8,4}} & 0 & 0 & \boldsymbol{A_{8,7}} & \boldsymbol{A_{8,8}} \end{bmatrix}, \tag{A.6}$$

where

$$\begin{aligned}
\boldsymbol{A_{5,3}} = &-\frac{1}{2M\ell\sigma_7}\Big[4Mh^2m\tau\mathbf{c}_{(2\theta_1-\theta_2)} - I_M\ell m\left(\sigma_2 - \mathbf{c}_{\theta_1}\right)\sigma_5 + I_M M\ell\mathbf{c}_{\theta_1}\sigma_4 + LMh\ell m\left(\sigma_1 + \mathbf{s}_{\theta_1}\right) \\
&+ Mh^2\ell m\left(F_1 + F_2\right)\left(3\mathbf{c}_{\sigma_3} - \sigma_2 + 2\mathbf{c}_{\theta_1}\right) - 4I_M M\dot{\theta}_1^2 h\ell m\left(\sigma_2 + \mathbf{c}_{\theta_1}\right)\Big] - \frac{1}{\ell\sigma_7^2}\Big[h^2 m\mathbf{s}_{\sigma_8}\Big(16I_M\tau\mathbf{s}_{\theta_2}(M+m) \\
&+ 2Mh^2m\tau(\mathbf{s}_{(2\theta_1-\theta_2)} + \mathbf{s}_{\theta_2}) - I_M\ell m\sigma_5(\sigma_1 - \mathbf{s}_{\theta_1}) + I_M M\ell\mathbf{s}_{\theta_1}\sigma_4 + 16I_M M\dot{\theta}_2^2\ell^2 m\mathbf{c}_{\theta_2} \\
&+ Mh^2\ell m(F_1+F_2)(\mathbf{s}_{\sigma_3} - \sigma_1 + 2\mathbf{s}_{\theta_1}) - LMhlm(\sigma_1 + \mathbf{c}_{\theta_1})\sigma_6 - 4I_M M\dot{\theta}_1^2 h\ell m(\sigma_1 + \mathbf{s}_{\theta_1})\Big)\Big],
\end{aligned} \tag{A.7}$$

$$\begin{aligned}
\boldsymbol{A_{5,4}} = &\frac{1}{\ell\sigma_7^2}\Big[h^2 m\mathbf{s}_{\sigma_8}\Big(16I_M\tau\mathbf{s}_{\theta_2}(M+m) + 2Mh^2m\tau(\mathbf{s}_{(2\theta_1-\theta_2)} + \mathbf{s}_{\theta_2}) - I_M\ell m8(F_1+F_2)(\sigma_1 - \mathbf{s}_{\theta_1}) \\
&+ I_M M\ell\mathbf{s}_{\theta_1}\sigma_4 + 16I_M M\dot{\theta}_2^2\ell^2 m\mathbf{c}_{\theta_2} + Mh^2\ell m(F_1+F_2)(\mathbf{s}_{\sigma_3} - \sigma_1 + 2\mathbf{s}_{\theta_1}) - LMh\ell m(\sigma_1 + \mathbf{c}_{\theta_1})(2F_1 - 2F_2) \\
&- 4I_M M\dot{\theta}_1^2 h\ell m(\sigma_1 + \mathbf{s}_{\theta_1})\Big)\Big] - \frac{1}{2M\ell\sigma_7}\Big[8I_M Mm\sigma_2\dot{\theta}_1^2 h\ell - 16I_M Mm\mathbf{s}_{\theta_2}\dot{\theta}_2^2\ell^2 - 2Mm\tau(\mathbf{c}_{(2\theta_1-\theta_2)} - \mathbf{c}_{\theta_2})h^2, \\
&+ Mm(\sigma_2 - \mathbf{c}_{\sigma_3})(2F_1 + 2F_2)h^2\ell - 4LMm\sigma_1(F_1 - F_2)h\ell + I_M m\sigma_2\sigma_4\ell + 16I_M\tau\mathbf{c}_{\theta_2}(M+m)\Big]
\end{aligned} \tag{A.8}$$

$$\boldsymbol{A_{5,7}} = \frac{4I_M\dot{\theta}_1 hm(\mathbf{s}_{(\theta_1-2\theta_2)} + \mathbf{s}_{\theta_1})}{\sigma_7}, \tag{A.9}$$

$$\boldsymbol{A_{5,8}} = -\frac{16I_M\dot{\theta}_2\ell m\mathbf{c}_{\theta_2}}{\sigma_7}, \tag{A.10}$$

$$\begin{aligned}
\boldsymbol{A_{6,3}} = &\frac{1}{\ell\sigma_7^2}\Big[h^2 m\mathbf{s}_{\sigma_8}\Big(16I_M(M+m)(\tau\mathbf{c}_{\theta_2} - Mg\ell) + I_M\ell m(\sigma_2 + \mathbf{c}_{\theta_1})\sigma_5 + 2Mh^2m(\tau\mathbf{c}_{(2\theta_1-\theta_2)} + \tau\mathbf{c}_{\theta_2} - Mg\ell) \\
&+ I_M M\ell\mathbf{c}_{\theta_1}\sigma_4 - 2M^2gh^2\ell m\mathbf{c}_{\sigma_8} + Mh^2\ell m(F_1+F_2)(\sigma_2 + \mathbf{c}_{\sigma_3} + 2\mathbf{c}_{\theta_1}) - 16I_M M\dot{\theta}_2^2\ell^2 m\mathbf{s}_{\theta_2} \\
&+ 4I_M M\dot{\theta}_1^2 h\ell m(\sigma_2 - \mathbf{c}_{\theta_1}) - LMh\ell m\sigma_6(\sigma_1 - \mathbf{s}_{\theta_1})\Big)\Big] - \frac{1}{2M\ell\sigma_7}\Big[I_M\ell m(\sigma_1 + \mathbf{s}_{\theta_1})\sigma_5 + 4Mh^2m\tau\mathbf{s}_{(2\theta_1-\theta_2)} \\
&+ I_M M\ell\mathbf{s}_{\theta_1}\sigma_4 - 4M^2gh^2\ell m\mathbf{s}_{\sigma_8} + Mh^2\ell m(F_1+F_2)(\sigma_1 + 3\mathbf{s}_{\sigma_3} + 2\mathbf{s}_{\theta_1}) + LMh\ell m(\sigma_2 - \mathbf{c}_{\theta_1})\sigma_6 \\
&+ 4I_M M\dot{\theta}_1^2 h\ell m(\sigma_1 - \mathbf{s}_{\theta_1})\Big],
\end{aligned} \tag{A.11}$$

$$\boldsymbol{A_{6,4}} = \frac{1}{2M\ell\sigma_7}\Bigg[I_M\ell m\sigma_1\sigma_4 - 8I_M M\ell m(2\dot{\theta}_2^2\ell\mathbf{c}_{\theta_2} - \dot{\theta}_1^2 h\sigma_1) - 16I_M\tau\mathbf{s}_{\theta_2}(M+m) + 2Mh^2m\tau(\mathbf{s}_{(2\theta_1-\theta_2)} - \mathbf{s}_{\theta_2})$$
$$- 4M^2gh^2\ell m\mathbf{s}_{\sigma_8} + Mh^2\ell m2(F_1+F_2)(\sigma_1+\mathbf{s}_{\sigma_3}) + LMh\ell m\sigma_2 4(F_1-F_2)\Bigg] - \frac{1}{\ell\sigma_7^2}\Bigg[h^2m\mathbf{s}_{\sigma_8}\Big(I_M M\ell\mathbf{c}_{\theta_1}\sigma_4$$
$$+ Mh^2\ell m(F_1+F_2)(\sigma_2 + 3\mathbf{c}_{\sigma_3} + 2\mathbf{c}_{\theta_1}) + 2Mh^2m(\tau(\mathbf{c}_{(2\theta_1-\theta_2)} + \mathbf{c}_{\theta_2}) - Mg\ell) + I_M\ell m(\sigma_2+\mathbf{c}_{\theta_1})8(F_1+F_2)$$
$$+ 16I_M(M+m)(\tau\mathbf{c}_{\theta_2} - Mg\ell) - 2M^2gh^2\ell m\mathbf{c}_{\sigma_8} - 16I_M M\dot{\theta}_2^2\ell^2 m\mathbf{s}_{\theta_2} - 2LMh\ell m(F_1-F_2)(\sigma_1 - \mathbf{s}_{\theta_1})$$
$$+ 4I_M M\dot{\theta}_1^2 h\ell m(\sigma_2 - \mathbf{c}_{\theta_1})\Big)\Bigg], \tag{A.12}$$

$$\boldsymbol{A_{6,7}} = \frac{4I_M\dot{\theta}_1 hm(\mathbf{c}_{(\theta_1-2\theta_2)} - \mathbf{c}_{\theta_1})}{\sigma_7}, \tag{A.13}$$

$$\boldsymbol{A_{6,8}} = -\frac{16I_M\dot{\theta}_2\ell m\mathbf{s}_{\theta_2}}{\sigma_7}, \tag{A.14}$$

$$\boldsymbol{A_{7,3}} = \frac{h}{\ell\sigma_7}\Bigg[4\tau\mathbf{c}_{(\theta_1-\theta_2)}(M+m) + \ell m\mathbf{c}_{\sigma_8}4(F_1+F_2) + 2M\ell m(h\mathbf{c}_{\sigma_8}\dot{\theta}_1^2 + 2\ell\mathbf{s}_{(\theta_1-\theta_2)}\dot{\theta}_2^2)\Bigg] + \frac{1}{\ell\sigma_7^2}\Bigg[\Big(Mm\mathbf{s}_{\sigma_8}\dot{\theta}_1^2h^2\ell$$
$$- 4Mm\mathbf{c}_{(\theta_1-\theta_2)}\dot{\theta}_2^2h\ell^2 + 2m\mathbf{s}_{\sigma_8}(F_1+F_2)h\ell + 4\tau\mathbf{s}_{(\theta_1-\theta_2)}(M+m)h - 4L(M+m)(F_1-F_2)\ell\Big)2Mh^2m\mathbf{s}_{\sigma_8}\Bigg], \tag{A.15}$$

$$\boldsymbol{A_{7,4}} = -\frac{1}{\ell\sigma_7}\Bigg[4h\tau\mathbf{c}_{(\theta_1-\theta_2)}(M+m) + h\ell m\mathbf{c}_{\sigma_8}4(F_1+F_2) + 2Mh\ell m(h\mathbf{c}_{\sigma_8}\dot{\theta}_1^2 + 2\ell\mathbf{s}_{(\theta_1-\theta_2)}\dot{\theta}_2^2)\Bigg]$$
$$- \frac{1}{\ell\sigma_7^2}\Bigg[2Mh^2m\mathbf{s}_{\sigma_8}\Big(Mm\mathbf{s}_{\sigma_8}\dot{\theta}_1^2h^2\ell - 4Mm\mathbf{c}_{(\theta_1-\theta_2)}\dot{\theta}_2^2h\ell^2 + 2m\mathbf{s}_{\sigma_8}(F_1+F_2)h\ell + 4\tau\mathbf{s}_{(\theta_1-\theta_2)}(M+m)h$$
$$- 4L(M+m)(F_1-F_2)\ell\Big)\Bigg], \tag{A.16}$$

$$\boldsymbol{A_{7,7}} = \frac{2M\dot{\theta}_1h^2m\mathbf{s}_{(2\theta_1-2\theta_2)}}{\sigma_7}, \tag{A.17}$$

$$\boldsymbol{A_{7,8}} = -\frac{8M\dot{\theta}_2h\ell m\mathbf{c}_{(\theta_1-\theta_2)}}{\sigma_7}, \tag{A.18}$$

$$\boldsymbol{A_{8,3}} = \frac{1}{\ell^2\sigma_7^2}\Bigg[2h^2\mathbf{s}_{\sigma_8}\Big(8I_M\tau(M+m)^2 + M^2h^2\ell m^2(h\mathbf{c}_{(\theta_1-\theta_2)}\dot{\theta}_1^2 - \ell\mathbf{s}_{\sigma_8}\dot{\theta}_2^2 + \mathbf{c}_{(\theta_1-\theta_2)}2(F_1+F_2))$$
$$+ 2Mh^2m\tau(M+m) + 8I_M\ell m\mathbf{c}_{(\theta_1-\theta_2)}(M+m)(F_1+F_2) + 4I_M M\dot{\theta}_1^2h\ell m\mathbf{c}_{(\theta_1-\theta_2)}(M+m)$$
$$- 2LMh\ell m\mathbf{s}_{(\theta_1-\theta_2)}(M+m)(F_1-F_2)\Big)\Bigg] - \frac{1}{M\ell^2m\sigma_7}\Bigg[\mathbf{s}_{(\theta_1-\theta_2)}\Big(8I_M\ell m(M+m) + 2Mh^2\ell m^2\Big)(F_1+F_2)$$
$$+ 2M^2\dot{\theta}_2^2h^2\ell^2m^2\mathbf{c}_{\sigma_8} + M\dot{\theta}_1^2h\ell m\mathbf{s}_{(\theta_1-\theta_2)}\Big(Mmh^2 + 4I_M(M+m)\Big) + 2LMh\ell m\mathbf{c}_{(\theta_1-\theta_2)}(M+m)(F_1-F_2)\Bigg], \tag{A.19}$$

$$\boldsymbol{A_{8,4}} = \frac{1}{M\ell^2m\sigma_7}\Bigg[\mathbf{s}_{(\theta_1-\theta_2)}\Big(8I_M\ell m(M+m) + 2Mh^2\ell m^2\Big)(F_1+F_2) + 2M^2\dot{\theta}_2^2h^2\ell^2m^2\mathbf{c}_{\sigma_8}$$
$$+ M\dot{\theta}_1^2h\ell m\mathbf{s}_{(\theta_1-\theta_2)}\Big(Mmh^2 + 4I_M(M+m)\Big) + 2LMh\ell m\mathbf{c}_{(\theta_1-\theta_2)}(M+m)(F_1-F_2)\Bigg]$$
$$- \frac{1}{\ell^2\sigma_7^2}\Bigg[2h^2\mathbf{s}_{\sigma_8}\Big(8I_M\tau(M+m)^2 + M^2h^2\ell m^2(h\mathbf{c}_{(\theta_1-\theta_2)}\dot{\theta}_1^2 - \ell\mathbf{s}_{\sigma_8}\dot{\theta}_2^2 + \mathbf{c}_{(\theta_1-\theta_2)}2(F_1+F_2))$$
$$+ 2Mh^2m\tau(M+m) + 8I_M\ell m\mathbf{c}_{(\theta_1-\theta_2)}(M+m)(F_1+F_2) + 4I_M M\dot{\theta}_1^2h\ell m\mathbf{c}_{(\theta_1-\theta_2)}(M+m)$$
$$- 2LMh\ell m\mathbf{s}_{(\theta_1-\theta_2)}(M+m)(F_1-F_2)\Big)\Bigg], \tag{A.20}$$

$$\boldsymbol{A_{8,7}} = \frac{2M^2\theta_1h^3\ell m^2\mathbf{c}_{(\theta_1-\theta_2)} + 8I_M M\dot{\theta}_1h\ell m\mathbf{c}_{(\theta_1-\theta_2)}(M+m)}{M\ell^2m\sigma_7}, \tag{A.21}$$

$$\boldsymbol{A_{8,8}} = -\frac{2M\dot{\theta}_2h^2m\mathbf{s}_{(2\theta_1-2\theta_2)}}{\sigma_7}. \tag{A.22}$$

The B matrix is,

$$B = \begin{bmatrix} 0 & 0 & 0 \\ 0 & 0 & 0 \\ 0 & 0 & 0 \\ 0 & 0 & 0 \\ \boldsymbol{B_{5,1}} & \boldsymbol{B_{5,2}} & \boldsymbol{B_{5,3}} \\ \boldsymbol{B_{6,1}} & \boldsymbol{B_{6,2}} & \boldsymbol{B_{6,3}} \\ \boldsymbol{B_{7,1}} & \boldsymbol{B_{7,2}} & \boldsymbol{B_{7,3}} \\ \boldsymbol{B_{8,1}} & \boldsymbol{B_{8,2}} & \boldsymbol{B_{8,3}} \end{bmatrix}, \tag{A.23}$$

where

$$\boldsymbol{B_{5,1}} = \frac{1}{2M\ell\sigma_7}\left[- M\ell m\Big((\mathbf{s}_{(3\theta_1-2\theta_2)} - \sigma_1 + 2\mathbf{s}_{\theta_1})h^2 + 2L(\mathbf{c}_{(\theta_1-2\theta_2)} + \mathbf{c}_{\theta_1})h\Big) + 8I_M\ell m(\sigma_1 - \mathbf{s}\theta_1) - 16I_M M\ell\mathbf{s}_{\theta_1}\right], \tag{A.24}$$

$$\boldsymbol{B_{5,2}} = -\frac{1}{2M\ell\sigma_7}\left[M\ell m\Big((\mathbf{s}_{(3\theta_1-2\theta_2)} - \sigma_1 + 2\mathbf{s}_{\theta_1})h^2 + 2L(\mathbf{c}_{(\theta_1-2\theta_2)} + \mathbf{c}_{\theta_1})h\Big) - 8I_M\ell m(\sigma_1 - \mathbf{s}\theta_1) + 16I_M M\ell\mathbf{s}_{\theta_1}\right], \tag{A.25}$$

$$\boldsymbol{B_{5,3}} = -\frac{2Mm(\mathbf{s}_{(2\theta_1-\theta_2)} + \mathbf{s}_{\theta_2})h^2 + 16I_M\mathbf{s}_{\theta_2}(M+m)}{2M\ell\sigma_7}, \tag{A.26}$$

$$\boldsymbol{B_{6,1}} = \frac{1}{2M\ell\sigma_7}\left[M\ell m\Big((\sigma_2 + \mathbf{c}_{(3\theta_1-2\theta_2)} + 2\mathbf{c}_{\theta_1})h^2 - 2L(\mathbf{s}_{(\theta_1-2\theta_2)} - \mathbf{s}_{\theta_1})h\Big) + 8I_M\ell m(\sigma_2 + \mathbf{c}\theta_1) + 16I_M M\ell\mathbf{c}_{\theta_1}\right], \tag{A.27}$$

$$\boldsymbol{B_{6,2}} = \frac{1}{2M\ell\sigma_7}\left[M\ell m\Big((\sigma_2 + \mathbf{c}_{(3\theta_1-2\theta_2)} + 2\mathbf{c}_{\theta_1})h^2 + 2L(\mathbf{s}_{(\theta_1-2\theta_2)} - \mathbf{s}_{\theta_1})h\Big) + 8I_M\ell m(\sigma_2 + \mathbf{c}\theta_1) + 16I_M M\ell\mathbf{c}_{\theta_1}\right], \tag{A.28}$$

$$\boldsymbol{B_{6,3}} = -\frac{2Mm(\mathbf{c}_{(2\theta_1-\theta_2)} + \mathbf{c}_{\theta_2})h^2 + 16I_M\mathbf{c}_{\theta_2}(M+m)}{2M\ell\sigma_7}, \tag{A.29}$$

$$\boldsymbol{B_{7,1}} = -\frac{4L\ell(M+m) - 2h\ell m\mathbf{s}_{(2\theta_1-2\theta_2)}}{\ell\sigma_7}, \tag{A.30}$$

$$\boldsymbol{B_{7,2}} = \frac{4L\ell(M+m) + 2h\ell m\mathbf{s}_{(2\theta_1-2\theta_2)}}{\ell\sigma_7}, \tag{A.31}$$

$$\boldsymbol{B_{7,3}} = \frac{4h\mathbf{s}_{(\theta_1-\theta_2)}(M+m)}{\ell\sigma_7}, \tag{A.32}$$

$$\boldsymbol{B_{8,1}} = \frac{1}{M\ell^2 m\sigma_7}\left[8I_M\ell m\mathbf{c}_{(\theta_1-\theta_2)}(M+m) + 2Mh^2\ell m^2\mathbf{c}_{(\theta_1-\theta_2)} - 2LMh\ell m\mathbf{s}_{(\theta_1-\theta_2)}(M+m)\right], \tag{A.33}$$

$$\boldsymbol{B_{8,2}} = \frac{1}{M\ell^2 m\sigma_7}\left[8I_M\ell m\mathbf{c}_{(\theta_1-\theta_2)}(M+m) + 2Mh^2\ell m^2\mathbf{c}_{(\theta_1-\theta_2)} + 2LMh\ell m\mathbf{s}_{(\theta_1-\theta_2)}(M+m)\right], \tag{A.34}$$

$$\boldsymbol{B_{8,3}} = \frac{\Big(2Mmh^2 + 8I_M(M+m)\Big)(M+m)}{M\ell^2 m\sigma_7}, \tag{A.35}$$

with the variables below;

$$\sigma_1 = \mathbf{s}_{(\theta_1 - 2\theta_2)}, \tag{A.36a}$$

$$\sigma_2 = \mathbf{c}_{(\theta_1 - 2\theta_2)}, \tag{A.36b}$$

$$\sigma_3 = 3\theta_1 - 2\theta_2, \tag{A.36c}$$

$$\sigma_4 = 16F_1 + 16F_2, \tag{A.36d}$$

$$\sigma_5 = 8F_1 + 8F_2, \tag{A.36e}$$

$$\sigma_6 = 2F_1 - 2F_2, \tag{A.36f}$$

$$\sigma_7 = Mm(\mathbf{c}_{\sigma_8} + 1)h^2 + 8I_M(M + m), \tag{A.36g}$$

$$\sigma_8 = 2\theta_1 - 2\theta_2. \tag{A.36h}$$

A.3 Conventional Quadrotor Platform

The conventional quadrotor platform has A matrix defined below;

$$A = \begin{bmatrix}
0 & 0 & 0 & 0 & 0 & 0 & 1 & 0 & 0 & 0 & 0 & 0 \\
0 & 0 & 0 & 0 & 0 & 0 & 0 & 1 & 0 & 0 & 0 & 0 \\
0 & 0 & 0 & 0 & 0 & 0 & 0 & 0 & 1 & 0 & 0 & 0 \\
0 & 0 & 0 & \boldsymbol{A_{4,4}} & \boldsymbol{A_{4,5}} & 0 & 0 & 0 & 0 & 1 & \boldsymbol{A_{4,11}} & \boldsymbol{A_{4,12}} \\
0 & 0 & 0 & \boldsymbol{A_{5,4}} & 0 & 0 & 0 & 0 & 0 & 0 & \boldsymbol{A_{5,11}} & \boldsymbol{A_{5,12}} \\
0 & 0 & 0 & \boldsymbol{A_{6,4}} & \boldsymbol{A_{6,5}} & 0 & 0 & 0 & 0 & 0 & \boldsymbol{A_{6,11}} & \boldsymbol{A_{6,12}} \\
0 & 0 & 0 & \boldsymbol{A_{7,4}} & \boldsymbol{A_{7,5}} & \boldsymbol{A_{7,6}} & 0 & 0 & 0 & 0 & 0 & 0 \\
0 & 0 & 0 & \boldsymbol{A_{8,4}} & \boldsymbol{A_{8,5}} & \boldsymbol{A_{8,6}} & 0 & 0 & 0 & 0 & 0 & 0 \\
0 & 0 & 0 & \boldsymbol{A_{9,4}} & \boldsymbol{A_{9,5}} & 0 & 0 & 0 & 0 & 0 & 0 & 0 \\
0 & 0 & 0 & 0 & 0 & 0 & 0 & 0 & 0 & 0 & \boldsymbol{A_{10,11}} & \boldsymbol{A_{10,12}} \\
0 & 0 & 0 & 0 & 0 & 0 & 0 & 0 & 0 & \boldsymbol{A_{11,10}} & 0 & \boldsymbol{A_{11,12}} \\
0 & 0 & 0 & 0 & 0 & 0 & 0 & 0 & 0 & 0 & 0 & 0
\end{bmatrix}, \tag{A.37}$$

where

$$\boldsymbol{A_{4,4}} = q\mathbf{c}_\phi \mathbf{t}_\theta - r\mathbf{s}_\phi \mathbf{t}_\theta, \tag{A.38}$$

$$\boldsymbol{A_{4,5}} = q\mathbf{s}_\phi(1 + \mathbf{t}_\theta^2) + r\mathbf{c}_\phi(1 + \mathbf{t}_\theta^2), \tag{A.39}$$

$$\boldsymbol{A_{4,11}} = \mathbf{s}_\phi \mathbf{t}_\theta, \tag{A.40}$$

$$\boldsymbol{A_{4,12}} = \mathbf{c}_\phi \mathbf{t}_\theta, \tag{A.41}$$

$$\boldsymbol{A_{5,4}} = -q\mathbf{s}_\phi - r\mathbf{c}_\phi, \tag{A.42}$$

$$\boldsymbol{A_{5,11}} = \mathbf{c}_\phi \tag{A.43}$$

$$\boldsymbol{A_{5,12}} = -\mathbf{s}_\phi \tag{A.44}$$

$$\boldsymbol{A_{6,4}} = \frac{q\mathbf{c}_\phi}{\mathbf{c}_\theta} - \frac{r\mathbf{s}_\phi}{\mathbf{c}_\theta}, \tag{A.45}$$

$$\boldsymbol{A_{6,5}} = \frac{q\mathbf{s}_\phi \mathbf{s}_\theta}{\mathbf{c}_\theta^2} + \frac{r\mathbf{c}_\phi \mathbf{s}_\theta}{\mathbf{c}_\theta^2}, \tag{A.46}$$

$$\tag{A.47}$$

$$\boldsymbol{A_{6,11}} = \frac{\mathbf{s}_\phi}{\mathbf{c}_\theta}, \tag{A.48}$$

$$\boldsymbol{A_{6,12}} = \frac{\mathbf{c}_\phi}{\mathbf{c}_\theta}, \tag{A.49}$$

$$\boldsymbol{A_{7,4}} = -\frac{1}{M}\left(-\mathbf{s}_\phi \mathbf{s}_\theta \mathbf{c}_\psi + \mathbf{c}_\phi \mathbf{s}_\psi\right) U_1, \tag{A.50}$$

$$\boldsymbol{A_{7,5}} = -\frac{1}{M}\left(\mathbf{c}_\phi \mathbf{c}_\theta \mathbf{c}_\psi\right) U_1, \tag{A.51}$$

$$\boldsymbol{A_{7,6}} = -\frac{1}{M}\left(-\mathbf{c}_\phi \mathbf{s}_\theta \mathbf{s}_\psi + \mathbf{s}_\phi \mathbf{c}_\psi\right) U_1, \tag{A.52}$$

$$\boldsymbol{A_{8,4}} = -\frac{1}{M}\left(-\mathbf{s}_\phi \mathbf{s}_\theta \mathbf{s}_\psi - \mathbf{c}_\phi \mathbf{c}_\psi\right) U_1, \tag{A.53}$$

$$\boldsymbol{A_{8,5}} = -\frac{1}{M}\left(\mathbf{c}_\phi \mathbf{c}_\theta \mathbf{s}_\psi\right) U_1, \tag{A.54}$$

$$\boldsymbol{A_{8,6}} = -\frac{1}{M}\left(\mathbf{c}_\phi \mathbf{s}_\theta \mathbf{c}_\psi + \mathbf{s}_\phi \mathbf{s}_\psi\right) U_1, \tag{A.55}$$

$$\boldsymbol{A_{9,4}} = -\frac{1}{M}\left(-\mathbf{s}_\phi \mathbf{c}_\theta\right) U_1 \tag{A.56}$$

$$\boldsymbol{A_{9,5}} = -\frac{1}{M}\left(-\mathbf{c}_\phi \mathbf{s}_\theta\right) U_1, \tag{A.57}$$

$$\boldsymbol{A_{10,11}} = \frac{U_R J_r + (J_{yy} - J_{zz}) r}{J_{xx}} \tag{A.58}$$

$$\boldsymbol{A_{10,12}} = \frac{(J_{yy} - J_{zz}) q}{J_{xx}} \tag{A.59}$$

$$\boldsymbol{A_{11,10}} = \frac{(J_{zz} - J_{xx}) r - U_R J_r}{J_{yy}} \tag{A.60}$$

$$\boldsymbol{A_{11,12}} = \frac{(J_{zz} - J_{xx}) p}{J_{yy}}. \tag{A.61}$$

And B matrix is as follows;

$$B = \begin{bmatrix} 0 & 0 & 0 & 0 \\ 0 & 0 & 0 & 0 \\ 0 & 0 & 0 & 0 \\ 0 & 0 & 0 & 0 \\ 0 & 0 & 0 & 0 \\ 0 & 0 & 0 & 0 \\ \boldsymbol{B_{7,1}} & 0 & 0 & 0 \\ \boldsymbol{B_{8,1}} & 0 & 0 & 0 \\ \boldsymbol{B_{9,1}} & 0 & 0 & 0 \\ 0 & \boldsymbol{B_{10,2}} & 0 & 0 \\ 0 & 0 & \boldsymbol{B_{11,3}} & 0 \\ 0 & 0 & 0 & \boldsymbol{B_{12,4}} \end{bmatrix}, \tag{A.62}$$

where

$$\boldsymbol{B_{7,1}} = -\frac{1}{M}(\mathbf{c}_\phi \mathbf{s}_\theta \mathbf{c}_\psi + \mathbf{s}_\phi \mathbf{s}_\psi), \tag{A.63}$$

$$\boldsymbol{B_{8,1}} = -\frac{1}{M}(\mathbf{c}_\phi \mathbf{s}_\theta \mathbf{s}_\psi - \mathbf{s}_\phi \mathbf{c}_\psi), \tag{A.64}$$

$$\boldsymbol{B_{9,1}} = -\frac{1}{M}(\mathbf{c}_\phi \mathbf{c}_\theta), \tag{A.65}$$

$$\boldsymbol{B_{10,2}} = 1/J_{xx}, \tag{A.66}$$

$$\boldsymbol{B_{11,3}} = 1/J_{yy}, \tag{A.67}$$

$$\boldsymbol{B_{12,4}} = 1/J_{zz}. \tag{A.68}$$

A.4 Proposed Quadrotor Platform with 2-DOF Abdomen-like Appendage

The linearized state-space model of the quadrotor platform with 2-DOF abdomen-like appendage has the matrix A below;

$$A = \begin{bmatrix}
0 & 0 & 0 & 0 & 0 & 0 & 0 & 0 & 1 & 0 & 0 & 0 & 0 & 0 & 0 & 0 \\
0 & 0 & 0 & 0 & 0 & 0 & 0 & 0 & 0 & 1 & 0 & 0 & 0 & 0 & 0 & 0 \\
0 & 0 & 0 & 0 & 0 & 0 & 0 & 0 & 0 & 0 & 1 & 0 & 0 & 0 & 0 & 0 \\
0 & 0 & 0 & \boldsymbol{A_{4,4}} & \boldsymbol{A_{4,5}} & 0 & 0 & 0 & 0 & 0 & 0 & 1 & A_{4,13} & \boldsymbol{A_{4,14}} & 0 & 0 \\
0 & 0 & 0 & \boldsymbol{A_{5,4}} & 0 & 0 & 0 & 0 & 0 & 0 & 0 & 0 & \boldsymbol{A_{5,13}} & \boldsymbol{A_{5,14}} & 0 & 0 \\
0 & 0 & 0 & \boldsymbol{A_{6,4}} & \boldsymbol{A_{6,5}} & 0 & 0 & 0 & 0 & 0 & 0 & 0 & \boldsymbol{A_{6,13}} & \boldsymbol{A_{6,14}} & 0 & 0 \\
0 & 0 & 0 & 0 & 0 & 0 & 0 & 0 & 0 & 0 & 0 & 0 & 0 & 0 & 1 & 0 \\
0 & 0 & 0 & 0 & 0 & 0 & 0 & 0 & 0 & 0 & 0 & 0 & 0 & 0 & 0 & 1 \\
0 & 0 & 0 & \boldsymbol{A_{9,4}} & \boldsymbol{A_{9,5}} & \boldsymbol{A_{9,6}} & \boldsymbol{A_{9,7}} & \boldsymbol{A_{9,8}} & 0 & 0 & 0 & 0 & 0 & 0 & \boldsymbol{A_{9,15}} & \boldsymbol{A_{9,16}} \\
0 & 0 & 0 & \boldsymbol{A_{10,4}} & \boldsymbol{A_{10,5}} & \boldsymbol{A_{10,6}} & \boldsymbol{A_{10,7}} & \boldsymbol{A_{10,8}} & 0 & 0 & 0 & 0 & 0 & 0 & \boldsymbol{A_{10,15}} & \boldsymbol{A_{10,16}} \\
0 & 0 & 0 & \boldsymbol{A_{11,4}} & \boldsymbol{A_{11,5}} & \boldsymbol{A_{11,6}} & \boldsymbol{A_{11,7}} & \boldsymbol{A_{11,8}} & 0 & 0 & 0 & 0 & 0 & 0 & \boldsymbol{A_{11,15}} & \boldsymbol{A_{11,16}} \\
0 & 0 & 0 & 0 & 0 & 0 & 0 & 0 & 0 & 0 & 0 & 0 & \boldsymbol{A_{12,13}} & \boldsymbol{A_{12,14}} & 0 & 0 \\
0 & 0 & 0 & 0 & 0 & 0 & 0 & 0 & 0 & 0 & 0 & \boldsymbol{A_{13,12}} & 0 & \boldsymbol{A_{13,14}} & 0 & 0 \\
0 & 0 & 0 & 0 & 0 & 0 & 0 & 0 & 0 & 0 & 0 & 0 & 0 & 0 & 0 & 0 \\
0 & 0 & 0 & \boldsymbol{A_{15,4}} & \boldsymbol{A_{15,5}} & \boldsymbol{A_{15,6}} & \boldsymbol{A_{15,7}} & \boldsymbol{A_{15,8}} & 0 & 0 & 0 & 0 & 0 & 0 & 0 & \boldsymbol{A_{15,16}} \\
0 & 0 & 0 & \boldsymbol{A_{16,4}} & \boldsymbol{A_{16,5}} & \boldsymbol{A_{16,6}} & \boldsymbol{A_{16,7}} & \boldsymbol{A_{16,8}} & 0 & 0 & 0 & 0 & 0 & 0 & \boldsymbol{A_{16,15}} & \boldsymbol{A_{16,16}}
\end{bmatrix}, \tag{A.69}$$

where

$$\boldsymbol{A_{4,4}} = q\mathbf{c}_\phi\mathbf{t}_\theta - r\mathbf{s}_\phi\mathbf{t}_\theta, \tag{A.70}$$

$$\boldsymbol{A_{4,5}} = q\mathbf{s}_\phi(1+\mathbf{t}_\theta^2) + r\mathbf{c}_\phi(1+\mathbf{t}_\theta^2), \tag{A.71}$$

$$\boldsymbol{A_{4,13}} = \mathbf{s}_\phi\mathbf{t}_\theta, \tag{A.72}$$

$$\boldsymbol{A_{4,14}} = \mathbf{c}_\phi\mathbf{t}_\theta, \tag{A.73}$$

$$\boldsymbol{A_{5,4}} = -q\mathbf{s}_\phi - r\mathbf{c}_\phi, \tag{A.74}$$

$$\boldsymbol{A_{5,13}} = \mathbf{c}_\phi, \tag{A.75}$$

$$\boldsymbol{A_{5,14}} = -\mathbf{s}_\phi, \tag{A.76}$$

$$\boldsymbol{A_{6,4}} = q\frac{\mathbf{c}_\phi}{\mathbf{c}_\theta} - r\frac{\mathbf{s}_\phi}{\mathbf{c}_\theta}, \tag{A.77}$$

$$\boldsymbol{A_{6,5}} = q\frac{\mathbf{s}_\phi\mathbf{s}_\theta}{\mathbf{c}_\theta^2} + r\frac{\mathbf{c}_\phi\mathbf{s}_\theta}{\mathbf{c}_\theta^2}, \tag{A.78}$$

$$\boldsymbol{A_{6,13}} = \frac{\mathbf{s}_\phi}{\mathbf{c}_\theta}, \tag{A.79}$$

$$\boldsymbol{A_{6,14}} = \frac{\mathbf{c}_\phi}{\mathbf{c}_\theta}, \tag{A.80}$$

$$\boldsymbol{A_{9,4}} = -\frac{1}{M+m}\left((-\mathbf{s}_\phi\mathbf{s}_\theta\mathbf{c}_\psi + \mathbf{c}_\phi\mathbf{s}_\psi)U_1 + mL\left(\frac{\partial\ddot{\theta_a}}{\partial\phi}\mathbf{c}_{\theta_a}\mathbf{c}_{\phi_a} - \frac{\partial\ddot{\phi_a}}{\partial\phi}\mathbf{s}_{\theta_a}\mathbf{s}_{\phi_a}\right)\right), \tag{A.81}$$

$$\boldsymbol{A_{9,5}} = -\frac{1}{M+m}\left((\mathbf{c}_\phi\mathbf{c}_\theta\mathbf{c}_\psi)U_1 + mL\left(\frac{\partial\ddot{\theta_a}}{\partial\theta}\mathbf{c}_{\theta_a}\mathbf{c}_{\phi_a} - \frac{\partial\ddot{\phi_a}}{\partial\theta}\mathbf{s}_{\theta_a}\mathbf{s}_{\phi_a}\right)\right), \tag{A.82}$$

$$\boldsymbol{A_{9,6}} = -\frac{1}{M+m}\left((-\mathbf{c}_\phi\mathbf{s}_\theta\mathbf{s}_\psi + \mathbf{s}_\phi\mathbf{c}_\psi)U_1 + mL\left(\frac{\partial\ddot{\theta_a}}{\partial\psi}\mathbf{c}_{\theta_a}\mathbf{c}_{\phi_a} - \frac{\partial\ddot{\phi_a}}{\partial\psi}\mathbf{s}_{\theta_a}\mathbf{s}_{\phi_a}\right)\right), \tag{A.83}$$

$$\boldsymbol{A_{9,7}} = -\frac{1}{M+m}\left(mL\left(\frac{\partial\ddot{\theta_a}}{\partial\phi_a}\mathbf{c}_{\theta_a}\mathbf{c}_{\phi_a} + \dot{\theta}_a^2\mathbf{s}_{\theta_a}\mathbf{s}_{\phi_a} - 2\dot{\theta}_a\dot{\phi}_a\mathbf{c}_{\theta_a}\mathbf{c}_{\phi_a} - \frac{\partial\ddot{\phi_a}}{\partial\phi_a}\mathbf{s}_{\theta_a}\mathbf{s}_{\phi_a} + \dot{\phi}_a^2\mathbf{s}_{\theta_a}\mathbf{s}_{\phi_a}\right)\right), \tag{A.84}$$

$$\boldsymbol{A_{9,8}} = -\frac{1}{M+m}\left(mL\left(\frac{\partial\ddot{\theta_a}}{\partial\theta_a}\mathbf{c}_{\theta_a}\mathbf{c}_{\phi_a} - \dot{\theta}_a^2\mathbf{c}_{\theta_a}\mathbf{c}_{\phi_a} + 2\dot{\theta}_a\dot{\phi}_a\mathbf{s}_{\theta_a}\mathbf{s}_{\phi_a} - \frac{\partial\ddot{\phi_a}}{\partial\theta_a}\mathbf{s}_{\theta_a}\mathbf{s}_{\phi_a} - \dot{\phi}_a^2\mathbf{c}_{\theta_a}\mathbf{c}_{\phi_a}\right)\right), \tag{A.85}$$

$$\boldsymbol{A_{9,15}} = -\frac{1}{M+m}\left(mL\left(\frac{\partial\ddot{\theta_a}}{\partial\dot{\phi_a}}\mathbf{c}_{\theta_a}\mathbf{c}_{\phi_a} - 2\dot{\theta}_a\mathbf{c}_{\theta_a}\mathbf{s}_{\phi_a} - \frac{\partial\ddot{\phi_a}}{\partial\dot{\phi_a}}\mathbf{s}_{\theta_a}\mathbf{s}_{\phi_a} - 2\dot{\phi}_a\mathbf{s}_{\theta_a}\mathbf{c}_{\phi_a}\right)\right), \tag{A.86}$$

$$\boldsymbol{A_{9,16}} = -\frac{1}{M+m}\left(mL\left(\frac{\partial\ddot{\theta_a}}{\partial\dot{\theta_a}}\mathbf{c}_{\theta_a}\mathbf{c}_{\phi_a} - 2\dot{\theta}_a\mathbf{s}_{\theta_a}\mathbf{c}_{\phi_a} - \frac{\partial\ddot{\phi_a}}{\partial\dot{\theta_a}}\mathbf{s}_{\theta_a}\mathbf{s}_{\phi_a} - 2\dot{\phi}_a\mathbf{c}_{\theta_a}\mathbf{s}_{\phi_a}\right)\right), \tag{A.87}$$

$$\boldsymbol{A_{10,4}} = \frac{1}{M+m}\left(-(-\mathbf{s}_\phi\mathbf{s}_\theta\mathbf{s}_\psi - \mathbf{c}_\phi\mathbf{c}_\psi)U_1 + mL\left(\frac{\partial\ddot{\phi_a}}{\partial\phi}\mathbf{c}_{\phi_a}\right)\right), \tag{A.88}$$

$$\boldsymbol{A_{10,5}} = \frac{1}{M+m}\left(-(\mathbf{c}_\phi\mathbf{c}_\theta\mathbf{s}_\psi)U_1 + mL\left(\frac{\partial\ddot{\phi_a}}{\partial\theta}\mathbf{c}_{\phi_a}\right)\right), \tag{A.89}$$

$$\boldsymbol{A_{10,6}} = \frac{1}{M+m}\left(-(\mathbf{c}_\phi\mathbf{s}_\theta\mathbf{c}_\psi + \mathbf{s}_\phi\mathbf{s}_\psi)U_1 + mL\left(\frac{\partial\ddot{\phi_a}}{\partial\psi}\mathbf{c}_{\phi_a}\right)\right), \tag{A.90}$$

$$\boldsymbol{A_{10,7}} = \frac{1}{M+m}\left(mL\left(\frac{\partial\ddot{\phi_a}}{\partial\phi_a}\mathbf{c}_{\phi_a} - \dot{\phi}_a^2\mathbf{c}_{\phi_a}\right)\right), \tag{A.91}$$

$$\boldsymbol{A_{10,8}} = \frac{1}{M+m}\left(mL\left(\frac{\partial\ddot{\phi_a}}{\partial\theta_a}\mathbf{c}_{\phi_a}\right)\right), \tag{A.92}$$

$$\boldsymbol{A_{10,15}} = \frac{1}{M+m}\left(mL\left(\frac{\partial\ddot{\phi_a}}{\partial\dot{\phi_a}}\mathbf{c}_{\phi_a} - 2\dot{\phi}_a\mathbf{s}_{\phi_a}\right)\right), \tag{A.93}$$

$$\boldsymbol{A_{10,16}} = \frac{1}{M+m}\left(mL\left(\frac{\partial\ddot{\phi_a}}{\partial\dot{\theta_a}}\mathbf{c}_{\phi_a}\right)\right), \tag{A.94}$$

$$\boldsymbol{A_{11,4}} = \frac{1}{M+m}\left((\mathbf{s}_\phi\mathbf{c}_\theta)U_1 + mL\left(\frac{\partial\ddot{\theta_a}}{\partial\phi}\mathbf{s}_{\theta_a}\mathbf{c}_{\phi_a} + \frac{\partial\ddot{\phi_a}}{\partial\phi}\mathbf{c}_{\theta_a}\mathbf{s}_{\phi_a}\right)\right), \tag{A.95}$$

$$\boldsymbol{A_{11,5}} = \frac{1}{M+m}\left((\mathbf{c}_\phi\mathbf{s}_\theta)U_1 + mL\left(\frac{\partial\ddot{\theta_a}}{\partial\theta}\mathbf{s}_{\theta_a}\mathbf{c}_{\phi_a} + \frac{\partial\ddot{\phi_a}}{\partial\theta}\mathbf{c}_{\theta_a}\mathbf{s}_{\phi_a}\right)\right), \tag{A.96}$$

$$\boldsymbol{A_{11,6}} = \frac{1}{M+m}\left(mL\left(\frac{\partial\ddot{\theta_a}}{\partial\psi}\mathbf{s}_{\theta_a}\mathbf{c}_{\phi_a} + \frac{\partial\ddot{\phi_a}}{\partial\psi}\mathbf{c}_{\theta_a}\mathbf{s}_{\phi_a}\right)\right), \tag{A.97}$$

$$\boldsymbol{A_{11,7}} = \frac{1}{M+m}\left(mL\left(\frac{\partial\ddot{\theta_a}}{\partial\phi_a}\mathbf{s}_{\theta_a}\mathbf{c}_{\phi_a} - \dot{\theta}_a^2\mathbf{c}_{\theta_a}\mathbf{s}_{\phi_a} - 2\dot{\theta_a}\dot{\phi_a}\mathbf{s}_{\theta_a}\mathbf{c}_{\phi_a} + \frac{\partial\ddot{\phi_a}}{\partial\phi_a}\mathbf{c}_{\theta_a}\mathbf{s}_{\phi_a} - \dot{\phi}_a^2\mathbf{c}_{\theta_a}\mathbf{s}_{\phi_a}\right)\right), \tag{A.98}$$

$$\boldsymbol{A_{11,8}} = \frac{1}{M+m}\left(mL\left(\frac{\partial\ddot{\theta_a}}{\partial\theta_a}\mathbf{s}_{\theta_a}\mathbf{c}_{\phi_a} - \dot{\theta}_a^2\mathbf{s}_{\theta_a}\mathbf{c}_{\phi_a} - 2\dot{\theta_a}\dot{\phi_a}\mathbf{c}_{\theta_a}\mathbf{s}_{\phi_a} + \frac{\partial\ddot{\phi_a}}{\partial\theta_a}\mathbf{c}_{\theta_a}\mathbf{s}_{\phi_a} - \dot{\phi}_a^2\mathbf{s}_{\theta_a}\mathbf{c}_{\phi_a}\right)\right), \tag{A.99}$$

$$\boldsymbol{A_{11,15}} = \frac{1}{M+m}\left(mL\left(\frac{\partial\ddot{\theta_a}}{\partial\dot{\phi_a}}\mathbf{s}_{\theta_a}\mathbf{c}_{\phi_a} - 2\dot{\theta}_a\mathbf{s}_{\theta_a}\mathbf{s}_{\phi_a} + \frac{\partial\ddot{\phi_a}}{\partial\dot{\phi_a}}\mathbf{c}_{\theta_a}\mathbf{s}_{\phi_a} + 2\dot{\phi}_a\mathbf{c}_{\theta_a}\mathbf{c}_{\phi_a}\right)\right), \tag{A.100}$$

$$\boldsymbol{A_{11,16}} = \frac{1}{M+m}\left(mL\left(\frac{\partial\ddot{\theta_a}}{\partial\dot{\theta_a}}\mathbf{s}_{\theta_a}\mathbf{c}_{\phi_a} + 2\dot{\theta}_a\mathbf{c}_{\theta_a}\mathbf{c}_{\phi_a} + \frac{\partial\ddot{\phi_a}}{\partial\dot{\theta_a}}\mathbf{c}_{\theta_a}\mathbf{s}_{\phi_a} - 2\dot{\phi}_a\mathbf{s}_{\theta_a}\mathbf{s}_{\phi_a}\right)\right), \tag{A.101}$$

$$\boldsymbol{A_{12,13}} = \frac{U_R J_R + (J_{yy} - J_{zz})r}{J_{xx}}, \tag{A.102}$$

$$\boldsymbol{A_{12,14}} = \frac{(J_{yy} - J_{zz})q}{J_{xx}}, \tag{A.103}$$

$$\boldsymbol{A_{13,12}} = \frac{(J_{zz} - J_{xx})r - U_R J_R}{J_{yy}}, \tag{A.104}$$

$$\boldsymbol{A_{13,14}} = \frac{(J_{zz} - J_{xx})p}{J_{yy}}, \tag{A.105}$$

$$\boldsymbol{A_{15,4}} = \frac{1}{ML}\left((-\mathbf{s}_{\theta_a}\mathbf{s}_{\phi_a}(-\mathbf{s}_\phi\mathbf{s}_\theta\mathbf{c}_\psi + \mathbf{c}_\phi\mathbf{s}_\psi) - \mathbf{c}_{\phi_a}(-\mathbf{s}_\phi\mathbf{s}_\theta\mathbf{s}_\psi - \mathbf{c}_\phi\mathbf{c}_\psi) + \mathbf{c}_{\theta_a}\mathbf{s}_{\phi_a}\mathbf{s}_\phi\mathbf{c}_\theta)U_1\right), \tag{A.106}$$

$$\boldsymbol{A_{15,5}} = \frac{1}{ML}\left((-\mathbf{s}_{\theta_a}\mathbf{s}_{\phi_a}(\mathbf{c}_\phi\mathbf{c}_\theta\mathbf{c}_\psi) - \mathbf{c}_{\phi_a}(\mathbf{c}_\phi\mathbf{c}_\theta\mathbf{s}_\psi) + \mathbf{c}_{\theta_a}\mathbf{s}_{\phi_a}\mathbf{c}_\phi\mathbf{s}_\theta)U_1\right), \tag{A.107}$$

$$\boldsymbol{A_{15,6}} = \frac{1}{ML}\left(\left(-\mathbf{s}_{\theta_a}\mathbf{s}_{\phi_a}(-\mathbf{c}_\phi\mathbf{s}_\theta\mathbf{s}_\psi + \mathbf{s}_\phi\mathbf{c}_\psi) - \mathbf{c}_{\phi_a}(\mathbf{c}_\phi\mathbf{s}_\theta\mathbf{c}_\psi + \mathbf{s}_\phi\mathbf{s}_\psi)\right)U_1\right), \tag{A.108}$$

$$\boldsymbol{A_{15,7}} = \frac{1}{ML}\Bigg((-\mathbf{s}_{\theta_a}\mathbf{c}_{\phi_a}(\mathbf{c}_\phi\mathbf{s}_\theta\mathbf{c}_\psi + \mathbf{s}_\phi\mathbf{s}_\psi) + \mathbf{s}_{\phi_a}(\mathbf{c}_\phi\mathbf{s}_\theta\mathbf{s}_\psi - \mathbf{s}_\phi\mathbf{c}_\psi) - \mathbf{c}_{\theta_a}\mathbf{c}_{\phi_a}\mathbf{c}_\phi\mathbf{c}_\theta)U_1\Bigg) - (\mathbf{c}_{\phi_a}^2 - \mathbf{s}_{\phi_a}^2)\dot{\theta}_a^2, \quad \text{(A.109)}$$

$$\boldsymbol{A_{15,8}} = \frac{1}{ML}\Bigg((-\mathbf{c}_{\theta_a}\mathbf{s}_{\phi_a}(\mathbf{c}_\phi\mathbf{s}_\theta\mathbf{c}_\psi + \mathbf{s}_\phi\mathbf{s}_\psi) + \mathbf{s}_{\theta_a}\mathbf{s}_{\phi_a}\mathbf{c}_\phi\mathbf{c}_\theta)U_1\Bigg), \quad \text{(A.110)}$$

$$\boldsymbol{A_{15,16}} = -2\mathbf{s}_{\phi_a}\mathbf{c}_\phi\dot{\theta}_a, \quad \text{(A.111)}$$

$$\boldsymbol{A_{16,4}} = \frac{1}{M}\Bigg((-\mathbf{s}_\phi\mathbf{s}_\theta\mathbf{c}_\psi + \mathbf{c}_\phi\mathbf{s}_\psi)U_1\frac{\mathbf{c}_{\theta_a}}{L\mathbf{c}_{\phi_a}} + (\mathbf{s}_\phi\mathbf{c}_\theta)U_1\frac{\mathbf{s}_{\theta_a}}{L\mathbf{c}_{\phi_a}}\Bigg), \quad \text{(A.112)}$$

$$\boldsymbol{A_{16,5}} = \frac{1}{M}\Bigg((\mathbf{c}_\phi\mathbf{c}_\theta\mathbf{c}_\psi)U_1\frac{\mathbf{c}_{\theta_a}}{L\mathbf{c}_{\phi_a}} + (\mathbf{c}_\phi\mathbf{s}_\theta)U_1\frac{\mathbf{s}_{\theta_a}}{L\mathbf{c}_{\phi_a}}\Bigg), \quad \text{(A.113)}$$

$$\boldsymbol{A_{16,6}} = \frac{1}{M}\Bigg((-\mathbf{c}_\phi\mathbf{s}_\theta\mathbf{s}_\psi + \mathbf{s}_\phi\mathbf{c}_\psi)U_1\frac{\mathbf{c}_{\theta_a}}{L\mathbf{c}_{\phi_a}}\Bigg), \quad \text{(A.114)}$$

$$\boldsymbol{A_{16,7}} = \frac{1}{M}\Bigg(2\dot{\theta_a}\dot{\phi_a}M(1+\mathbf{t}_{\phi_a}^2) + (\mathbf{c}_\phi\mathbf{s}_\theta\mathbf{c}_\psi + \mathbf{s}_\phi\mathbf{s}_\psi)U_1\frac{\mathbf{c}_{\theta_a}\mathbf{s}_{\phi_a}}{L\mathbf{c}_{\phi_a}^2} + (-\mathbf{c}_\phi\mathbf{c}_\theta)U_1\frac{\mathbf{s}_{\theta_a}\mathbf{s}_{\phi_a}}{L\mathbf{c}_{\phi_a}^2}\Bigg), \quad \text{(A.115)}$$

$$\boldsymbol{A_{16,8}} = \frac{1}{M}\Bigg(-(\mathbf{c}_\phi\mathbf{s}_\theta\mathbf{c}_\psi + \mathbf{s}_\phi\mathbf{s}_\psi)U_1\frac{\mathbf{s}_{\theta_a}}{L\mathbf{c}_{\phi_a}} + (-\mathbf{c}_\phi\mathbf{c}_\theta)U_1\frac{\mathbf{c}_{\theta_a}}{L\mathbf{c}_{\phi_a}}\Bigg) \quad \text{(A.116)}$$

$$\boldsymbol{A_{16,15}} = 2\dot{\theta}_a\mathbf{t}_{\phi_a}, \quad \text{(A.117)}$$

$$\boldsymbol{A_{16,16}} = 2\dot{\phi}_a\mathbf{t}_{\phi_a}, \quad \text{(A.118)}$$

and the B matrix is as follows;

$$B = \begin{bmatrix} 0 & 0 & 0 & 0 & 0 & 0 \\ 0 & 0 & 0 & 0 & 0 & 0 \\ 0 & 0 & 0 & 0 & 0 & 0 \\ 0 & 0 & 0 & 0 & 0 & 0 \\ 0 & 0 & 0 & 0 & 0 & 0 \\ 0 & 0 & 0 & 0 & 0 & 0 \\ 0 & 0 & 0 & 0 & 0 & 0 \\ 0 & 0 & 0 & 0 & 0 & 0 \\ \boldsymbol{B_{9,1}} & \boldsymbol{B_{9,2}} & \boldsymbol{B_{9,3}} & \boldsymbol{B_{9,4}} & \boldsymbol{B_{9,5}} & \boldsymbol{B_{9,6}} \\ \boldsymbol{B_{10,1}} & \boldsymbol{B_{10,2}} & \boldsymbol{B_{10,3}} & \boldsymbol{B_{10,4}} & \boldsymbol{B_{10,5}} & \boldsymbol{B_{10,6}} \\ \boldsymbol{B_{11,1}} & \boldsymbol{B_{11,2}} & \boldsymbol{B_{11,3}} & \boldsymbol{B_{11,4}} & \boldsymbol{B_{11,5}} & \boldsymbol{B_{11,6}} \\ 0 & \boldsymbol{B_{12,2}} & 0 & 0 & 0 & 0 \\ 0 & 0 & \boldsymbol{B_{13,3}} & 0 & 0 & 0 \\ 0 & 0 & 0 & \boldsymbol{B_{14,4}} & 0 & 0 \\ 0 & 0 & 0 & 0 & \boldsymbol{B_{15,5}} & 0 \\ 0 & 0 & 0 & 0 & 0 & \boldsymbol{B_{16,6}} \end{bmatrix}, \quad \text{(A.119)}$$

where

$$\boldsymbol{B_{9,1}} = -\frac{1}{M+m}\Bigg((\mathbf{c}_\phi\mathbf{s}_\theta\mathbf{c}_\psi + \mathbf{s}_\phi\mathbf{s}_\psi) + mL\Big(\frac{\partial\ddot{\theta}_a}{\partial U_1}\mathbf{c}_{\theta_a}\mathbf{c}_{\phi_a} - \frac{\partial\ddot{\phi}_a}{\partial U_1}\mathbf{s}_{\theta_a}\mathbf{s}_{\phi_a}\Big)\Bigg), \quad \text{(A.120)}$$

$$\boldsymbol{B_{9,2}} = -\frac{1}{M+m}\Bigg(mL\Big(\frac{\partial\ddot{\theta}_a}{\partial U_2}\mathbf{c}_{\theta_a}\mathbf{c}_{\phi_a} - \frac{\partial\ddot{\phi}_a}{\partial U_2}\mathbf{s}_{\theta_a}\mathbf{s}_{\phi_a}\Big)\Bigg), \quad \text{(A.121)}$$

$$\boldsymbol{B_{9,3}} = -\frac{1}{M+m}\Bigg(mL\Big(\frac{\partial\ddot{\theta}_a}{\partial U_3}\mathbf{c}_{\theta_a}\mathbf{c}_{\phi_a} - \frac{\partial\ddot{\phi}_a}{\partial U_3}\mathbf{s}_{\theta_a}\mathbf{s}_{\phi_a}\Big)\Bigg), \quad \text{(A.122)}$$

$$\boldsymbol{B_{9,4}} = -\frac{1}{M+m}\left(mL(\frac{\partial\ddot{\theta_a}}{\partial U_4}\mathbf{c}_{\theta_a}\mathbf{c}_{\phi_a} - \frac{\partial\ddot{\phi_a}}{\partial U_4}\mathbf{s}_{\theta_a}\mathbf{s}_{\phi_a})\right), \tag{A.123}$$

$$\boldsymbol{B_{9,5}} = -\frac{1}{M+m}\left(mL\left(\frac{\partial\ddot{\theta_a}}{\partial \tau_x}\mathbf{c}_{\theta_a}\mathbf{c}_{\phi_a} - \frac{\partial\ddot{\phi_a}}{\partial \tau_x}\mathbf{s}_{\theta_a}\mathbf{s}_{\phi_a}\right)\right), \tag{A.124}$$

$$\boldsymbol{B_{9,6}} = -\frac{1}{M+m}\left(mL\left(\frac{\partial\ddot{\theta_a}}{\partial \tau_y}\mathbf{c}_{\theta_a}\mathbf{c}_{\phi_a} - \frac{\partial\ddot{\phi_a}}{\partial \tau_y}\mathbf{s}_{\theta_a}\mathbf{s}_{\phi_a}\right)\right), \tag{A.125}$$

$$\boldsymbol{B_{10,1}} = \frac{1}{M+m}\left(-(\mathbf{c}_\phi\mathbf{s}_\theta\mathbf{s}_\psi - \mathbf{s}_\phi\mathbf{c}_\psi) + mL\left(\frac{\partial\ddot{\phi_a}}{\partial U_1}\mathbf{c}_{\phi_a}\right)\right), \tag{A.126}$$

$$\boldsymbol{B_{10,2}} = \frac{1}{M+m}\left(mL\left(\frac{\partial\ddot{\phi_a}}{\partial U_2}\mathbf{c}_{\phi_a}\right)\right), \tag{A.127}$$

$$\boldsymbol{B_{10,3}} = \frac{1}{M+m}\left(mL\left(\frac{\partial\ddot{\phi_a}}{\partial U_3}\mathbf{c}_{\phi_a}\right)\right), \tag{A.128}$$

$$\boldsymbol{B_{10,4}} = \frac{1}{M+m}\left(mL\left(\frac{\partial\ddot{\phi_a}}{\partial U_4}\mathbf{c}_{\phi_a}\right)\right), \tag{A.129}$$

$$\boldsymbol{B_{10,5}} = \frac{1}{M+m}\left(mL\left(\frac{\partial\ddot{\phi_a}}{\partial \tau_x}\mathbf{c}_{\phi_a}\right)\right), \tag{A.130}$$

$$\boldsymbol{B_{10,6}} = \frac{1}{M+m}\left(mL\left(\frac{\partial\ddot{\phi_a}}{\partial \tau_y}\mathbf{c}_{\phi_a}\right)\right), \tag{A.131}$$

$$\boldsymbol{B_{11,1}} = \frac{1}{M+m}\left(-(\mathbf{c}_\phi\mathbf{c}_\theta) + mL\left(\frac{\partial\ddot{\theta_a}}{\partial U_1}\mathbf{s}_{\theta_a}\mathbf{c}_{\phi_a} + \frac{\partial\ddot{\phi_a}}{\partial U_1}\mathbf{c}_{\theta_a}\mathbf{s}_{\phi_a}\right)\right), \tag{A.132}$$

$$\boldsymbol{B_{11,2}} = \frac{1}{M+m}\left(mL\left(\frac{\partial\ddot{\theta_a}}{\partial U_2}\mathbf{s}_{\theta_a}\mathbf{c}_{\phi_a} + \frac{\partial\ddot{\phi_a}}{\partial U_2}\mathbf{c}_{\theta_a}\mathbf{s}_{\phi_a}\right)\right), \tag{A.133}$$

$$\boldsymbol{B_{11,3}} = \frac{1}{M+m}\left(mL\left(\frac{\partial\ddot{\theta_a}}{\partial U_3}\mathbf{s}_{\theta_a}\mathbf{c}_{\phi_a} + \frac{\partial\ddot{\phi_a}}{\partial U_3}\mathbf{c}_{\theta_a}\mathbf{s}_{\phi_a}\right)\right), \tag{A.134}$$

$$\boldsymbol{B_{11,4}} = \frac{1}{M+m}\left(mL\left(\frac{\partial\ddot{\theta_a}}{\partial U_4}\mathbf{s}_{\theta_a}\mathbf{c}_{\phi_a} + \frac{\partial\ddot{\phi_a}}{\partial U_4}\mathbf{c}_{\theta_a}\mathbf{s}_{\phi_a}\right)\right), \tag{A.135}$$

$$\boldsymbol{B_{11,5}} = \frac{1}{M+m}\left(mL\left(\frac{\partial\ddot{\theta_a}}{\partial \tau_x}\mathbf{s}_{\theta_a}\mathbf{c}_{\phi_a} + \frac{\partial\ddot{\phi_a}}{\partial \tau_x}\mathbf{c}_{\theta_a}\mathbf{s}_{\phi_a}\right)\right), \tag{A.136}$$

$$\boldsymbol{B_{11,6}} = \frac{1}{M+m}\left(mL\left(\frac{\partial\ddot{\theta_a}}{\partial \tau_y}\mathbf{s}_{\theta_a}\mathbf{c}_{\phi_a} + \frac{\partial\ddot{\phi_a}}{\partial \tau_y}\mathbf{c}_{\theta_a}\mathbf{s}_{\phi_a}\right)\right), \tag{A.137}$$

$$\boldsymbol{B_{12,2}} = \frac{1}{J_{xx}}, \tag{A.138}$$

$$\boldsymbol{B_{13,3}} = \frac{1}{J_{yy}}, \tag{A.139}$$

$$\boldsymbol{B_{14,4}} = \frac{1}{J_{zz}}, \tag{A.140}$$

$$\boldsymbol{B_{15,5}} = \frac{(M+m)}{MI_{px}}, \tag{A.141}$$

$$\boldsymbol{B_{16,6}} = \frac{(M+m)}{MI_{py}}. \tag{A.142}$$